FABRICATION AND CHARGE TRANSPORT MEASUREMENTS ON GRAPHENE-BASED NANOSTRUCTURES IN THE QUANTUM HALL REGIME

by

Cenk Yanık

Submitted to the Graduate School of Engineering and Natural Sciences
in partial fulfillment of
the requirements for the degree of
Doctor of Philosophy

Sabancı University
Spring 2016

FABRICATION AND CHARGE TRANSPORT MEASUREMENTS ON
GRAPHENE-BASED NANOSTRUCTURES IN THE QUANTUM HALL REGIME

APPROVED BY

Assoc. Prof. Dr. İsmet İnönü Kaya
(Thesis Supervisor) .....

Prof. Dr. Cihan Saçlıoğlu .....

Assoc. Prof. Dr. Özhan Özatay .....

Assoc. Prof. Dr. Cem Çelebi .....

Assist. Prof. Dr. Oktay Göktaş .....

DATE OF APPROVAL 10.08.2016

FABRICATION AND CHARGE TRANSPORT MEASUREMENTS ON GRAPHENE-BASED NANOSTRUCTURES IN THE QUANTUM HALL REGIME

Cenk Yanık

Physics, Doctor of Philosophy Thesis, August 2016

Thesis Supervisor: Assoc. Prof. Dr. İsmet İnönü Kaya

Keywords: Graphene, quantum Hall effect, breakdown of the quantum Hall effect, suspended graphene, minimum conductivity

ABSTRACT

Quantum Hall effect(QHE) is not only important from fundamental physics point of view but also it provides the international resistance standard. Therefore, it has a direct impact on the whole electronics industry in terms of reaching the ultimate precision in any application. Achieving QHE at higher currents near the breakdown regime is crucial for improving the resistance standard. Graphene seems to be a good candidate for the resistance metrology towards better precision and wider application under less strict conditions due to its unique electronic properties. In this thesis, we first investigated the breakdown of the QHE in mechanically exfoliated single layer graphene samples on SiO_x substrates. We found that the breakdown emerges as a gradual increase in the longitudinal resistivity rather than an abrupt jump. We have also observed that the deviation of the Hall resistance with current remains very small until an abrupt increase around $j_x = 5A/m$. The exponential dependence of the conductivity on the current is attributed to impurity mediated inter-Landau level tunnelling of carriers. As a second study, graphene samples were suspended and electrically characterized at temperatures ranging from room temperature to 20 mK at magnetic fields between 0-12 Tesla. Various techniques were developed to fabricate suspended devices and treated them to reach ultra-high cleanliness. These techniques lead us to produce devices with charge mobility values in excess of $10^6\ cm^2V^{-1}s^{-1}$. We observed that in these devices, the minimum conductivity around the Dirac point can exceed the theoretically predicted value of $4e^2/\pi h$. In such monolayer graphene devices, quantum Hall filling factors $\nu = 0, \pm 1$ can also emerge in the magneto-transport measurements in addition to the expected 2(2n+1) plateaus. The presence of these plateaus in these ultra high quality suspended samples indicate the lifting of the valley and spin degeneracy.

GRAFEN TABANLI NANO YAPILARIN ÜRETİMİ VE KUANTUM HALL REJİMİNDE YÜK TAŞINIM ÖLÇÜMLERİ

Cenk Yanık

Fizik, Doktora Tezi, Ağustos 2016

Tez Danışmanı: Doç. Dr. İsmet İnönü Kaya

Anahtar kelimeler: Grafen, kuantum Hall etkisi, kuantum Hall etkisinin kırılımı, askıda grafen, minimum iletkenlik

ÖZET

Kuantum Hall etkisi uluslararası direnç standartını oluşturması nedeniyle temel fizik açısından olduğu kadar uygulama açısından da çok önemlidir. Elektronik endüstrisine en yüksek hassasiyete erişimi belirlemek gibi doğrudan önemli bir etkisi vardır. Kırılma rejimine yakın akımlarda kuantum Hall etkisine ulaşılması direnç standartının geliştirilmesi açısından büyük önem taşımaktadır. Grafen kendine has elektronik özelliklerinden dolayı daha esnek koşullar altında direnç metrolojisindeki yüksek hassasiyet ve geniş uygulama alanı açısından iyi bir aday olarak görülmektedir. Bu tezde ilk olarak, SiO_x attaşlar üzerinde mekanik ayrıştırma yöntemi ile elde edilmiş tek katman grafen örnekler üzerinde kuantum Hall etkisinin kırılması incelenmiştir. Boyuna direncin ani olarak artışından ziyade kademeli olarak arttığı gözlenmiştir. Ayrıca akım yoğunluğunun 5A/m değerine kadar Hall direncindeki sapmanın çok az olduğu bu değerden sonra ani bir artma olduğu gözlenmiştir. İletkenliğin akım üzerindeki üstel bağlılığı taşıyıcıların kirlilik aracılıklı Landau seviyeleri arası bir tünellemeye atfedilmiştir. Bu tezde ikinci çalışma olarak, grafen örnekler askıda bırakılarak oda sıcaklığı ve 20 mK sıcaklıkları arasında, 0-12 Tesla manyetik alan aralığında elektriksel karakterizasyonları yapılmıştır. Asılı grafen aygıtların üretimi ve ultra saflık düzeyinde temizleme süreçleri geliştirilmiştir. Geliştirilen tekniklerle yük hareketlilikleri $10^6\ cm^2V^{-1}s^{-1}$ nin üzerinde değerlere ulaşan aygıtların üretilmesi başarılmıştır. Bu aygıtlarda grafenin Dirac noktası civarındaki en düşük iletkenliğinin kuramsal olarak öngörülen $4e^2/\pi h$ değerinin altına inebildiği gözlenmiştir. Ayrıca gerçeklestirilen manyeto-taşınım ölçümlerinde tek katman grafende beklenen 2(2n+1) kuantum Hall dolum faktörlerinin yanı sıra vadi ve spin yozlaşmasının ortadan kalkması sonucunda $\nu = 0, \pm 1$ dolum faktörlerinin belirginleştiği saptanmıştır.

aileme

(to my family)

ACKNOWLEDGEMENTS

First of all, I would like to express my sincere gratitude to my advisor Assoc. Prof. Dr. İsmet İnönü Kaya. I am grateful for all of the opportunities that he has provided me. He was always more than just an advisor for all the years. It has been a privilege for me to study under his guidance.

I would like to thank to Prof. Dr. Cihan Saçlıoğlu, Assoc. Prof. Dr. Özhan Özatay, Assoc. Prof. Dr. Cem Çelebi and Assist. Prof. Dr. Oktay Göktaş for being on my thesis committee.

I would like to express my special thanks to the members of Faculty Engineering and Natural Sciences of Sabanci University who kindly shared the knowledge and experience with me. The staff of Sabanci University Nanotechnology Research and Application Center (SUNUM) also deserves to be acknowledged for their contributions. I wish to express my appreciation to Volkan Özgüz, the director of SUNUM, who believed in me and gave an opportunity to work as an ebeam specialist at SUNUM while I have been a Phd Student.

I owe special thanks both the present and past laboratory group members in our quantum transport & Nano-electronics laboratory who have kindly helped me with my research & study and made the journey pleasurable and rewarding. I would like to thank all my friends, who support and encourage me. I would like to thank Özge Çavuşlar for her endless support to write this thesis.

I would like to especially thank my parents for their endless love and selfless support over the years. I am grateful for everything they have done for me. Rest in peace my dear father!, missing you..

Lastly, we appreciate the financial support received from the Scientific and Technological Research council of Turkey (TUBITAK) under grants 107T855 and 112T990.

Contents

List of Figures

Chapter 1

INTRODUCTION

1.1 Motivation

While graphene as a single sheet of carbon atoms arranged in a honeycomb structure has been studied theoretically since 1947 [8], it was long thought to be unstable at any finite temperature due to the thermodynamic instability of two-dimensional crystals [9]. Since its first experimental realisation[10], surprisingly isolated on SiO_x surface by scotch tape method, graphene has attracted tremendous interest as a truly 2D system that allows the study of effectively massless Dirac Fermions arising from its unique electronic band structure. Before investigation of graphene, the experimental study of the two dimensional electron system (2DEG) system has been realized by confining carriers in semiconductor structures, such as GaAs-AlGaAs High electron mobility transistor (HEMT), silicon metal oxide semiconductor field effect transistors (Si-MOSFETs), or quantum wells. The studies on these low dimensional electron systems have produced remarkable discoveries in quantum physics. One of the most prominent phenomena is the integer quantum Hall effect (IQHE) discovered by von Klitzing, Dorda, and Pepper in 1980[2]. The basic observation of this effect is that the Hall resistance of a 2DEG is quantized in units of h/e^2, with h the Planck's constant and e the elementary charge at low enough temperatures in the presence of high enouugh magnetic fields. Striking feature underlying this effect is an universal macroscopic quantum effect, which is independent of the material system in which the 2DEG system is realised. Therefore, the quantized Hall resistance of the QHE has been used as an international resistance standard with very high precision (relative error better than one part in billion) [11]. The resistance quantum $R_K = h/e^2 = 25812.807... \ \Omega$ was named as the von Klitzing constant and he was awarded the 1985 Nobel prize in physics for this discovery. In the quantum Hall regime, the longitudinal resistivity ρ_{xx} approaches zero (no dissipation in the bulk of the system) near the filling factors $\nu = n_s h/eB$, with n_s being the areal electron density of the 2DEG system and B the magnetic field. The quantum Hall states can persist until the Hall cur-

rent I reaches a critical value of I_c. Above these values, ρ_{xx} increases suddenly from zero and Hall resistivity starts deviating from it quantized value, system becomes dissipative and this phenomenon is called the electrical breakdown of the QHE[12, 13]. Transport near the breakdown regime is generally referred as non-equilibrium transport. The breakdown of the QHE has attracted great interest within the scientific community from both a fundamental science and a metrology point of view. In order to perform high precision measurements, the sample current should be as high as possible due to the high signal to noise ratio but below the critical limit where the QH conditions survive. Graphene is considered to be a good candidate for the quantum hall resistance metrology towards better precision and wider application under less strict conditions such as high temperatures, low magnetic fields[14] due to its unique electronic properties. Experimental results on the precision measurements so far indicate that the precision in R_K can be improved[15–24]. Therefore, the breakdown of the quantum Hall effect in graphene needs to be better understood. First motivation of this thesis is to investigate non-equilibrium transport properties of graphene in narrow graphene hall devices in which the microscopic inhomogeneities can play a critical role on the QHE breakdown.

The second motivation of this thesis is dedicated to fabrication and experimental study of high quality suspended devices[25–29]. In order to probe the interesting quantum transport properties close to the charge neutrality point where the interactions are not screened out due to the substrate, samples need to be current annealed[30] which eventually provides very low inhomogeneity fluctuations in the carrier density ($\delta n \lesssim 10^9\ cm^{-2}$) leading observation of interesting phenomena that might occur at the Dirac point.

1.2 Structure of the Thesis

In this thesis, we present the charge transport measurements on successfully characterized graphene based nanostructures in particular on the graphene Hall-bars & free standing graphene sheets in the quantum Hall regime.

A brief summary for each of the following chapters can be given as;

Chapter 2 introduces the basic concepts of 2DEG systems and Graphene in terms of electronic properties and follows with examining classical and quantum Hall effects in generic two-dimensional electron gases. We present unique electronic properties of graphene as a consequence of its extraordinary band structure. Finally, we introduce the edge transport picture of a confined quantum Hall system in the Landau-Büttiker formalism which provides an alternative explanation for the quantum Hall effect.

In ***chapter 3*** we give a summary of the earlier works on the breakdown of the quantum Hall effect for 2DEG systems and subsequently in graphene. Then, phenomenological description and some of the physical models proposed for the breakdown of the quantum Hall effect in two dimensional electron systems are included at the end of the chapter.

In ***Chapter 4*** fabrication of the graphene based devices (Hall-bars, suspended sheets) before the measurements are described. The recipes and process parameters of each fabrication step are provided in detail. Finally, we present the experimental measurement techniques and set-ups that have been utilized to characterize the charge transport properties of graphene.

Chapter 5 focuses on the nonequilibrium transport results of graphene Hall devices on SiO_x substrates in the quantum Hall regime. The results are interpreted as the strong variation of the breakdown behaviour throughout the sample due to the randomly distributed scattering centers that mediates the breakdown of the quantum Hall effect.

Chapter 6 is dedicated to the characterization and quantum transport measurements of high quality suspended graphene samples with introducing an effective annealing technique we developed.

Chapter 7, experimental results on the thermo-pressured-cycled ultra clean high quality suspended graphene are presented. The observation of an insulating behaviour near the charge neutrality point after the thermo-pressure cycle, is discussed through the conductance fluctuations of a weakly disordered ultra clean graphene sheet with strong short-range potentials which results in localization via inter-valley backscattering.

Chapter 8 summarizes the presented work.

Chapter 2

BASIC CONCEPTS

In this chapter, we first investigate the importance of two dimensional electron gases (2DEG) in terms of their electronic transport properties. We first extract the significant quantities such as density of states, Fermi energy and Fermi momentum, and review classical and quantum Hall effects in these electron systems.

Later, we focus on graphene lattice structure and electronic properties, and investigate its transport behaviour under a perpendicular magnetic field. We discuss the differences between the quantum Hall effects in usual 2DEGs and graphene and try to understand its significance through examples.

2.1 Two Dimensional Electron Gases (2DEG)

In order to study the electrons confined in two dimensions, we first start with Schrödinger equation for a free particle. In this section, we mostly follow Michael Marder's Condensed Matter Physics book [31]. Assuming the periodic boundary conditions in x and y directions which have the lengths L_x and L_y respectively, we obtain:

$$\begin{aligned} & -\frac{\hbar^2}{2m}\nabla^2\Psi(x,y,z) = E\Psi(x,y,z) \\ & \Psi(x,y,z) = \Psi(x+L_x,y,z) = \Psi(x,y+L_y,z) \\ \Rightarrow \quad & \Psi(x,y,z) = \frac{1}{\sqrt{L_xL_y}}e^{ik_xx+ik_yy} = \frac{1}{\sqrt{A}}e^{i\vec{k}.\vec{r}} \end{aligned} \tag{2.1}$$

, where $A = L_xL_y$ is the total area of the region which confines the two dimensional electron gas and constitutes the boundary for single electron wavefunctions. According to our chosen periodic boundary condition, we have a restriction on our $\vec{k}$ vector, and therefore the electron energy:

$$
\begin{aligned}
k_x = \frac{2\pi}{L_x} n_x \quad \& \quad k_y = \frac{2\pi}{L_y} n_y, \quad n_x, n_y = 0, \pm 1, \pm 2, ... \\
E_{\vec{k}} = \frac{\hbar^2 \vec{k}^2}{2m} = \frac{h^2}{2m} \left(\frac{{n_x}^2}{L_x^2} + \frac{{n_y}^2}{L_y^2} \right)
\end{aligned}
\tag{2.2}
$$

Since the indices n_x and n_y quantize the energy, according to the Pauli Exclusion Principle, only two electrons with up and down spins can occupy the same energy state. Now, if we consider N non-interacting electrons in this model at zero temperature, we must fill the energy states $E_{\vec{k}}$ starting from the lowest energy state and successively putting the others in the higher energy levels up to a certain cut-off wave vector k_F which is called Fermi wave vector. In the k-space, therefore, we have points in 2-dimension which are separated by $2\pi/L_x$ in the x-direction and $2\pi/L_y$ in the y-direction. Since we have only one point in the area $\frac{2\pi}{L_x}\frac{2\pi}{L_y} = \frac{(2\pi)^2}{A}$, we have $\frac{A}{(2\pi)^2}$ states per area. Dividing this expression by the area and multiplying it by 2 to include spin degeneracy, we obtain the density of states (DOS), which is independent of area and the wave vector, and only depends on the dimension of the theory. Density of states basically tells us how many states are available in a given small area/volume/hypervolume (depending on the dimension) $d^d k$ which eventually help us to evaluate many useful quantities related to the free electron system. For instance, we can evaluate the sum of an arbitrary function $F(\vec{k})$ which depends on the wave vector:

$$
\begin{aligned}
\sum_{\vec{k}} F(\vec{k}) = A \int d^d k D(\vec{k}) F(\vec{k}) \\
D^{2D}(\vec{k}) = \frac{1}{2\pi^2}
\end{aligned}
\tag{2.3}
$$

, where A can be a length, area, volume or hypervolume, depending on the dimension d in which we are working in.

Now, we want to calculate energy density of states which tells us how much the density of available states changes with energy. Since any arbitrary function $F(\vec{k})$ is also a function of energy $F(E_{\vec{k}})$, we can evaluate the same summation as:

$$
\sum_{\vec{k}} F(E_{\vec{k}}) = A \int dE D(E) F(E) \tag{2.4}
$$

However, using the equation in (2.3), we obtain:

$$\begin{aligned}\sum_{\vec{k}} F(E_{\vec{k}}) &= A \int d^2k D(\vec{k}) F(E_{\vec{k}}) \\ &= A \int dE \int d^2k D(\vec{k}) \delta(E - E_{\vec{k}}) F(E)\end{aligned} \tag{2.5}$$

Comparing (2.4) and (2.5), we arrive at:

$$D(E) = \int d^2k D(\vec{k}) \delta(E - E_{\vec{k}}) \tag{2.6}$$

Now, we can calculate the energy density of states from the above equation using the polar coordinates where the differential area is $d^2k = 2\pi k dk$:

$$\begin{aligned}D(E) &= \int 2\pi k dk \frac{1}{2\pi^2} \delta(E - E_{\vec{k}}) \\ &= \frac{1}{\pi} \int_0^\infty k dE \frac{dk}{dE} \delta(E - E_{\vec{k}})\end{aligned} \tag{2.7}$$

, where $k = \frac{\sqrt{2mE}}{\hbar}$ and $\frac{dk}{dE} = \frac{m}{\hbar^2 k} = \frac{\sqrt{m}}{\hbar\sqrt{2E}}$. Therefore, we have:

$$D(E) = \frac{1}{\pi} \int_0^\infty dE \frac{m}{\hbar^2} \delta(E - E_{\vec{k}}) = \frac{m}{\pi\hbar^2} \tag{2.8}$$

This result shows us that in two-dimension, density of states does not vary with energy and always stays constant unless another subband energy state is occupied. Each energy level contributes to the density of states with equal amount, and at sufficiently low temperatures and in the ground state, density of electron states can be reduced in the material to very low values. [32].

2.2 Classical and Quantum Hall Effects in 2DEG

This section serves to give a summary of electronic transport in two dimensional electron gases under perpendicular magnetic field. First, we treat electrons as classical point particles and solve for the equations of motion for a single electron. Then, we treat electrons as quantum particles which obey Schrödinger equation, and obtain the energy eigenvalues for a single electron.

2.2.1 Classical Hall Effect

In this subsection, we write an Hamiltonian for an electron under a perpendicular magnetic and parallel electric field, and solve it first classically, and subsequently quantum mechanically.

Under a magnetic field, canonical momentum $\vec{p}$ transforms into $\vec{p} - \frac{q}{c}\vec{A}$, where $\vec{A}$ is a vector potential and q is the charge of the particle which is $-e$ in our case [33]. We also add a parallel electric field in order to study the electrical transport of a single electron, as well.

$$\begin{aligned} \mathcal{H} &= \frac{1}{2m}\big(\vec{p} + \frac{e}{c}\vec{A}\big)^2 - e\Phi \\ \mathcal{L} &= \frac{1}{2}m\dot{\vec{r}}^2 + e\Phi - \frac{e}{c}\dot{\vec{r}}.\vec{A} \end{aligned} \tag{2.9}$$

In equation 2.9, both Hamiltonian and Lagrangian of the model is given [34]. Using Euler-Lagrange equation, we can obtain the equation of motion for this system. First of all, we define our coordinate system. Magnetic field is perpendicular to the xy-plane, along the z axis, and electric field is in the x axis. Therefore, $\vec{A} = Bx\hat{j}$ and $\Phi = -\int_c \vec{E}.d\vec{r} = -\vec{E}.\vec{r}$ where $\vec{E} = E_x\hat{i} + E_y\hat{j}$. Replacing these into the Lagrangian in 2.9, we obtain:

$$\mathcal{L} = \frac{m}{2}(\dot{x}^2 + \dot{y}^2 + \dot{z}^2) - eE_x x - eE_y y - \frac{e}{c}B\dot{y}x \tag{2.10}$$

Now, using the Euler-Lagrange equation stated as $\frac{d}{dt}(\frac{\partial \mathcal{L}}{\partial \dot{x}_i}) - \frac{\partial \mathcal{L}}{\partial x_i} = 0$, where $i = 1, 2, 3$ indexes the three Cartesian coordinates, we obtain the equations of motion as follows:

$$\begin{aligned} \frac{d}{dt}(\frac{\partial \mathcal{L}}{\partial \dot{x}}) = m\ddot{x} \quad \& \quad \frac{\partial \mathcal{L}}{\partial x} = -eE_x - \frac{e}{c}B\dot{y} \\ \frac{d}{dt}(\frac{\partial \mathcal{L}}{\partial \dot{y}}) = m\ddot{y} - \frac{e}{c}B\dot{x} \quad \& \quad \frac{\partial \mathcal{L}}{\partial y} = -eE_y \\ \frac{d}{dt}(\frac{\partial \mathcal{L}}{\partial \dot{z}}) = m\ddot{z} \quad \& \quad \frac{\partial \mathcal{L}}{\partial z} = 0 \end{aligned} \tag{2.11}$$

Equating left and right hand sides in each line, and setting the electric field to 0 for simplicity, we obtain three equations regarding the motion of a single electron, two of which are coupled to each other. Furthermore, we do not need to worry about the last equation since we have no motion in the $\hat{z}$ direction. Therefore, the equations of motion and their solutions are as follows [35]:

$$
\begin{aligned}
m\ddot{x} = -\frac{e}{c}B\dot{y} \quad \& \quad m\ddot{y} = \frac{e}{c}B\dot{x} \\
\Rightarrow x(t) = x_0 - Rsin(\omega_0 t + \phi) \\
y(t) = y_0 - Rcos(\omega_0 t + \phi)
\end{aligned}
\tag{2.12}
$$

, where $\omega_0 = \frac{eB}{mc}$ is the cyclotron frequency of the electrons in the circular orbit, x_0 and y_0 are the center of the motion and ϕ is just a phase depending on the initial conditions. This effect is called Hall effect and a result of the Lorentz force in classical electrodynamics. In Figure 2.1, a schematics of classical Hall effect is shown.

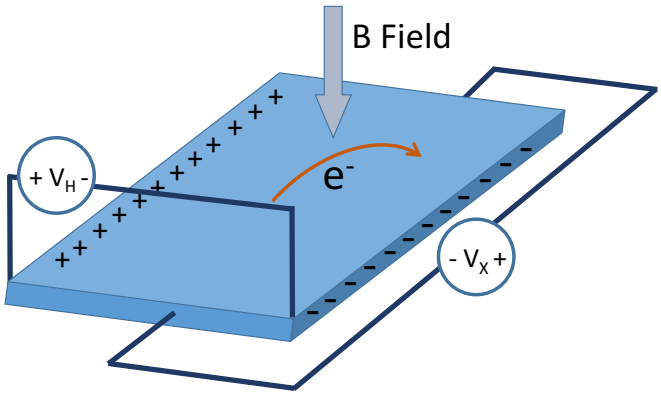

Figure 2.1: A charged particle orbiting in a circle due to the Lorentz force and a typical experimental setup for the measurement of classical Hall effect[1].

Then, we study the electrons under both a perpendicular magnetic field and a parallel electric field which drifts the particles throughout the two dimensional electron sheet. We start by writing the equations of motion introduced in Equation 2.11 in matrix notation with the electric field components included. Also, we introduce a dissipative force $-\frac{m}{\tau}(\dot{x}\hat{i}+\dot{y}\hat{j})$ which accounts for the electrons random scatterings throughout the conductor, and acts like a frictional force since it depends on the velocity [35]. Here τ stands for the average time between the two successive scatterings of the electrons.

$$
m\begin{pmatrix}\ddot{x}\\ \ddot{y}\end{pmatrix} = \begin{pmatrix}-eE_x - \frac{e}{c}\dot{y}B - \frac{m\dot{x}}{\tau}\\ -eE_y + \frac{e}{c}\dot{x}B - \frac{m\dot{y}}{\tau}\end{pmatrix}
\tag{2.13}
$$

In steady state, however, $\ddot{x}$ and $\ddot{y}$ are going to be zero, and we assume so in order to study the equilibrium case in the conductor. Dividing the both sides by $\frac{m}{\tau}$, we obtain:

$$\begin{pmatrix} \dot{x} + \frac{eB}{mc}\tau\dot{y} \\ \dot{y} - \frac{eB}{mc}\tau\dot{x} \end{pmatrix} = -\frac{e\tau}{m}\begin{pmatrix} E_x \\ E_y \end{pmatrix} \tag{2.14}$$

Recognizing $\vec{J} = nq\dot{\vec{r}}$ and multiplying both sides with qn where $q = -e$ and n is the electron density inside the conductor, and replacing $\frac{eB}{mc}$ with ω_0 we get:

$$\begin{pmatrix} J_x + \omega_0\tau J_y \\ J_y - \omega_0\tau J_x \end{pmatrix} = \frac{e^2 n\tau}{m}\begin{pmatrix} E_x \\ E_y \end{pmatrix} \tag{2.15}$$

Now, if we define $\sigma_0 = \frac{e^2 n\tau}{m}$ and write this expression like a matrix equation, we obtain:

$$\frac{1}{\sigma_0}\begin{pmatrix} 1 & \omega_0\tau \\ -\omega_0\tau & 1 \end{pmatrix}\begin{pmatrix} J_x \\ J_y \end{pmatrix} = \begin{pmatrix} E_x \\ E_y \end{pmatrix} \tag{2.16}$$

Here, we obtain an equation in the form of $\vec{E} = \rho\vec{J}$, where ρ is the resistivity tensor and the whole equation resembles the Ohm's law. Indeed, it reduces to the Ohm's law $V = IR$ if $B = \omega_0 = 0$. However, due to the magnetic field, there is a Hall component in the perpendicular direction. Now, if we invert the resistivity tensor, we obtain the conductivity tensor $\sigma = \rho^{-1}$:

$$\begin{aligned} \rho &= \begin{pmatrix} \rho_{xx} & \rho_{xy} \\ \rho_{yx} & \rho_{yy} \end{pmatrix} = \frac{1}{\sigma_0}\begin{pmatrix} 1 & \omega_0\tau \\ \omega_0 & 1 \end{pmatrix} \\ \sigma &= \begin{pmatrix} \sigma_{xx} & \sigma_{xy} \\ \sigma_{yx} & \sigma_{yy} \end{pmatrix} = \frac{\sigma_0}{1+\omega_0^2\tau}\begin{pmatrix} 1 & -\omega_0\tau \\ \omega_0\tau & 1 \end{pmatrix} \end{aligned} \tag{2.17}$$

It is worth to place some remarks here about the resistivity tensor. First of all, if we look at the off-diagonal Hall components of this tensor, we realize that they are independent of the average time between the scatterings of the charge carriers, which means the resistivity that the electrons are subject to are immune to the dirt and sample specific properties which are projected on τ. Whatever the properties of the material, one always measures the same resistivity for the samples which have the same electron density and are subject to the same magnetic field, since $\rho_{xy} = -\rho_{yx} = \frac{\omega_0\tau}{\sigma_0} = \frac{B}{en}$.

One other remark about the two dimensional classical Hall effect is the fact that the

Hall resistivity and the Hall resistance are indeed the same quantities, although resistance generally depends on the geometry of the sample. Hall resistivity is defined as the division of the voltage drop between the Hall contacts and the current passing through the sample, $R_H = \frac{V_\perp}{I_\parallel}$. Since $V_\perp$ equals to LE_y and $I_\parallel = LJ_x$, we obtain $R_H = \frac{E_y}{J_x} = \rho_{xy}$. Therefore, the resistance which we usually measure in the laboratory is the same as the resistivity which is independent of the dimensions of the sample.

Finally, Hall measurements are essential in the semiconductor industry since one can extract the type of the dominant charge carrier in a material and also measure the mobility of the sample.

2.2.2 Quantum Hall Effect

Quantum Hall effect was discovered in 1980 by Klaus von Klitzing and his co-workers [2] by observing constant plateaus rather than a monotonic increase in the Hall resistance with increasing magnetic field, as we discussed in the previous section. The special thing about his sample was that the electrons were confined in a very narrow region in a high quality Si-MOSFET transistor. Therefore, the sample was closer to a "2D" electron gas approximation and it was possible to observe this interesting effect in very low temperatures (4 K) and high magnetic fields.

Quantum Hall effect is a result of the formation of discrete Landau energy levels in the 2DEG. It is easy to show that the electron energy levels are discretized by replacing the momentum and position variables in the Hamiltonian given in Equation 2.9 with their operator counterparts:

$$\mathcal{H} = \frac{1}{2m}\left(\hat{\vec{p}} + \frac{e}{c}\vec{A}\right)^2 \tag{2.18}$$

, where $\hat{\vec{p}} \rightarrow \frac{-\hbar^2}{2m}\vec{\nabla}$ and $\vec{A} = B\hat{x}\hat{j}$ where $\hat{x}$ is the position operator. Now, we just solve the Schrödinger equation:

$$\begin{aligned}
\left(\frac{1}{2m}\left(\hat{\vec{p}} + \frac{eB}{c}\hat{x}\hat{j}\right)^2\right)\psi &= E\psi \\
\left[\frac{1}{2m}\left(\hat{p_x}\hat{i} + \hat{p_y}\hat{j} + \frac{eB}{c}\hat{x}\hat{j}\right)^2\right]\psi &= E\psi \\
\left[\frac{\hat{p_x}^2}{2m} + \frac{1}{2m}\left(\hat{p_y} + \frac{eB}{c}\hat{x}\right)^2\right]\psi &= E\psi
\end{aligned} \tag{2.19}$$

In the last line in Equation 2.19, since the operator $\hat{p_y}$ commutes with the whole Hamilto-

nian, we can replace it by its eigenvalue which is $\hbar k_y$. By leaving the $\hat{x}$ operator alone in that expression and using $\omega_0 = \frac{eB}{mc}$, we obtain:

$$\begin{aligned} \left[\frac{\hat{p_x}^2}{2m} + \frac{e^2B^2}{2mc^2}\left(\hat{x} + \frac{c\hbar k_y}{eB}\right)^2\right]\psi = E\psi \\ \Rightarrow \left[\frac{\hat{p_x}^2}{2m} + \frac{1}{2}m\omega_0^2\left(\hat{x} + \frac{\hbar k_y}{m\omega_0}\right)^2\right]\psi = E\psi \end{aligned} \tag{2.20}$$

This is just usual harmonic oscillator Hamiltonian whose potential energy is shifted by $-\frac{\hbar k_y}{m\omega_0}$ [33]. Its energy eigenvalues, therefore, are given by:

$$E_n = \hbar\omega_0(n + \frac{1}{2}) \tag{2.21}$$

Until now, we proved that energy levels for electrons under a magnetic field is quantized in the half-integers of $\hbar\omega_0$. A remark about this calculation is that energy is only dependent on the integer index n, but the wavefunction of the electrons depends on both n and wave vector k. Therefore, we expect a degeneracy for each Landau level. In order to calculate this degeneracy, we assume that the shift in position x $-\frac{\hbar k_y}{m\omega_0}$ stays in the sample size where the sample size is $L \times L$:

$$0 < -\frac{\hbar k_y}{m\omega_0} < L \tag{2.22}$$

However, we know that k_y can only take the values $\frac{2\pi}{L}l_y$, where l_y is an integer, due to the quantization. By explicitly writing the value of ω_0:

$$0 < -\frac{2\pi\hbar l_y}{mL}\frac{mc}{eB} < L \quad \Rightarrow \quad -\frac{eBL^2}{hc} < l_y < 0 \tag{2.23}$$

Here, $L^2 = A$ is the sample area and therefore $\Phi = BA$ is the total magnetic flux through the sample. Since, l_y indexes the number of available states, and it can be at most $N = \frac{e\Phi}{hc}$, we have:

$$N = \frac{\Phi}{(hc/e)} = \frac{\Phi}{\Phi_0}, \quad \Phi_0 = \frac{hc}{e} \tag{2.24}$$

As a good approximation, number of the states available is the ratio of the total magnetic flux passing through the sample to the flux quantum Φ_0.

Now, we can calculate the conductivity of the sample in quantum Hall regime. When

n-Landau levels are filled, and there are $n\frac{\Phi}{\Phi_0}$ number of states available since each Landau level contributes to the number of states by $\frac{\Phi}{\Phi_0}$, total charge in the sample is going to be $Q = -en\frac{\Phi}{\Phi_0}$. From the Lenz' law, we know that $\oint_C d\vec{l}.\vec{E} = -\frac{1}{c}\frac{\partial\Phi}{\partial t}$ where $\vec{E}$ is the electric field parallel to the contour and Φ is the total magnetic flux. Using $\vec{j_\perp} = \sigma_{xy}\vec{E_\parallel}$, we obtain:

$$\begin{aligned} \frac{1}{\sigma_{xy}}\oint_C d\vec{l}.\vec{j_\perp} &= \frac{-1}{c}\frac{\partial\Phi}{\partial t} \\ \Rightarrow \frac{\partial Q}{\partial t} = -\frac{\sigma_{xy}}{c}\frac{\partial\Phi}{\partial t} \quad &\Rightarrow \quad \sigma_{xy} = -c\frac{\partial Q}{\partial\Phi} \\ Q = -en\frac{\Phi}{\Phi_0} \quad &\Rightarrow \quad \sigma_{xy} = \frac{nec}{\Phi_0}\frac{\partial\Phi}{\partial\Phi} \\ \sigma_{xy} &= n\frac{e^2}{h} \end{aligned} \tag{2.25}$$

Since the integral on the left hand side in the first line equals to the rate of change of the charge encapsulated by the contour C, we obtain $\sigma_{xy} = -c\frac{\partial Q}{\partial\Phi}$ in the second line. Then using the charge expression $Q = -en\frac{\Phi}{\Phi_0}$, we were able to derive the quantization of the Hall conductance. Figure 2.2 shows the quantization of the Hall resistance.

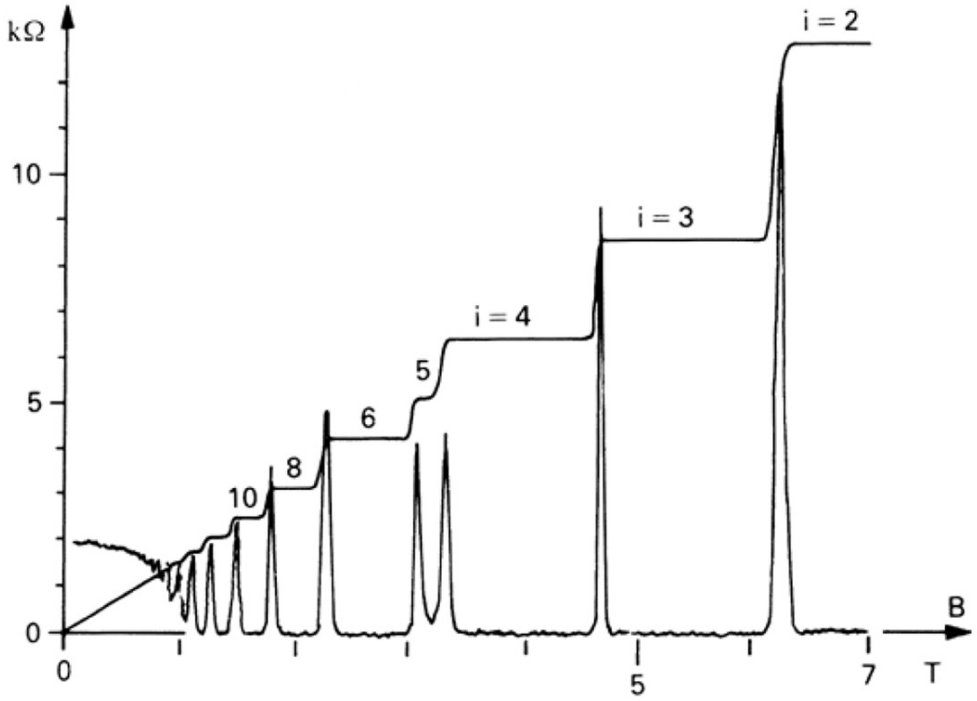

Figure 2.2: Integer quantum Hall effect: The quantized Hall plateaus assosiated with vanishing longitudional resistance as a function of magnetic field[2].

2.3 Graphene

Graphene has attracted an enormous attention due to its physically rich and interesting nature. First of all, before graphene, all the two dimensional electron gases were formed by confining the conduction carriers through band-gap engineering. These were enough to neglect the electron motion in the third dimension, however, no one was ever able to realize a truly two dimensional electron gas in the literature. First, Andre Geim and Katya Novoselov isolated a long-thought [8] two dimensional graphite sheet in 2004, which then let them won a Nobel prize in physics in 2010 [10].

In this section, we start to study graphene by introducing its lattice structure and deriving the energy dispersion relation of the charge carriers with respect to momentum. Then, we show that, at low energies, its charge carriers obey the massless Dirac equation, which in fact makes the graphene special. Finally, we discuss the quantum Hall effect in graphene and its anomalous sequence in comparison to usual the quantum Hall effect.

2.3.1 Energy Dispersion Relation in Graphene

Graphene lattice consists of carbon atoms arranged in a honeycomb lattice which is basically a hexagonal lattice with a basis. Since the honeycomb lattice is not a simple one, two carbon atoms in the basis are inequivalent to each other. Therefore, we conventionally label the sublattice atoms as A and B which have their own lattice translation vectors. This difference between two sublattice atoms lead two different reciprocal lattice points as well, namely K and K' points [3]. In Figure 2.3, graphene lattice in real space and reciprocal space are shown.

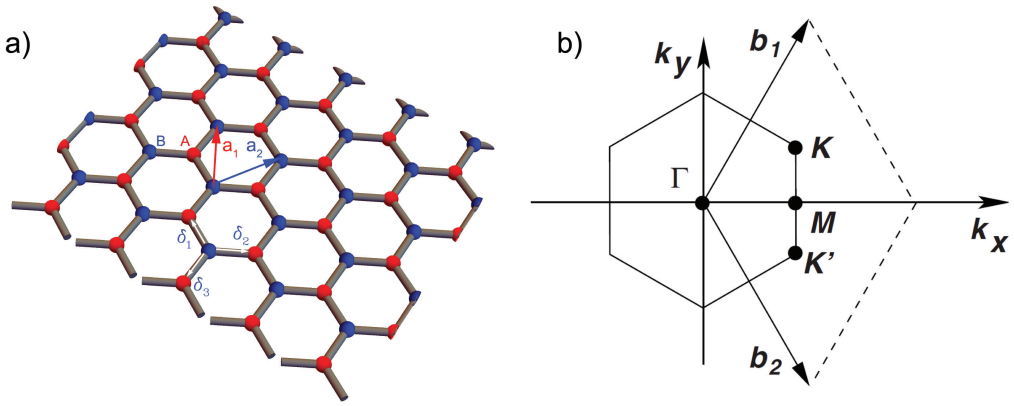

Figure 2.3: a) Honeycomb lattice of graphene with sublattices A and B. b) Reciprocal lattice of graphene with K and K' points.[3].

In order to obtain the energy dispersion relation of graphene, we use tight-binding

model approach. Only considering the nearest-neighbour hopping, Hamiltonian for the graphene electrons is given as follows:

$$\mathcal{H} = -t \sum_{<i,j>} \hat{a}_i^\dagger \hat{b}_j - t \sum_{<i,j>} \hat{b}_i^\dagger \hat{a}_j \tag{2.26}$$

, where the operators $\hat{a}$ and $\hat{b}$ annihilate, and $\hat{a}^\dagger$ and $\hat{b}^\dagger$ create electrons at the sites A and B, respectively. Since there are three different ways to go from i to j, rather than carrying the sum over all sites i and j, we carry the sum over each lattice site and the three different configurations.

$$\mathcal{H} = -t \sum_{j=1}^{3} \sum_{i} \hat{a}_i^\dagger \hat{b}_{i+j} + \hat{b}_i^\dagger \hat{a}_{i+j} \tag{2.27}$$

Now, we take the Fourier transform of each operator and replace each operator in Equation 2.27 with their Fourier expansions. Our Fourier transform convention is as follows:

$$\hat{a}_i = \frac{1}{\sqrt{N}} \sum_k \hat{a}_k e^{-i\vec{k}.\vec{r}_i} \quad \& \quad \hat{a}_k = \frac{1}{\sqrt{N}} \sum_i \hat{a}_i e^{i\vec{k}.\vec{r}_i} \tag{2.28}$$

Replacing the Fourier expansion in Equation 2.27 and defining the difference $\vec{r}_i - \vec{r}_{i+j}$ as Δ_j we obtain:

$$\begin{aligned} \mathcal{H} &= -t \sum_{j=1}^{3} \sum_{k} \hat{a}_k^\dagger \hat{b}_k e^{-i\vec{k}.\vec{\Delta}_j} + \hat{b}_k^\dagger \hat{a}_k e^{i\vec{k}.\vec{\Delta}_j} \\ &= -t \sum_k \hat{a}_k^\dagger \hat{b}_k \left(\sum_{j=1}^{3} e^{-i\vec{k}.\vec{\Delta}_j} \right) + \hat{b}_k^\dagger \hat{a}_k \left(\sum_{j=1}^{3} e^{i\vec{k}.\vec{\Delta}_j} \right) \end{aligned} \tag{2.29}$$

If we call the summation $\mathcal{H}_{ba} = -t \sum_{j=1}^{3} e^{i\vec{k}.\vec{\Delta}_j}$, we obtain:

$$\begin{aligned} &\sum_k H_{ba} \hat{a}_k{}^\dagger \hat{b}_k + H_{ba}^* \hat{b}_k^\dagger \hat{a}_k = \sum_k \mathcal{H}_{ba} \hat{a}_k{}^\dagger \hat{b}_k + h.c. \\ &\mathcal{H} = \sum_k \begin{pmatrix} a_k{}^\dagger & b_k{}^\dagger \end{pmatrix} \begin{pmatrix} 0 & \mathcal{H}_{ba} \\ \mathcal{H}_{ba}^* & 0 \end{pmatrix} \begin{pmatrix} a_k \\ b_k \end{pmatrix} \end{aligned} \tag{2.30}$$

As a result, the off-diagonal elements of the Hamiltonian are given by $\mathcal{H}_{ba}$ and its complex conjugate, while diagonal elements which only shift the energy levels set to zero

for convenience. Therefore, the energy dispersion of the graphene can be calculated by solving the eigenvalue equation:

$$E = \pm \left| \mathcal{H}_{ba} \right| \quad \& \quad \mathcal{H}_{ba} = -t\left(e^{-i\vec{k}.\vec{\Delta}_1} + e^{-i\vec{k}.\vec{\Delta}_2} + e^{-i\vec{k}.\vec{\Delta}_3}\right) \tag{2.31}$$

From the honeycomb lattice geometry, we recognize the vectors $\vec{\Delta}_1$, $\vec{\Delta}_2$ and $\vec{\Delta}_3$ as $-\frac{a}{2}\hat{i}$, $\frac{a}{2}(\hat{i} + \sqrt{3}\hat{j})$ and $\frac{a}{2}(\hat{i} - \sqrt{3}\hat{j})$, respectively. After taking the absolute value of $\mathcal{H}_{ba}$, we obtain the energy dispersion relation as:

$$E(k) = \pm t\sqrt{3 + 2\cos(\sqrt{3}k_x a) + 4\cos(\frac{\sqrt{3}}{2}k_x a)\cos(\frac{3}{2}k_y a)} \tag{2.32}$$

A sketch of energy dispersion relation is shown in Figure 2.4.

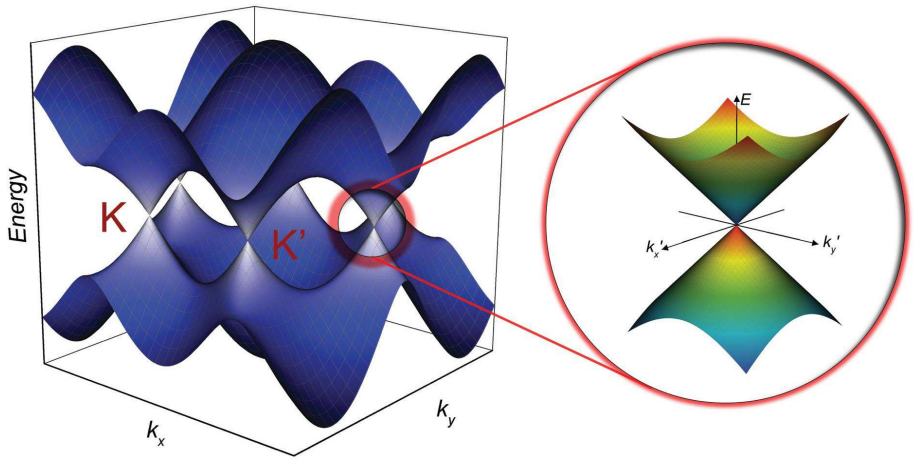

Figure 2.4: Dispersion relation of graphene with the low-energy, gapless Dirac cones.

In this figure, we realize that the energy vanishes at two points, $\vec{K} = (k_x, k_y) = (\frac{4\pi}{3\sqrt{3}a}, 0)$ and $\vec{K'} = (k'_x, k'_y) = (-\frac{4\pi}{3\sqrt{3}a}, 0)$. If we expand the dispersion relation around these points, we arrive at the Hamiltonian:

$$\mathcal{H} = v_F \vec{p}.\vec{\sigma} \tag{2.33}$$

This Hamiltonian shows at low energies and charge carriers in graphene act like massless Dirac fermions and are able to show relativistic phenomena such as Klein tunneling [3].

2.3.2 Resistance peak at Charge Neutrality Point

The linear dispersion relation which was shown in previous subsection actually leads to the unique electronic properties of graphene. Intersecting of valance and conduction bands at charge neutrality point (Dirac point) results with no band gap. This may seem to be an obstacle for transistor applications, However this property provides an ambipolar field effect where the carrier concentration can be tuned between the two carriers (electron & holes). This field effect can be induced and controlled by applying gate voltage, V_G through a layer of dielectric (bottom or top gate). Applied electric field via gate voltage tunes the Fermi level E_F as[3];

$$E_F = \hbar V_F \sqrt{\pi n} \tag{2.34}$$

where n corresponds to the charge carrier concentration.

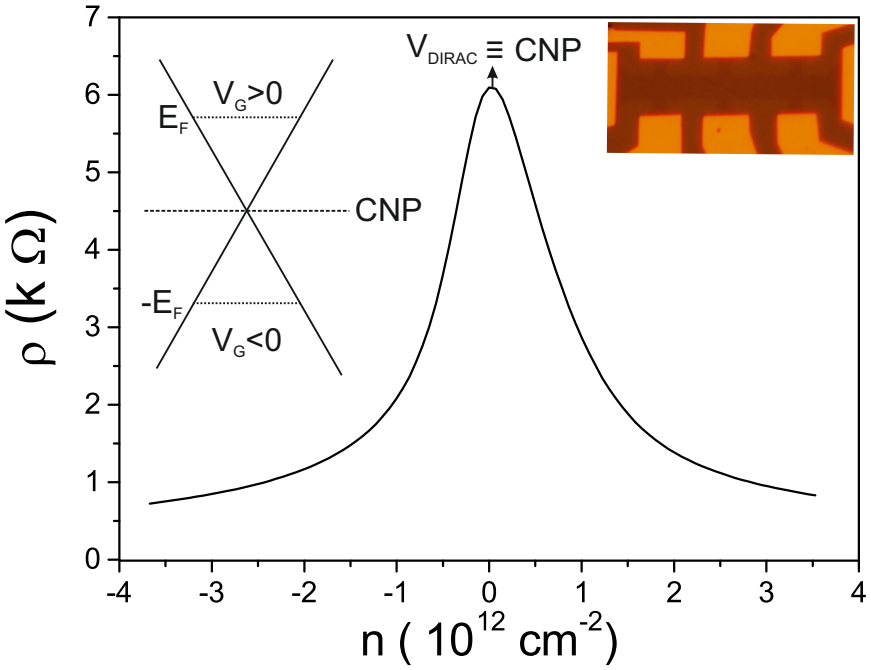

Figure 2.5: The resistivity of graphene on SiO_2 substate as function of charge carrier concentration at room temperature. Carrier concentration and the carrier type are controlled by applying back gate voltage which tunes the Fermi level. Insets: Graphene Hall bar device (Sample-CYG5-Hall) on SiO_2 substrate and schematic of the energy-momentum dispersion in Graphene. Dashed horizontal lines indicate the tuned Fermi level by applied gate voltage, V_G. Up and down cone regions corresponds to electron and hole branch, respectively

The tuned carrier concentration by applying gate voltage through the SiO_x gate can be estimated through the parallel capacitor model as;

$$n = \alpha(V_G - V_{CNP}). \tag{2.35}$$

where α corresponds to the gate capacitance per unit area divided by elementary charge;

$$n = \frac{\epsilon_0 \epsilon_r V_g}{te} \tag{2.36}$$

where ϵ_0 is the vacuum dielectric constant, ϵ_r is the relative dielectric permittivity of the gate insulator, e is the elementary charge and t is the insulator thickness. The resistance becomes maximum when the Fermi level lies at the Dirac point (Charge neutrality Point) and decreases by applying positive or negative gate voltage (tunes the Fermi level). In an ideal graphene, Fermi level is expected to be located at 0 gate voltage, $V_G = 0$. In real samples, charge impurities can dope the graphene and leads to shift in the Dirac point position either at negative (electron doping) or positive (hole doping) gate potentials. Fig. 2.5 shows the graphene resistivity as a function of carrer density. Charge carrier mobility for high densities (away from the Dirac point) can be calculated from the Drude formula for the diffusive transport as;

$$\mu = \frac{\sigma}{en} \tag{2.37}$$

2.3.3 Quantum Hall Effect in Graphene

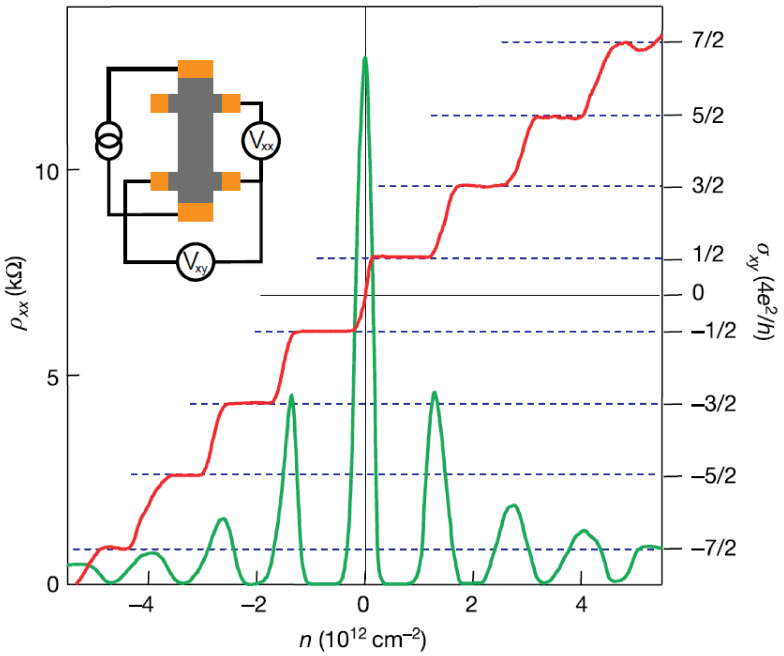

Figure 2.6: Quantum Hall effect in graphene is shown as the Hall conductance (σ_{XY}, red) in the steps of $4e^2/h$ starting from $2e^2/h$. Note that the longitudinal resistiviy ρ_{xx}(green) exhibits peaks when the Fermi level crosses a Landau Level. Adapted from Ref. [4]. Inset: Schematic of a graphene Hall bar with a typical 4 Probe measurement configuration.

When first quantum Hall measurements were utilized on graphene, physicists observed an interesting $\nu = 2, 6, 10, ... = 4(n + 1/2)$ sequence, which is deviated from its expected sequence $\nu = 4, 8, 12, ... = 4n$ for a material which has both spin and valley degeneracy. The 1/2 shift in the sequence turns out to be a result of the Dirac nature of the charge carriers in graphene. Since, the charge carriers in graphene obey Dirac equation rather than Schrödinger equation, we observe a half-degenerate zero Landau level and it causes the observed shift in the Hall sequence.

If we carefully, calculate the Landau levels in Dirac equation, one arrives at the energy levels as follows:

$$E = \pm\sqrt{2e\hbar B n {v_F}^2} \approx 36\ meV\sqrt{nB}, \quad n = 0, 1, 2, 3, ... \tag{2.38}$$

, where $n = 0$ results in an allowed energy level of 0. However, in the solution of Schrödinger equation as derived in Equation 2.21, $n = 0$ produces a non-zero energy level.

This difference actually leads an anomalous quantum Hall sequence in graphene [4]. In Figure 2.6, the anomalous sequence is shown.

Graphene's linear DOS is splitted into various Landau levels where the spacings are not equidistant as 2DEG[Fig. 2.7]. The first spacing between the Landau levels is larger than $100\ meV$ at 10 T which leads to the appearance of the quantum Hall effect even at room temperature[14].

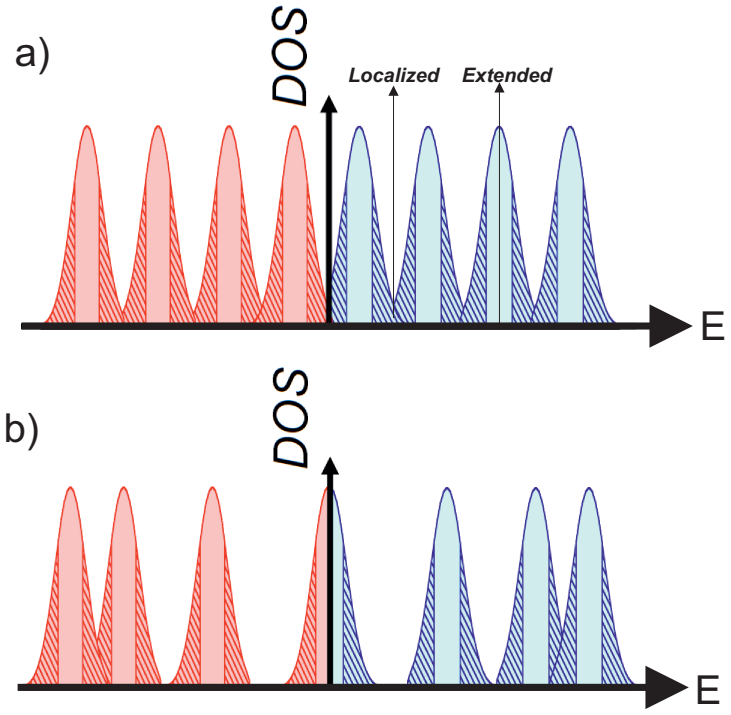

Figure 2.7: Comparison of the Landau Level (LL) spectrum. Electron branch (blue), hole branch (red). Localized states are illustrated by shaded regions where the extended states are filled regions. a) Equidistant LLs for conventional 2DEG systems. b) LL separation follows a square-root behaviour in monolayer graphene.

In an ideal system the Landau levels are infinitesimal delta peaks however those are broadened due to the impurities, temperature, e.g. When the Fermi level lies between localized states, longitudinal resistance vanishes since these states can not carry the current, and transversal resistance is quantized. As the Fermi level rises, electrons fill the next available states in the next Landau level where these extended states can carry the current. Thus, the longitudinal resistance does not vanish and the Hall resistance increases linearly with the carrier density. This process can be evaluated as a transition between the localized and extended states.

2.4 Edge channels in a quantum Hall Conductor

Quantum Hall effect can be explained by the Laughlin picture which involves the localised and delocalised states of the Landau bands and the gauge invariance properties of the system[36]. Another common way to describe the transport in the QHE effect is the edge state picture [Fig. 2.8(a)]. For the magneto-transport measurements, the samples are usually shaped into Hall bars and the edges provide lateral confinement to the 2DES. The confining potential results in an upward (downward) bending for positive (negative) Landau levels. When one Landau level intersects with Fermi level in a quantum Hall conductor, a pair of chiral edge states are created at both the upper and lower edges, which together act as an effective one dimensional channel [Fig. 2.8(c)]. Total number of these edge channels in the system equals to the number of Landau levels below the Fermi level. Only the edge channels can contribute the carrier transport in the quantum Hall regime. In a classical picture, those states are described by skipping orbits with the radius of l_B [Fig. 2.8(b). In the QH plateau regime, the electron states at the Fermi level are localized, and the scattering length is much larger than the magnetic length l_B, Thus, the backward scattering (electrons are scattered from the right-going states at the upper edge into the left-going electron sates at the lower edge, or vice versa) probability approaching zero leads to a transmission rate of one, and a reflection rate of zero. The backward scattering changes the transmission rate T of each edge channel. This transport mechanism is well described by the Landauer-Büttiker formalism that treats every channel with a corresponding transmission coefficient T and each contact with a reflection coefficient R.[37–39].

In this model, each channel carries a current of $I = \frac{e}{h}\Delta\mu_{ch}$, where $\Delta\mu_{ch} = \mu_2 - \mu_1$ gives the difference of the electro chemical potential of the two current leads. Then, M of the edge channels carry a current of $I = M\frac{e}{h}\Delta\mu$ Considering the edge channel conduction, the potential at each of the contacts μ_i $(i = 1 - 6)$ can be used to derive the longitudinal and Hall resistance. In Figure. 2.8(a) Charge carries injected through contact (1) with potential μ_1 move to contact (4) via (2) and (3). No current is extracted at contacts 2) and (3) therefore the potential remains unchanged ($\mu_1 = \mu_2 = \mu_3$). Same situation holds for the other edge where ($\mu_4 = \mu_5 = \mu_6$). There exist only one high and one low potential edge then the current is given by;

$$I = \frac{e}{h}\nu(\mu_1 - \mu_4) \tag{2.39}$$

where ν is the filling factor, which corresponds to the number of edge channels. Since the electrons injected via (1) do not reach (5) or (6), the longitudinal and Hall voltage can be

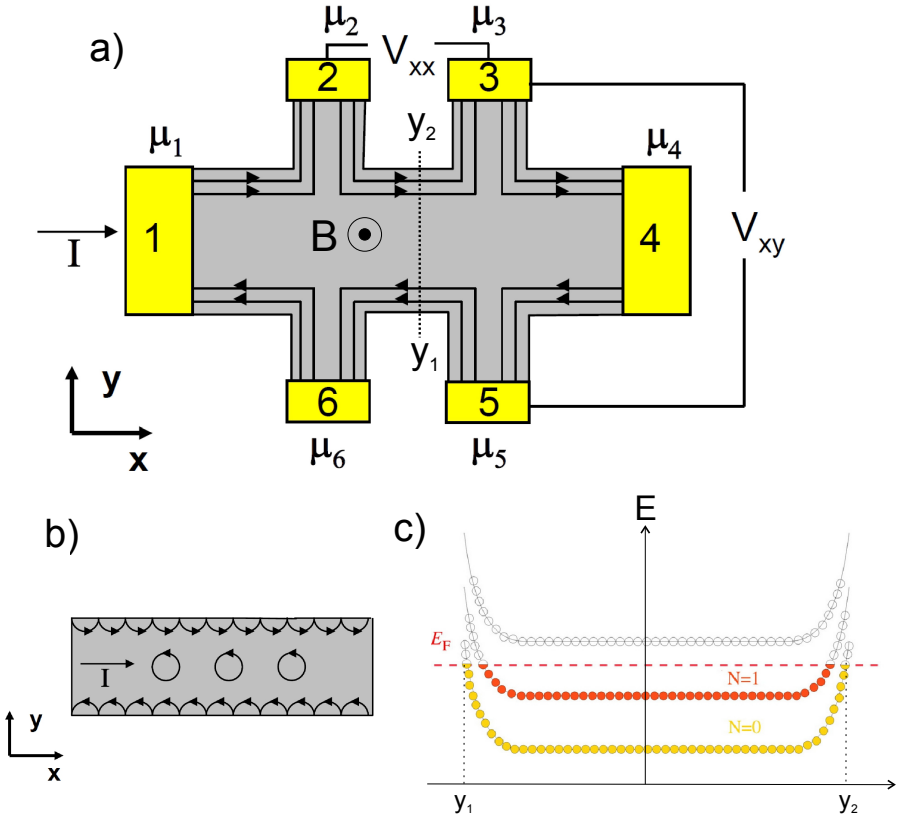

Figure 2.8: a) Scheme of the conduction via edge states (lines with arrows) in a Hall bar geometry in the quantum Hall regime. b) Electron transport in the edge channel picture, skipping cyclotron orbits at the boundaries equivalent to the edge channels in a 2DEG with finite size. c) Energy profile due to the confinement of the system in y direction where y_1 and y_2 are y coordinates of the lower and upper edge of the Hall bar, respectively. Filled circles represent the filled electron states. Intersection of the Fermi energy with the LLs leads to 1D edge channels at the edges of the 2DEG.

written as;

$$eV_{xx} = \mu_3 - \mu_2 = 0 \quad and \quad eV_{xy} = \mu_3 - \mu_5. \tag{2.40}$$

Thus, the corresponding resistances are;

$$R_{xx} = 0 \quad and \quad R_{xy} = \frac{h}{e^2\nu} \tag{2.41}$$

In General Hall resistance is the ratio of the potential at opposite edges to the current;

$$R_H = \frac{\frac{\Delta\mu}{e}}{M\Delta\mu\frac{e}{h}} = \frac{h}{Me^2} = \frac{R_K}{M} \tag{2.42}$$

For graphene $M = 2(2N+1) = 2, 6, 10..$ is given by the number of occupied Landau levels and we get the right quantization for $N = 0, 1, 2..$ level indexes. When the Fermi level is shifted through a higher Landau level an additional channel is added to the system.

Chapter 3

BREAKDOWN OF THE QUANTUM HALL EFFECT IN 2DEG

Shortly after the discovery of the quantum Hall effect [2], the physical limits of this effect in various conditions such as sample mobility, temperature and bias current were widely investigated in two dimensional electron gas (2DEG) structures [5]. In this chapter, first we will try to give an overview of the earlier works on the breakdown of the quantum Hall effect both in GaAs based 2DEG systems and graphene, respectively. A phenomenological picture without addressing the physical process that causes the the breakdown of the QHE will be discussed. Finally, We will shortly present widely used breakdown mechanisms in the literature.

3.1 A brief overview of the earlier works on the breakdown of the quantum Hall effect.

First of the depth study was made by Ebert *et al.* in 1983 and he found an abrupt onset of longitudinal voltage upon increasing bias current but only a smooth one by increasing the temperature[12]. The breakdown of the quantum Hall effect, which is observed as the abrupt increase in the longitudinal resistance with an associated loss in the quantization of Hall voltage is the major obstacle against improving the precision of the electrical resistance standard. It turned out that the most important parameters for the accuracy are temperature and current biasing. In the middle of 1980's, it has been observed a relatively high critical current densities (10 times higher) in narrow constrictions (1 μm wide, 10 μm lenght) compared to wide samples by Bliek *et al.* [40]. Later, it has been showed that the breakdown occurs after a certain travelling distance of the electrons and attributed to a heating effect that accumulates along the sample. Even when the current higher than critical current value I_c passing thorugh a Hall bar device, the longitudinal voltage V_x along the 2DES can remain as non-dissipative for the region close the electron-injection

corner, but evolves to exhibit well defined breakdown characteristics as the distance from injection corner increases[41, 42]. Another Striking features of the breakdown are its width and length dependence on the sample geometry. It has been found that for low-medium mobility samples ($10^5 - 10^6\ cm^2/Vs$) the critical current depends linearly on the width however, for medium-high mobility samples ($10^6 - 10^7\ cm^2/Vs$) the critical current follows a sub-linear trend over the sample width.[43–47]. Therefore, edge channel transport in Büttiker's formalism2.4 can not be in general applicable in the breakdown regime. Moreover, for the Hall voltages exceeding the Landau gap, the tunnelling from filled Landau level to next higher empty Landau level is pronounced, then the current starts to spread into the two-dimensional bulk which leads to breakdown of the QHE[6]. This has been observed with narrow samples and with a pronounced inhomogeneity[48–50].

Kaya *et al.* showed that the evolution of breakdown of the quantum Hall effect along a macroscopic constriction on a GaAs/AlGaAs 2DEG heterostructure where breakdown occurs as a longitudinal voltage drop only after a certain travelling length of the electrons in the constricted area in which the current becomes over critical[51]. Moreover, it has been also showed that the reverse process where hot electrons injected into an under-critical sample area cooled down after a travelling length and the QHE is recovered[52, 53]. Although a comprehensive model that explains all the experimental results on the breakdown of quantum Hall effect is still missing, the proposed models provide insight to different aspects of the breakdown. Some of these models are intra [12] and inter [6] Landau-Level transitions, electron heating [54–56], impurity mediated tunneling and relaxation of the electrons [51, 52, 57] and electron phonon interactions [58, 59].

Graphene is a two dimensional conductor which has linear energy-momentum dispersion and much larger Landau-level (LL) separation than GaAs based 2DEG for the same magnetic field [4]. This promises obtaining more precise quantization of the Hall resistance, or under less strict conditions such as higher temperatures [14] or lower magnetic fields. Therefore, graphene is a good candidate for the quantum Hall resistance metrology towards better precision and wider applications. A relative uncertainty of a few parts per billion (bpp) in the quantized resistance,

$$R_K = h/e^2 = 25812.807... \ \Omega \tag{3.1}$$

can be achieved in GaAs based Hall devices [60, 61]. Early attempts in exfoliated graphene yielded a relative uncertainty of 15 parts per million (ppm) in the quantized resistance limited by the high contact resitance togerther with a low bias current before the breakdown of the quantum Hall effect occured[62]. Since then the measured uncertainty of

R_K in the graphene based samples has been improved. Exfoliated monolayer and bilayer graphene samples yielded 0.5 ppm on SiO_x surface [15] and 6 pbb on GaAs surface [16]. Recently, 0.3 ppb accuracy has been achieved in a large area epitaxial graphene Hall device [17, 18]. Direct comparison of the resistance quantum in epitaxial graphene and in GaAs 2DEG has shown no difference within the relative standard uncertainty of 8.6 parts in 10^{11} [19]. High-accuracy quantum Hall resistance measurments in epitaxial grotwh graphene have also been recently produced by a number research groups[20–23] and even in a cryogen-free table top system in the presence of relatively low (below 5T) magnetic fields[24].

There is sufficient evidence that graphene can improve the precision in R_K and for this, the breakdown of the quantum Hall effect in graphene needs to be better understood. The physical mechanisms for breakdown of the quantum Hall effect in graphene, has been experimentally studied in a few publications. Singh *et al.* found the critical current in monolayer graphene around 1 A/m and interpreted the results as the presence of disorder-induced broadening of Landau levels and inhomogeneous charge distribution [63]. Guignard *et al.*[15] found the critical current values less then $1\ \mu A$ in bilayer graphene samples and interpreted the results through the enhanced inter-Landau- level scattering, assisted by large local electric fields in the presence of charged impurities. On the other hand, a significantly higher breakdown current density of 8 A/m has also been observed in exfoliated monolayer graphene and it has been related to the high energy loss rates of hot carriers which is order of mangnitude shorter than the conventional two dimensional electron gas system[64]. In this work, the bootstrap-type electron heating model proposed by Komiyama and Kawagucchi[56] has been modified according to the graphene and a critical breakdown field is predicted as;

$$E_c = j_c \rho_{xy} = \sqrt{\frac{4B\hbar w_c}{\eta e \tau_e}}, \tag{3.2}$$

where $\eta = 4$ for graphene (two fold spin and valley degeneracy and τ_e is a characteristic electron- phonon energy relaxation time. It was found that $\tau_e \sim 3\ ps$ is ~ 30 times smaller than GaAs which play an inmportant role in determing the high critical breakdown current. It was also predicted that in monolayer graphene the breakdown currents could be as high as 43 A/m. Soon after, remarkably high critical current density $j_c = 43\ A/m$ at 23 T has been observed in polymer gated epitaxial graphene samples in which resulting critical current values scale with the magnetic field as $I_c \propto B^{3/2}$[65] consisted with the studies and early experiment results[60, 66–68] on the 2DEG systems predicted by the breakdown models[6, 56].

Considering all the results, further work necessary in particular for the detailed understanding of the microscopic processes in the quantum Hall effect breakdown.

3.2 Current distribution and the electrical breakdown of the quantum Hall effect

Since the quantum Hall effect[2] is observed at liquid helium temperatures for the conventional 2DES, a sufficient increase in temperature certainly causes the breakdown of the effect. Here, we will discuss only the electrical breakdown of the quantum Hall effect. When the sample current is increased, the quantum Hall plateaus and the regions of $\rho_{xx} = 0$ starts to shrink[66, 69]. This shrinking is shown in Fig. 3.1(a) at filling factor $\nu = 2$, when the current is increased from $5\ \mu A$ to $50\ \mu A$ for this GaAs based 2DEG sample. The quantum Hall effect breaks down, if the current exceeds a critical value. When this happens, the quantum Hall plateaus disappear simultaneously, and at the corresponding magnetic field values the ρ_{xx} has finites values ($\rho_{xx} \neq 0$). This breakdown behaviour can also be observed in the current-voltage (*I- V*) characteristics of the quantum Hall devices as shown in Fig. 3.1(b) for $\nu = 2$. When the sample current exceeds the critical current I_c, a sudden increase of V_{xx} (or longitudinal resistance,ρ_{xx}) by several orders of magnitude occurred and leads to the breakdown of the QHE.

The conductance of two-dimensional systems in the presence of high magnetic fields had been evaluated from the theoretical point of view by Ando[70–73] and Gerhardts[74, 75] in the middle of seventies by taking a Kubo-formalism into consideration for homogeneous systems with short-range scatters. Here the transport was regarded in a local picture by assuming the entire system involved in the charge transport. One of the first theoretical works depending on the same idea was able to explain some of the exact properties of the Hall conductivity in the the 2DES in strong magnetic fields leading that the σ_{xy} should be exactly the integral multiple of e^2/h when the Fermi energy lies in the localized regime[76]

As we discussed earlier, in the presence of magnetic filed, the electric transport properties of the 2DES are determined by conductivity (or resistivity] tensors $\widehat{\sigma}$ (or $\widehat{\rho}$). For a homogeneous system, the components ρ_{xx} and ρ_{xy} of the resistivity tensor are independent of the position inside the 2DES and define the relation between the electric field $\vec{E}$ and the current density $\vec{j}$ according to ;

$$\vec{E} = \widehat{\rho}.\vec{j} \tag{3.3}$$

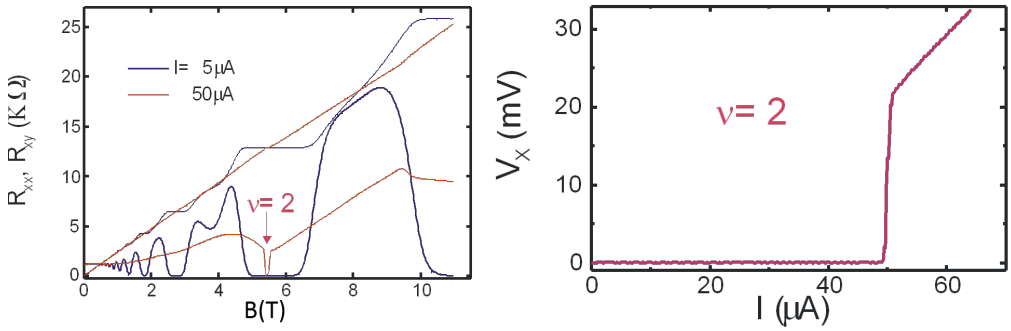

Figure 3.1: Breakdown of the quantum Hall effect in GaAs based 2DES. a) If the current exceeds a critical value, quantum Hall effect breaks down as the Hall plateaus disappear and ρ_{xx} shrinks and has a finite values. b) I-V characteristics of the QH device. For the critical current I_c the longitudinal voltage V_x increases by several orders of magnitude rapidly rather than a gradual transition. Figures adapted from *Kaya, Nachtwei, von Klitzting, 1998.*

Although, all the considerations are purely phenomenological which can not address the physical process responsible for the sudden increase of ρ_{xx}, phenomenologically it is possible to show how the breakdown evolves. In the ideal case of the QH regime, the tensor components of ρ_{xx} and ρ_{xy} can be given as;

$$\rho_{xx} = 0, \quad \rho_{xy} = h/ie^2. \tag{3.4}$$

As the current flows only in the x-direction, the y-component of the current density is always zero $j_y = 0$, and the tensor relation $\vec{E} = \widehat{\rho}.\vec{j}$ then forms as;

$$\begin{pmatrix} \vec{E}_x \\ \vec{E}_y \end{pmatrix} = \begin{pmatrix} 0 & \frac{h}{ie^2} \\ -\frac{h}{ie^2} & 0 \end{pmatrix} \begin{pmatrix} j_x \\ 0 \end{pmatrix} = \begin{pmatrix} 0 \\ -\frac{h}{ie^2} j_x \end{pmatrix} \tag{3.5}$$

The Hall angle Θ is defined as the angle between the Hall field and the current direction. As shown in Fig. 3.2(a), in the quantum Hall regime the electric Hall field is perpendicular to the current flow direction, hence the interior power dissipation per unit area is zero:

$$\frac{\delta P_i}{\delta A} = \vec{j}.\vec{E} = \begin{pmatrix} j_x \\ 0 \end{pmatrix} . \begin{pmatrix} 0 \\ -\frac{h}{ie^2} j_x \end{pmatrix} = 0 \tag{3.6}$$

The current flows without dissipating in the sample interior when the Hall angle is $\Theta = 90°$. Because of the voltage distribution, shown with "-" and "+" signs, the equipotential lines have to cross through the diagonally opposite corners of the Hall bar. At these corners the Hall angle is $\Theta \neq 90°$, so that dissipation takes place and leading strongly confined hot spots[77]. Thus, the total power dissipation is not zero ($P_t = \rho_{xy} I^2$) and occurs only at the hot spots. It is obvious that ρ_{xx} is several order of magnitude smaller than ρ_{xy} in the quantum Hall regime for the current densities below the breakdown current

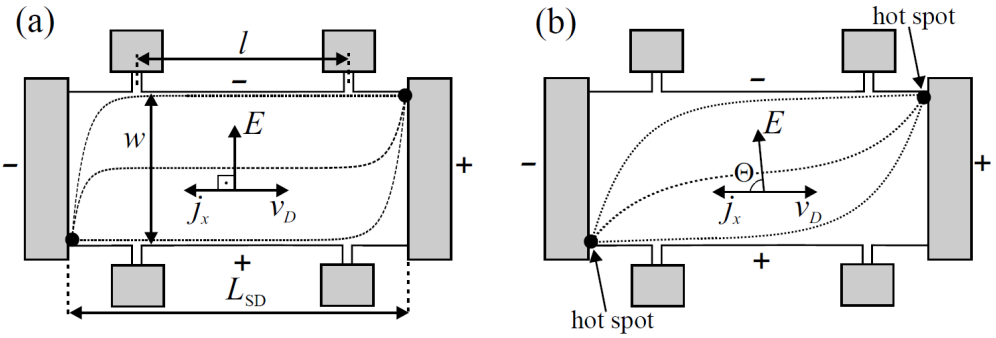

Figure 3.2: Schematic view of a Hall bar realized through a 2DES under QH conditions. a) The Hall angle Θ is $90°$, all dissipation occurs near the current contacts not in the sample interior in the QH regime where $j_x < j_c$. b) The Hall angle is $\Theta < 90°$, and the dissipation occurs partially in the sample interior in the breakdown regime where $j_x > j_c$. Full, dahsed lines correspond to equipotential lines. Figure is adapted from[5].

densities ($j < J_c$). As a result, the total dissipation is significantly high in contrast to the dissipation occurred in the sample interior. Hence, the breakdown of the quantum Hall effect can be described as a rapid increase in longitudinal resistance by several orders of magnitude $\rho_{xx} > 0$ and $\rho_{xy} \cong h/ie^2$ if the current density exceeds the critical value, $j > j_c$. Above the critical current density, an onset of the dissipation in the inner area can be observed due to the non-vanishing component of the electric field, $\vec{E_x}$ in the current flow direction. Eventually, the Hall angle deviates from $90°$ in the interior of the sample Fig. 3.2(b) and internal dissipation occurs. Tensor relation becomes;

$$\begin{pmatrix} \vec{E_x} \\ \vec{E_y} \end{pmatrix} = \begin{pmatrix} \rho_{xx} & \rho_{xy} \\ -\rho_{xy} & \rho_{xx} \end{pmatrix} \begin{pmatrix} j_x \\ 0 \end{pmatrix} = \begin{pmatrix} \rho_{xx} j_x \\ -\rho_{xy} j_x \end{pmatrix} \tag{3.7}$$

In the sample interior, the dissipated power per unit area then;

$$\frac{\delta P_i}{\delta A} = \vec{j}.\vec{E} = \rho_{xx} j_x^2. \tag{3.8}$$

This internal dissipation over the entire sample can be evaluated as $P_i = \rho_{xx} j_x^2 L_{SD}/w$ and the total dissipation power including the dissipation near the contacts $P_H = \rho_{xy} I^2$, then;

$$P_t = P_H + P_I = (\rho_{xx} L_{SD}/w + \rho_{xy}) I^2. \tag{3.9}$$

There is no ρ_{xx} term in the latter term, because $\rho_{xx} \ll \rho_{xy}$ holds even for the breakdown of the QHE ($\rho_{xx.} \approx 1 - 2\ k\Omega, \rho_{xy} \approx 6.45 - 25.8\ k\Omega$ for the filling factors $4 \geq \nu \geq 1$). Using the $\rho_{xy}/\rho_{xx} = tan\Theta$, relative dissipation of the sample interior can be defined as;

$$\frac{P_i}{P_t} = [tan(\Theta)w/L_{SD} + 1)]^{-1} = \left(\frac{\rho_{xy}}{\rho_{xx}}\frac{w}{L_{SD}} + 1\right)^{-1} \approx \frac{\rho_{xx}}{\rho_{xy}}\frac{L_{SD}}{w}. \tag{3.10}$$

Final equation provides a useful experimental criterion for the definition of the breakdown in Hall bars[5]. There exists a pre-breakdown regime in which ρ_{xx} increases slightly before the QHE breaks down[12]. The threshold value ρ_{xx}^{th} which corresponds to a certain Hall angle Θ or a limit of relative dissipation in the sample interior, should be chosen well above the pre-breakdown values, typically of the order of a few Ω.

3.3 Physical Proposals for the breakdown of the QHE

The Critical Hall filed of the QHE breakdown in the experiments varies from sample to sample (strongly depends on the local inhomogeneities[12, 13, 15, 63, 78–81] and most of the models try to explain the sudden onset (which is absent in graphene) of the breakdown. We will shortly present widely used breakdown mechanisms in the literature.

Quasi-elastic inter-Landau-level scattering

Eaves *et al.*[6] proposed a simple mode based on quasi-elastic inter-Landau-level scattering (QUILLS). Main idea of breakdown of the quantum Hall effect through the QUILLS process is based on the electron tunnelling process from highest occupied to the lowest unoccupied Landau level in the presence of strong Hall fields. The strong Hall filed bends the Landau level and associated wave function, $\phi_n(y - y_0)$ corresponding to highest filled Landau level can overlap with an empty state, $\phi_{n+1}(y - y_0\prime)$ of the next Landau level. This leads to the tunnelling of the electron from $n - th$ Landau level to the $(n + 1) - th$ Landau level [Fig. 3.3].

This tunnelling is being enhanced dramatically by the Landau level bending due to the external strong enough electric field leading to the breakdown of the QHE. If the spatial extent of the oscillator wave function Φ_n is given by the classical amplitude of motion as $A_n = (2n + 1)^{1/2} l_B$. The overlap condition determines the critical field E_C as ;

$$eE_c(A_n + An + 1) = \hbar\omega_c, \quad E_c = \frac{\hbar\omega_c}{el_B[(2n + 1)^{1/2} + (2n + 3)^{3/2}]} \tag{3.11}$$

The resulting critical current then;

$$\begin{aligned} I_{cr} &= \frac{e^2}{h} i \frac{\hbar\omega_c}{el_B[(2n + 1)^{1/2} + (2n + 3)^{3/2}]} \\ &= \frac{e^2}{h} i \frac{\sqrt{\hbar e}B^{3/2}}{m^\star[(2n + 1)^{1/2} + (2n + 3)^{3/2}]} \end{aligned} \tag{3.12}$$

Although this formula succeeds to find the magnetic field dependence of $B^{3/2}$ measured in some of the experiment, in general it gives a too high (2 order of magnitude higher) critical current values. This is due to the fact that this simple model does not consider the impurities and the microscopic inhomogeneities in the real sample. It has been shown that the inter Landau level tunnelling can be strongly enhanced by spatially extended impurities[15, 81–84].

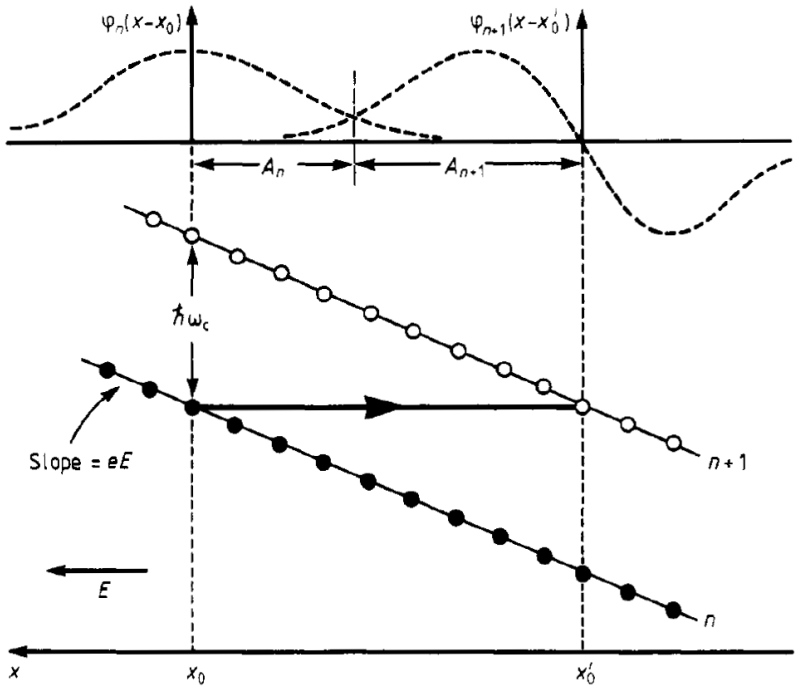

Figure 3.3: Landau level bending under strong electric field along y-direction. The condition for quasi-elastic scattering from filled Landau level n to empty level $n+1$ and spatial overlap between the oscillator eigenfunctions. The wavefunctions shown here correspond to the two lowest Landau levels. Adapted from Ref [6]

Intra-Landau-Level scattering by phonon emission

Streda *et al.*[58] proposed a possible model for the breakdown of the quantum hall effect by a spontaneous emission of phonons. An energy exchange has been considered between the 2DES and the lattice phonon systems via collective intra Landau level transitions. Here the electrons moving with a drift velocity higher than the speed of sound in GaAs exhibit a Cherenkov-like phonon emission effect. The critical breakdown current derived from this model;

$$\frac{I_c}{d} = \frac{e^2}{h} i v_s B \frac{d_{eff}^n}{d} \tag{3.13}$$

where d is the sample width, $v_S = 2470 ms^{-1}$ is the sound velocity of the GaAs, d_{eff} is the effective current carrying width depends on the impurities and homogeneities. Although, this model gives same order of magnitude critical current values as found in experiments, magnetic field dependence is proportional to B rather than $B^{3/2}$.

Electron heating

For the early experimental results, electron heating is attributed the breakdown of the QHE[12]. However, for also other models depending on the electron heating do not require a precise knowledge about the actual heating mechanism[56, 85, 86]. Basic idea is the balance between the energy gain and loss processes of the hot electrons near the breakdown of the QHE. Experiments show that the Hall field E_y greater than the critical field E_c, (not far away from the E_c, Hall angle is nearly $90°$), σ_{xx} is finite but $\sigma_{xx} \ll \sigma_{xy}$ and $E_x \ll E_y$ still hold. The power per unit area generated by Joule heating is;

$$\vec{j}\vec{E} = \sigma_{xx}(E_x^2 + E_y^2) \approx \sigma_{xx} E_y^2 = \rho_{xx} j^2. \tag{3.14}$$

The energy gain from the Joule heating causes the increase of the local electron temperature $T_e(\vec{r})$ at position $\vec{r}$ from the lattice temperature T_L. The energy loss rate is in general a function of the local electric field and the local electron and lattice temperature, Komiyama *et al.* described the energy difference of electron at temperature T_e and T_L over a relaxation time τ [54, 56]. Thus the electron temperature can be determined from the power balance equation;

$$\frac{Z(T_e) - Z(T_L)}{\tau} = \sigma_{xx} E_y^2 = \rho_{xx} j^2. \tag{3.15}$$

The energy Z can be calculated via the energetic distribution of the electrons within the

bands;

$$Z(T) = \int_{E_F}^{\infty} (\varepsilon - E_F) D(\varepsilon) f(E) d\varepsilon \tag{3.16}$$

Where $D(\varepsilon)$ corresponds to density of the states and $f(\varepsilon) = \{exp[\varepsilon - E_F)/k_B T] + 1\}^{-1}$ the Fermi-Dirac distribution. Moreover, the conductivity, $\sigma_{xx}(\vec{r})$ can be assumed to be position dependent where it depends on the local electron temperature and local electric field $E_y(\vec{r})$ as

$$\sigma_{xx}(\vec{r}) = \sigma_{xx}[T_e(\vec{r}), E_y(\vec{r})]. \tag{3.17}$$

Then heating model can be represented as a differential equation;

$$\frac{Z(T_e) - Z(T_L)}{\tau} = \sigma_{xx}[T_e(\vec{r}), E_y(\vec{r})] E_y^2(\vec{r}). \tag{3.18}$$

System can keep its equilibrium (stable) state for a stationary state fluctuations where the small dissipation due to the small increase in electron temperature can be balanced with energy loss rate. This condition can not be satisfied for a sudden increase in electron temperature and conductivity. Komiyama *et al.*[56] used this model setting $T_L = 0\ K$ and considering infinitesimally small broadening in Landau levels a thermally activated conductivity to calculate a critical electric field E_c where an abrupt jump of the electron temperature happens.

$$\sigma_{ac}(T) = \frac{e^2}{h} exp\left(-\frac{\hbar\omega_c}{2k_B T}\right), \quad E_c = \sqrt{\frac{2\hbar}{m^*\tau}} B \tag{3.19}$$

Calculated curves for the conductivity are in qualitative agreement with the experimental curves. In certain conditions, the function $\sigma_{xx}(E_y)$ obtained by this method can be an S-shaped multi-value function near the QHE breakdown.

Chapter 4

DEVICE FABRICATION

In this chapter, micro/nano fabrication methods of the quantum devices are described in detail. In this thesis, all the samples consist of exfoliated single layer graphene sheets. The micro/nano scale devices fabricated during this thesis require advanced fabrication techniques in a clean room environment, which are mainly performed in Sabanci University Nanotechnology Research and Application Center.

4.1 Substrate preparation and Cleaning

The fabrication procedure starts with placing the gold alignment marker system by following the standard metal lift-off process. Basic parts of the lift-off process are illustrated for the reader to understand the fabrication steps, which are given below as a recipe [Fig. 4.1]. The marker system basically contains 5 μm size squares above the number sets, separated by 250 μm from each other, for every 1cm x 1cm period on highly p-doped thermally grown Si/SiO_2 (285 nm) substrates (Supplied by Nova Electronic Materials) [Fig. 4.2(a)]. This marker system provides very precise coordinate positioning while designing the device contacts which will be discussed in the contact designing section 4.4.1.

In this thesis, most of the lithography processes have been carried out with Vistec EBPG 5000+ES 100 kV Electron beam lithography (EBL) system which provides very low spot size of $\approx 2\ nm$, high exposure currents (up to $200\ nA$) and very accurate alignment (Less than $20\ nm$ in the second ebeam step) with its laser interferometer stage. A standard operating procedure of the Vistec EBPG500+ EBL system is given in Appendix. A. EBL plays the most critical and flexible role for the micro-nano structuring of the device applications, leading to the observation of various quantum related physical phenomena. Fabrication recipe for the cleaning and metal-marked substrate can be summarized in the followings;

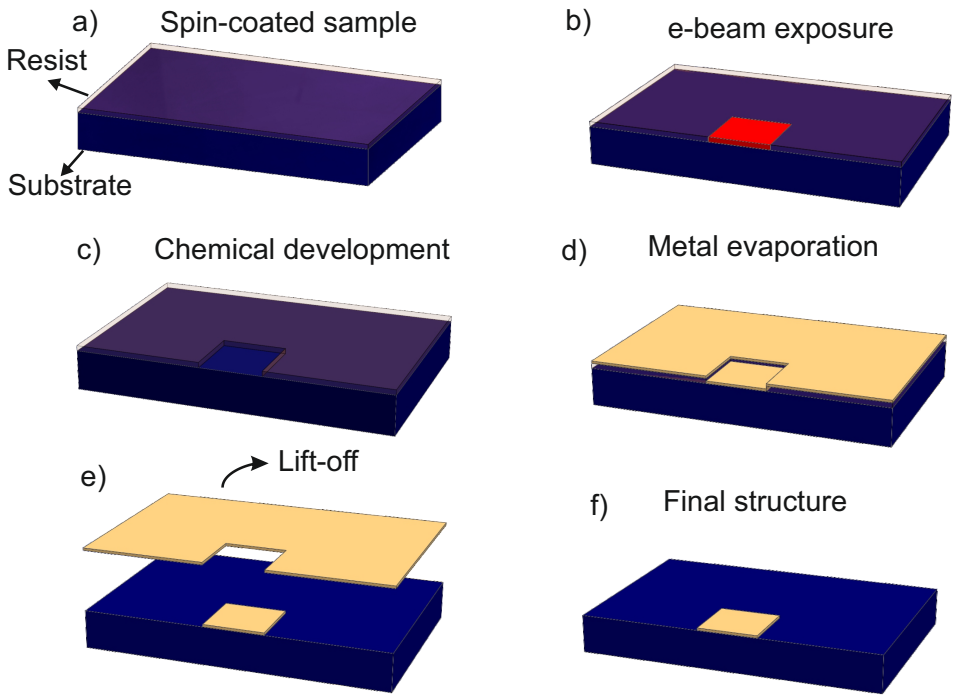

Figure 4.1: General illustrations of the standard metal lift-off process where the patterning is utilized by ebeam lithography.

Step 1: First the wafer is spin-coated with a layer of 950 Polymethyl-methacrylate (PMMA) A4 resist at 5000 rpm for 50 seconds, which results in a uniform 300 nm thick resist layer [Fig. 4.1(a)].

Step 2: Wafer is baked on a hot-plate at 170° for 5 minute to remove the excess solvent.

Step 3: Electron beam lithography (EBL) is performed to expose the markers on the wafer with an areal dose of $750\ \mu C/cm^2$ at 100 kV [Fig. 4.1(b)].

Step 4: Wafer is develop in a solution of methy isobutly ketone (MIBK) and isopropyl alcohol (IPA) in 1 to 3 volume ratio for 60 seconds then immersed into IPA for 40 seconds, rinse with IPA and dry in Nitrogen gas flow [Fig. 4.1(c)].

Step 5: After development, wafer is exposed to the O_2 plasma in a reactive ion etcher RIE (Oxford Instruments Cobra 100 Deep RIE) for a short time (≈ 5 s) to get rid of any remained PMMA residue in the develop regions with the RIE parameters; 100 W forward RF-power plasma at a pressure of 0.07 mBar with a 20 sccm of O_2 flow in the chamber.

Step 6: Wafer is placed in a metal evaporator (TORR Instruments, ebeam- thermal evaporator) then, chromium and gold metals Cr/Au (5/100 nm) are deposited after reaching the vacuum level under $\approx 5 \times 10^{-6}$ mBar [Fig. 4.1(d)].

Step 7: Wafer is immersed into acetone and left for a while in the acetone to let the acetone diffusion underneath the metal, eventually lifts the metal off. [Fig. 4.1](e). Depending on the final situation for the regions in which metal lifting problem occurs, ultrasonic vibration can be very helpful.

Step 8: After a successful metal lift-off process, wafer is spin-coated with a thin layer of 950 PMMA A2 resist before cutting the wafer into small pieces (1cmx1cm). This is an essential step which prevents the wafer surface from any damage, scratch and contamination during the dicing operation.

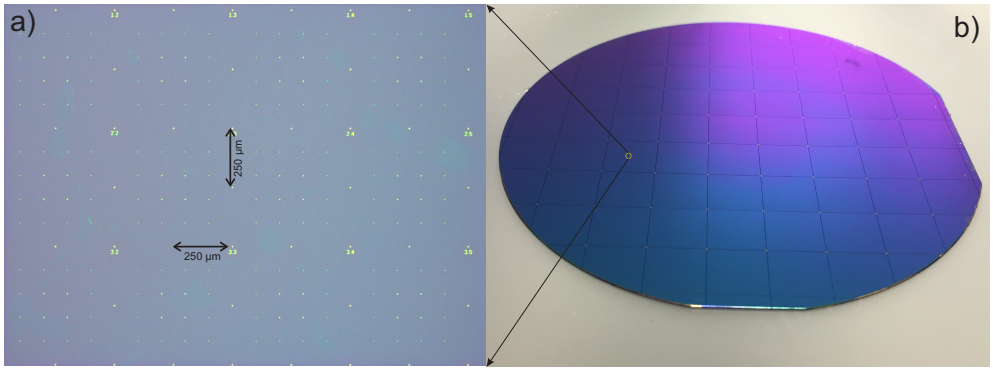

Figure 4.2: (a) Gold marker system on the substrates after lift-off. (b) 1 $cm \times 1$ cm diced pieces from the metal marked 4" wafer

Step 9: Before cleaning the substares as final step, wafer is cut into small rectangular pieces by wafer dicing machine (Disco Wafer Dicer) [Fig. 4.2(b)].

Step 10: Prior to graphene exfoliation, the substrates are cleaned following three steps. These cleaning methods:

1. *Standard Cleaning*
    - Ultrasonic ACE aggravation at room temperature for 5 minute.
    - Each sample rinses consecutively in three ACE and 3 IPA beakers for 30 seconds.
    - Dry in N_2 flow.
2. *Piranha Cleaning*
    - Substrates are immersed in a mixture of 3:1 concentrated H_2SO_4 to 35% H_2O_2 aqueous solution on a $100°C$ hot plate for 5 minutes.
    - Transfer to 2 separate deionized water (DI) beaker consecutively.

- Transfer to IPA, dry in N_2 gas flow.

3. *Oxygen Plasma*

   - The oxygen plasma parameters used in this step same as before; 20 sccm O_2 flow, 0.07 mBar pressure and 100 W forward RF-power for 1 minute.

First step is a standard method of cleaning in semiconductor industry. Second is a more aggressive one which cleans all the organic contaminations from the surface. Third one, oxygen plasma etching is a chemical process which also etches organic residues from the surface successfully. We generally perform oxygen plasma right before the graphene exfoliation. After cleaning, substrates are always kept in vacuum desiccators either at lab or cleanroom.

4.2 Graphene Exfoliation

The simple exfoliation technique to obtain a single layer isolated graphene from the bulk graphite was introduced by A. Geim and K. Novoselov in 2004[10], then it led them to win the Nobel Prize in 2010 for the the ground breaking experiments in this new inherently 2D material. The graphene flakes obtained by this simple method are the most clean and highest quality crystalline structure among all other production methods. Some reliable methods have been developed to produce large area graphene with high yield such as epitaxial growth on silicon carbide (SiC) samples[87–89] and chemical vapour deposition (CVD)[90]. However, these methods suffer from the defects, impurities or other challenging issues during the production. Epitaxial growth seems much promising method for the electronic applications compared to the CVD graphene which has relatively lower carrier mobilities. During my Phd studies, we also spent a significant amount of time on the production of high quality epitaxial graphene in ultra high vacuum conditions (UHV). A new technique which eventually provides a control mechanism on the thickness and the quality of uniform graphene sheets was introduced. However, these studies are not the main topics of this thesis. Interested readers can find the detail results in our published works in Ref. [91, 92].

In the scoth-tape method, the number of graphene flakes per sample area and size of these flakes are limited and relatively change from person to person depending on the hands-on experience. Everyone has his/her own optimization techniques which can be experienced with time. As a graphite source, Natural graphite flakes in various size (2-5 mm, 5-10 mm, 20-25mm by NGS Naturgraphit GmbH), Kish Graphite or Highly Oriented Pyrolytic Graphite (HOPG) can be used.

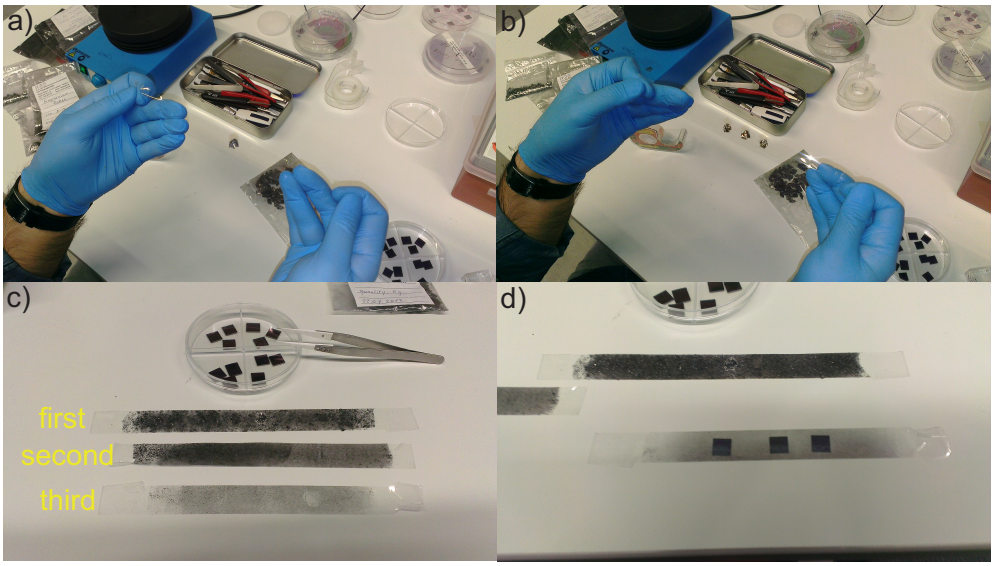

Figure 4.3: The mechanical exfoliation of graphene: (a-d) shows the production of graphene by mechanical cleavage method just using the scotch tape.

We generally use the natural Graphite flakes in 5-10 mm sizes. Here, I will try to describe the technique that I use in the following steps;

Step 1: A piece of graphite is first put on the sticky tape (Scotch Magic tape) and the tape is being stuck to itself and peeled off. Remaining thin graphite which has clean layers on its end-surface is removed from the tape and placed in a new scotch tape [Fig. 4.3(a)].
Step 2: After this, tape is continuously stuck to the clean side of itself and peeled off, thus the graphites can be divided into small and thin pieces [Fig. 4.3(b)].
Step 3: This process keeps continuing until the graphite is homogeneously covered on the tape. To obtain an optimum graphite thickness (Contrast on the tape, "depends on experience"), exfoliation can be repeated with a 2^{nd} piece of clean tape by sticking it to the 1^{st} one, if necessary, then the 3^{rd} one on the 2^{nd} one [Fig. 4.3(c)].
Step 4: As a final step, second or third tape is put on the previously prepared clean SiO_x substrates and small pressure is applied by thumb finger then the tape is removed away slowly [Fig. 4.3(d)].
Then the substrate is investigated under an optical microscope in order to find single layer graphene flakes in suitable sizes for device fabrication. Interestingly, as a single atomic thick graphene layer (thinnest material in the world) which has an optical transparency of $\sim \%98$[93], appropriate oxide thickness underneath $\sim 300\ nm$ gives enough contrast for the identification of graphene under white light optical microscope[94]. With this optical characterization method, it is possible to identify the thickness and position (markers on the substrate) of graphene. We are able to identify the thickness of the graphene sheets un-

der optical microscope in general. In order to be sure about the number of layers, Atomic Force microscopy (AFM)[10, 95] or Raman spectroscopy methods can be utilized[96]. In our facility, we use the Raman Spectroscopy (Renishaw's Raman Spectroscopy Instrument) to determine the number of graphene layers.

4.3 Raman Analysis of Graphene samples

Raman spectroscopy is a non-contact characterization which gives not only detailed information about the number of layers in graphene, but also provides information about the doping level, strain percentage and defect concentration[96, 97]. Raman spectrum of the graphene contains two significant peaks; G band at $\sim$ 1580 cm^{-1} and 2D band at $\sim$ 2700 cm^{-1} [Fig. 4.4]. Graphene layers are determined depending on the intensity ratio and full width at half maxima between these peaks. For single layer graphene; the intensity of G peak is smaller than the intensity of 2D peak, the ratio almost approaches 2 where it is almost 1 for bilayer and less for few layer of graphene sheets. The full width at half maxima (FWHM) and the position of 2D peak are also utilized to determine the number of layers. Shifts in the positions of these peaks can be used to determine the doping and strain level in graphene, as well. D peak around $\sim 1370cm^{-1}$, so called defect peak, is absent in high quality crystalline graphene, however it appears in defective graphene sheets.

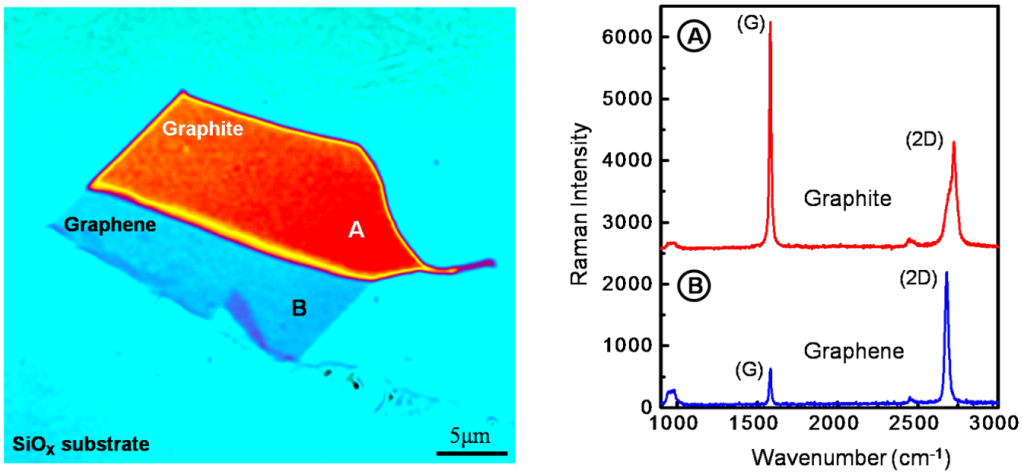

Figure 4.4: (a) Optical microscope image of the graphene sheets. Region A (red) shows the thick graphene and region B (almost transparent) shows the monolayer graphene. (b) Raman spectrum of the specified regions; 2D intensity is higher than the G peak intensity in region B and the ratio between them exceeds 2 (single layer). 2D peak intensity is lower than G peak in region A corresponds more than few layers of graphene. One can note that the defect peak is absent for both regions around D peak $\sim 1370cm^{-1}$.

4.4 Contact fabrication

After identifying a single layer graphene in suitable sizes for device fabrication, we design the contacts on the graphene sheets by using the LayoutEditor Computer-Aided Design (CAD) program. We use the bilayer resist process (Low molecular weight as a bottom layer (high sensitive), high molecular weight (less sensitive as a top layer), which provides more pronounced undercut profile that makes the lift-off process easier. Design and the fabrication of the contact processes flows will be given in the next subsections, in detail.

4.4.1 Designing the contacts

- We start taking the optical images of the graphene sheet on the substrate in various magnifications (5X, 10X, 20X, 50X, 100X).
- Then, we open previously prepared 20 pads general contact design with the markers that are same with previously evaporated metal markers on the substrate [Fig. 4.5(a)].
- We import the optical images into the background of the LayoutEditor program and align them to the markers in the layout. These markers are going to be used in the real alignment during e-beam exposure. We carefully make the designs on the graphene sheets by considering the other graphite pieces around to prevent any short-circuits between the probes [Fig. 4.5(b)].

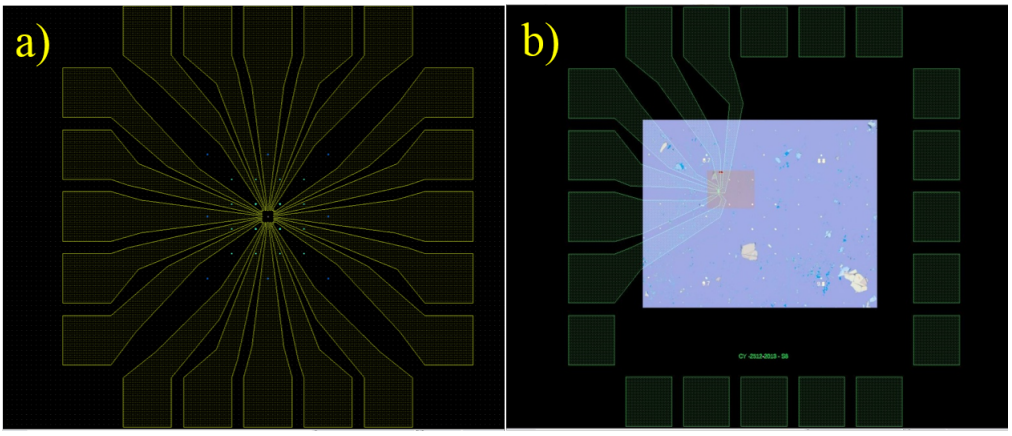

Figure 4.5: (a) Previously prepared 20 pads generic contact design for the graphene fabrication, Blue squares correspond to the main alignment markers to be used during the ebeam exposure. (b) Adjusted contact design for the specific graphene sheet on the substrate after aligning the 10X and 50X optical microscope images.

When the design is finished, it is exported as gdsII format and imported into the BEAMER (GenISys) program which allows the one make all the ebeam corrections. Then

the file is exported as a generated pattern file (gpf) which is a suitable exposure format for the Vistec EBPG 5000+ EBL system.

4.4.2 Fabrication of the contacts

- We start by spin coating the MMA (8.5) EL11 co-polmyer (Low Molecular Weight)at 5000 rpm for 50 seconds, which results in a uniform $\sim 400\ nm$ thick resist layer.
- Sample is baked on a hot-plate at $170^{\circ}\ C$ for 5 minutes to remove the excess solvent.
- Then the second layer of 950K PMMA A2 (High Molecular Weight) is spin-coated at 5000 rpm for 50 seconds which results in a uniform $\sim 70\ nm$ resist layer.
- Sample is again baked on a hot-plate at $170^{\circ}\ C$ for 5 minutes.
- Electron beam lithography (EBL) is performed to expose the contacts on the wafer with an areal dose of $650\ \mu C/cm^2$ at 100 kV. Vistec EBPG 5000+ ebeam lithography system is purely dedicated to perform ebeam lithography rather than the image inspection. It is very powerful and user friendly machine for the e-beam exposure in comparison with the attached systems to scanning electron microscope. One only needs to align the sample height and rotation of the sample (rotation alignment mistake must be less then 2°) under a special optical microscope. After loading the substrate into the system, it is just enough to tell the position of the lower left marker in your substrate then it does the rest itself with its automatic software[Appendix. A].
- Sample is developed in a solution of MIBK:IPA (IPA) in 1:3 volume ratio for 60 seconds, then 5 seconds in 1:1 ratio of MIBK:IPA, immersed into IPA for 40 seconds, rinsed and dried gently by Nitrogen gas flow [Fig. 4.6(b)].

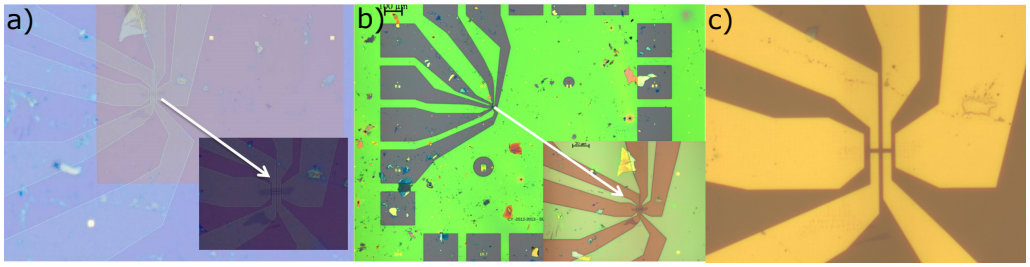

Figure 4.6: Optical microscope images from design to fabrication. (a) Completed contact design on the single layer graphene sheet, inset: A closer look at the contact design. (b) Sample after developing, inset: A closer look at the develop regions. (c) After metal evaporation and lift-off.

- Sample is placed in thermal metal evaporator for the metal evaporation. Chromium and gold metals Cr/Au (2.5/100 nm) are deposited after reaching a vacuum level of $\approx 2 \times 10^{-7}$ mBar.

- Sample is immersed to acetone in a glass petri-dish for lift-off process. We usually leave the sample inside the acetone overnight to let the acetone diffuse into the resist layers completely for achieving a clean and successful lift-off [Fig. 4.6(c)]. Therefore, it does not require any ultra-sonic vibration which may cause some problems such as; flipping graphene over, detaching of graphene from the surface or any damage to fine tuned contact structures.

After this final step, fabrication of a graphene hall-bar or giving any desired shape on the graphene sheet requires another e-beam lithography and oxygen plasma steps which will be discussed with combining the old fabrication procedure in the next section in detail.

4.5 Fabrication before Vistec EBPG5000+ EBL System

During my first years at Sabanci University, Nanotechnology Research and Application Center had not been present. We were carrying out our device fabrications in a small cleanroom inside the Sabanci University Faculty of Engineering and Natural Sciences building. E-beam applications were utilized by Nabity Pattern Generation System (NPGS), which is attached to Zeiss Leo Supra 35VP field emission Scanning Electron Microscopy(SEM) in faculty building.

4.5.1 Graphene Hall-bar Device Fabrication

- Exfoliated graphene on the substrate is aligned at the center of the designed marker system via optical lithography. Negative lithography is performed to achieve a negative profile in the resist profile in order to have easy lift-off. Negative optical lithography recipe: Sample is spin-coated with AZ5214E (Image reversal optical resist) at 6000 rpm for 50 seconds leading $1.2\ \mu m$ resist thickness. The sample is then baked on a hotplate at 90° for 2 minutes. Then the sample is illuminated (UV) through the optical-mask for 20 seconds (corresponding $\sim\ 50mjoule$) energy. Sample is baked on hotplate 115° for 2 minute again and illuminated by a second exposure to reverse the profile by UV with a corresponding energy $> 150mjoule$. Finally sample is developed in AZ726MIF which is a Tetramethylammonium Hydroxide (TMAH) based developer for 70 seconds.

- 5 nm Cr and 100 nm Au is evaporated and first lift-off process completed for the markers around the graphene [Fig. 4.7(a)].

- Graphene Hall-bar and little contact designs are designed by DesignCAD program [Fig. 4.7(c)].

- Sample is spincoated with 950 PMMA C2 at 5000 rpm which results in $\sim 90\ nm$ resist thickness.

- Sample is baked at 170° during 5 minutes.

- Little ohmic-contacts are exposed via NPGS system with an areal dose of $200\ \mu C/cm^2$ and $20\ pA$ beam current with $10\ \mu m$ aperture of SEM at 20 kV. Before Vistec EBL system, we were not able to expose all the contact design in one shot because of the some issues such as long exposure times due to low beam current and precise positioning during the exposure. We could get max 30 pico A beam current at 20 kV whereas we are able to write the full pattern with the high resolution adjustments up to 50 nano A via Vistec EBPG 5000+.

- Sample is developed in MIBK:IPA- 1:3 for 1 minute. Then immersed into IPA for 1 minute, rinsed with IPA and dry in nitrogen gas flow.

- After development, 2 nm Cr and 30 nm Au are deposited when the vacuum level reaches $\approx 3 \times 10^{-7}$ mBar inside the evaporator and sample is put into acetone for lift-off [Fig. 4.7(d)].

- After successful lift-off, second ebeam lithography is performed to give the hall-bar shape. There exist two ways of performing this exposure step. One is considering the positive tone(regions exposed to ebeam become soluble during development) standard PMMA resist and the second one is negative tone (regions exposed to ebeam become insoluble during development) Hydrogen Silsesqioaxene (HSQ) resist. If the PMMA resist is preferred, the region out of the the Hallbar shape should be exposed to let the PMMA on the graphene as a hall bar shape which will prevent the shape during oxygen plasma etching. If the HSQ as Fox 12 (Flowable Oxide) is preferred as a negative e-beam resist for this step, then only the Hall bar shape is going to be exposed where the rest will be developed in a TMAH based developer. For the PMMA, 950 PMMA C2 can be used and it follows the same exposure and development procedures. For the HSQ procedure; Sample is spincoated with HSQ-Fox 12 at 5000 rpm and baked at two steps; first at $150^{\circ}C$ for 2 minutes at $220^{\circ}C$ for 5 min. E-beam exposure is performed with an areal dose of $250\ \mu C/cm^2$ with

30 pA beam-current at 20 kV acceleration voltage (800 $\mu C/cm^2$ at 100 kV for 950 PMMA C2 via Vistec). Then the sample is developed for 70 seconds inside the 726MIF developer, rinsed in DI water then dried in nitrogen gas flow. A schematic of the process flow is given in Fig. 4.8.

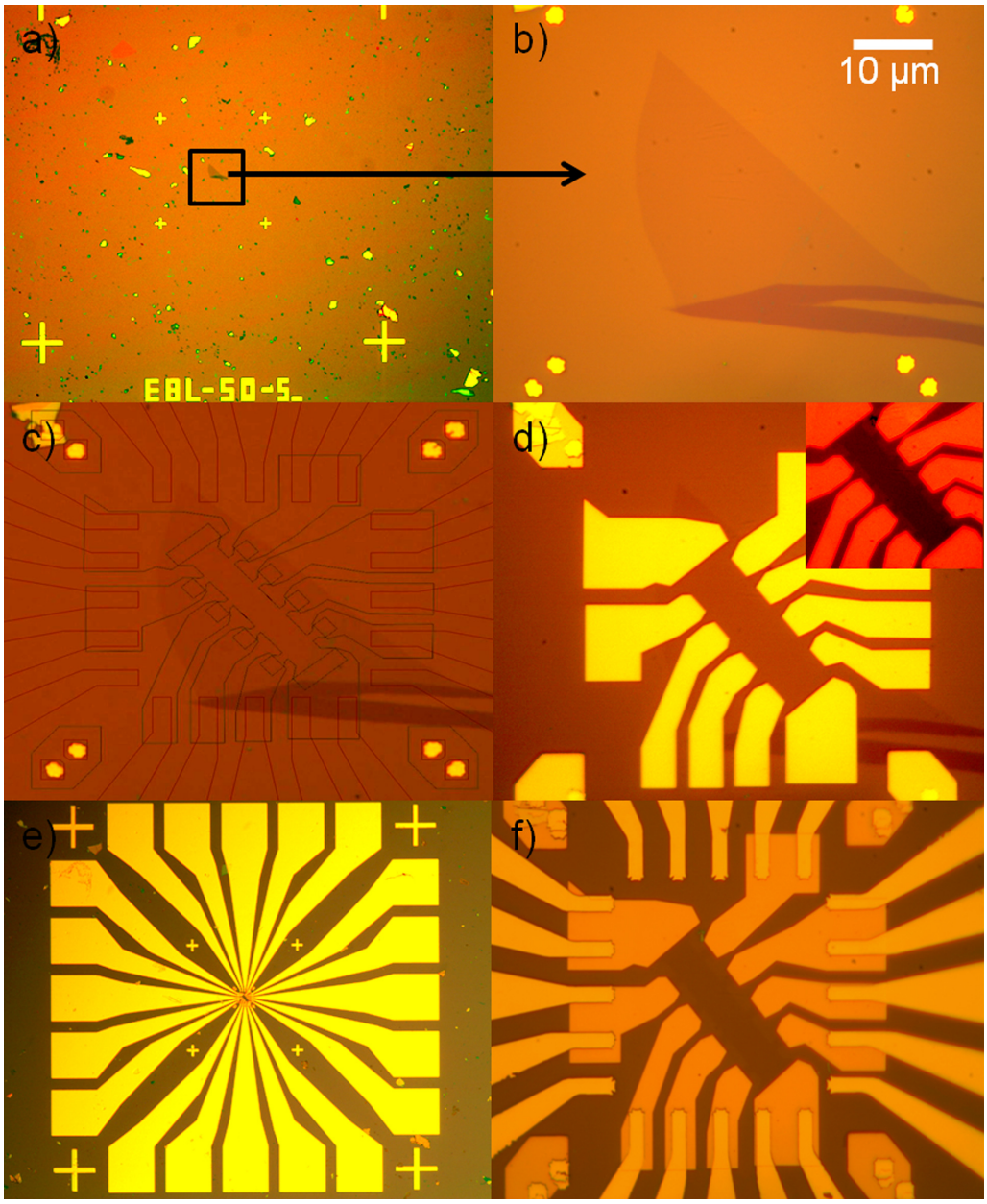

Figure 4.7: Optical microscope images of the graphene Hall-bar device fabrication flow; (a) Graphene inside the metal Cr/Au(5/100 nm) alignment markers aligned via optical mask. (b) A closer look at the Graphene sheet with the double-square markers around it. (c) Graphene contact pads and Hall-bar design (d) Graphene contact pads after lift-off. Inset: Graphene Hall bar shape after oxygen plasma etching. (e) 20 pad Ohmic contacts after metal lift-off. (f) A closer look at the Hall-bar region after lift-off.

- As the shape is protected by resist on the graphene sheets, an oxygen plasma is performed during 5 seconds to etch away the undesired graphene regions with the parameters of 100 W forward RF-power plasma at a pressure of 0.07 mBar with a 20 sccm of O_2 flow in the chamber. This recipe is enough to etch a few layers of graphene sheets while it etches only 1-2 nm PMMA layer per minute and does not etch HSQ [Fig. 4.7(d)- inset]. It has been known that the oxygen plasma crystallizes the HSQ, which may become an issue while striping the HSQ from the graphene surface just by immersing the sample in acetone. Very low concentration (DI Water: HF- 50:1) of Hydrofluoric acid may help to remove the remained resist. When we faced with this kind of stripping problem, we have developed a two-layer resist combination as HSQ on top of 950 PMMA C2. After oxygen plasma, PMMA leaves the surface easily in acetone and eventually takes away the HSQ at the same time.

- Second optical lithography is performed to put the the big-Ohmic contact pads by following same negative (image reversal recipe). After development, 5 nm Cr and 100 nm Au are deposited at the vacuum level of $\approx 5 \times 10^{-6}$ mBar inside the evaporator and sample is put into acetone for lift-off [Fig. 4.7(e),(f)].

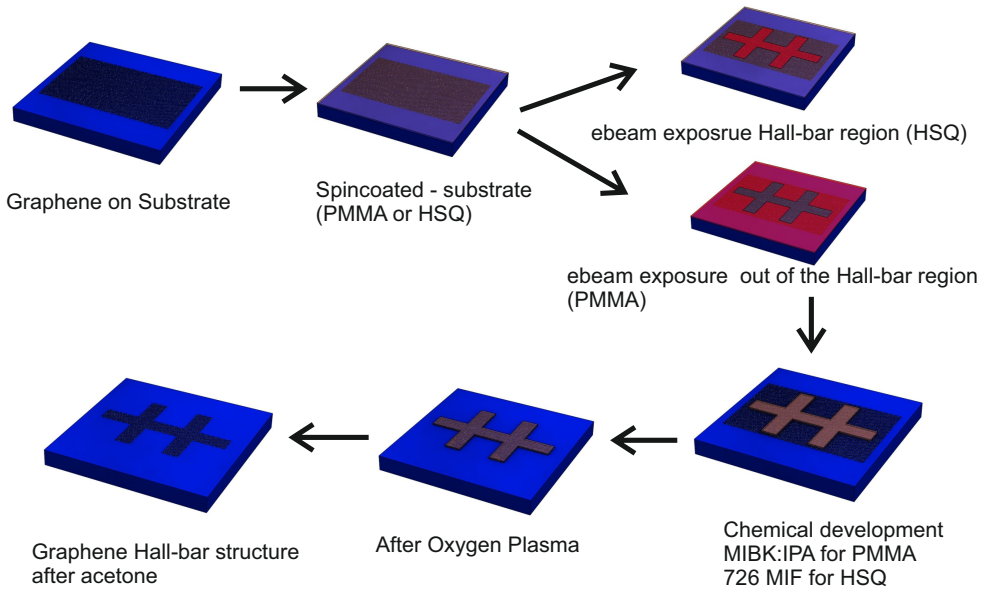

Figure 4.8: Shaping the graphene into Hall-bar: process flow for Positive (PMMA) and negative (HSQ) tone resist.

4.6 Pre-testing and Substrate etching

After completing the contact fabrication, device resistance values through all the contacts are tested by DC probe station. For the devices which have a few k-Ohm resistance values are processed to the etching procedure for the suspension. Before starting the etching procedure, substrate has to be diced into small dimensions (less than 4mm x 4mm) to attach it easily into the chip carrier (LCC02034- 20 pin chip carrier from SPECTRUM Semiconductor material).

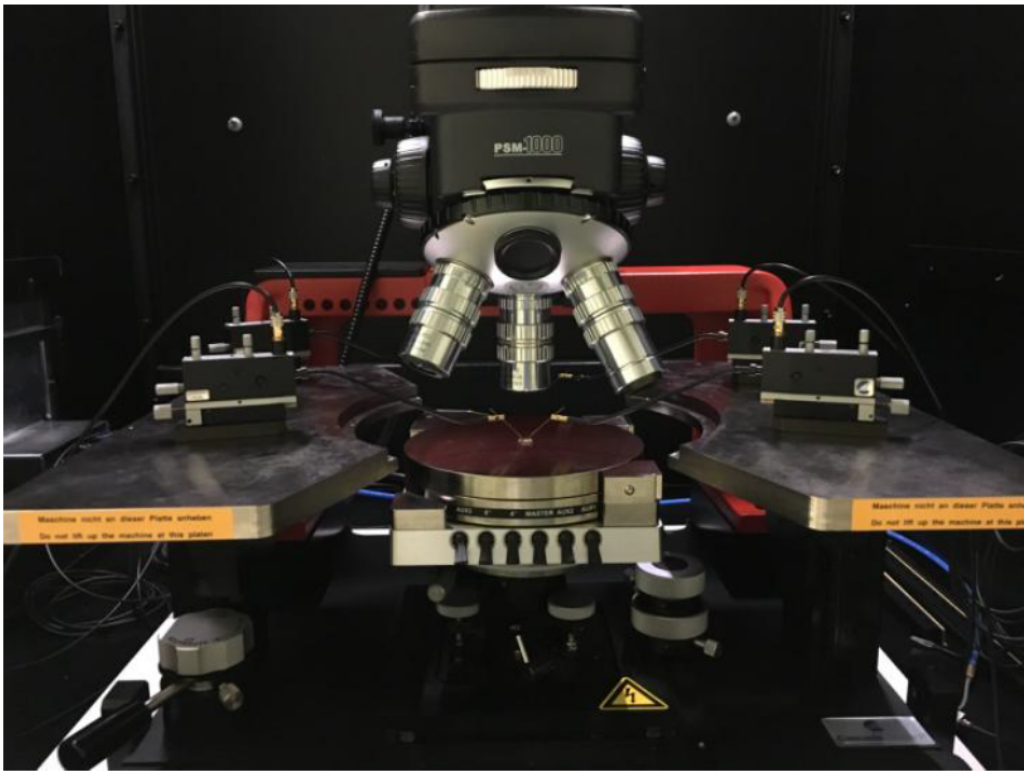

Figure 4.9: DC Probe station for pre-testing of the device resistance

7:1 Buffered oxide etcher (BOE) is used to etch the SiO_x underneath the graphene for the suspension. This etchant offers a very controlled etching process with an etch rate of $\approx 1.2\ nm/s$. We usually etch $\approx 200\ nm$ of SiO_x by immersing the sample into the BOE during 2.45 minutes. Remained oxide ($\approx 85 - 90\ nm$) is intentionally left in order to eliminate any short-circuits through the contacts where the graphite pieces short to Si layer which serves as a back gate. Sample is taken away from the BOE, then put into the distilled water to stop the etching process after 2.45 minutes. Then, we put the sample into hot isopropanol (IPA) which has a lower surface tension for 5 minutes. Finally sample is taken away from the IPA, dried with gently blown very low pressure nitrogen gas flow. Figure 4.10 shows free standing graphene sheets between the metal contacts.

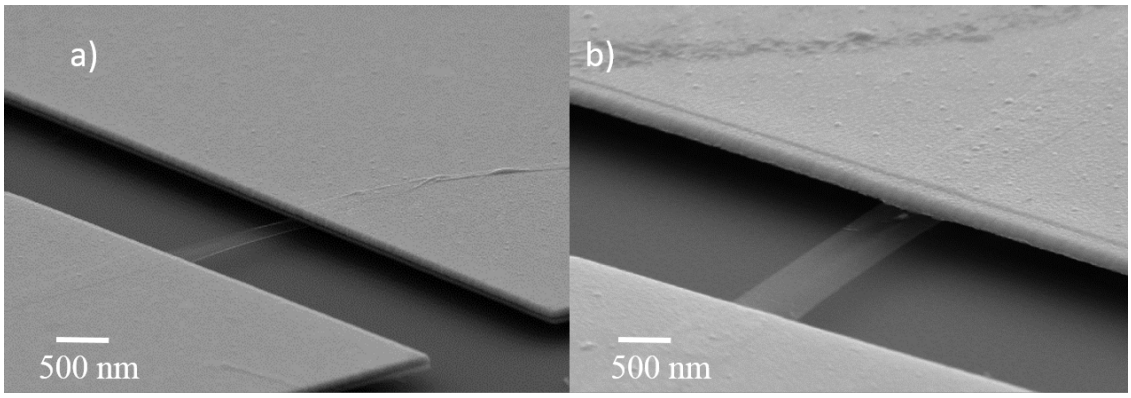

Figure 4.10: Scanning electron microscope pictures of 2-Terminal Suspended graphenes. SEM Images in a) and b) were taken at 70 degree tilted angle.

Certainly, reducing the fabrication steps during the device fabrication can play a critical role on the electrical and mechanical performances of the fabricated device. Obtaining a clean device after the fabrication is a challenging issue, especially for the graphene. One can clearly see the cleanliness level between the graphene sheets after different fabrication steps. In Fig. 4.10, the devices were fabricated by Vistec EBPG500+ just one ebeam step whereas in Fig. 4.11 device fabrication was completed with extra optical lithography steps which were explained in the 4.5 section. Residues on the suspended graphene sheet are mainly due to the remained optical resist residues which is harder to clean compared to the ebeam resist residues.

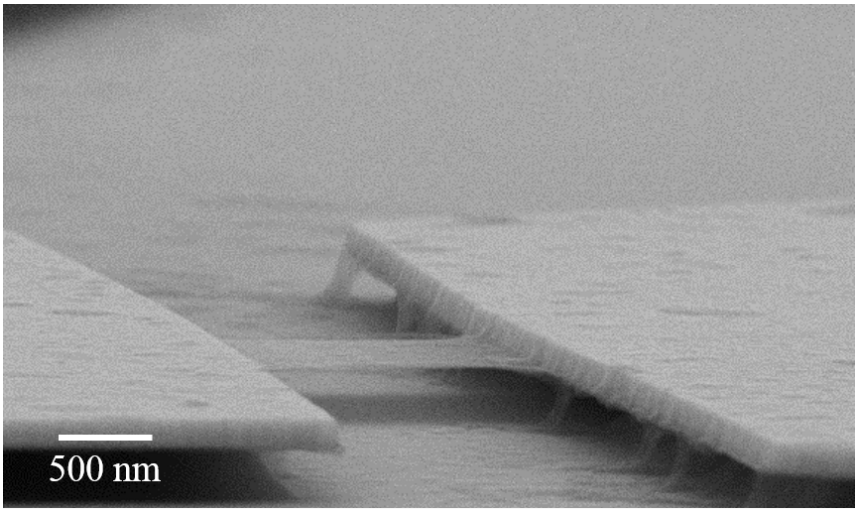

Figure 4.11: SEM picture of 2- Terminal Suspended graphene fabricated before Vistec EBPG5000+. Image was taken at 80 degree titled angle.

4.7 Alternative Drying; Critical Point Dryer

It is almost impossible to suspend long graphene sheets due to the surface tension during the drying process [Fig. 4.12]. An alternative way of drying can be the use of the critical point dryer (CPD) which provides a continuity of state where there is no apparent difference between the liquid and gas state of a medium. Therefore, the surface tension between this interface reduces to zero.

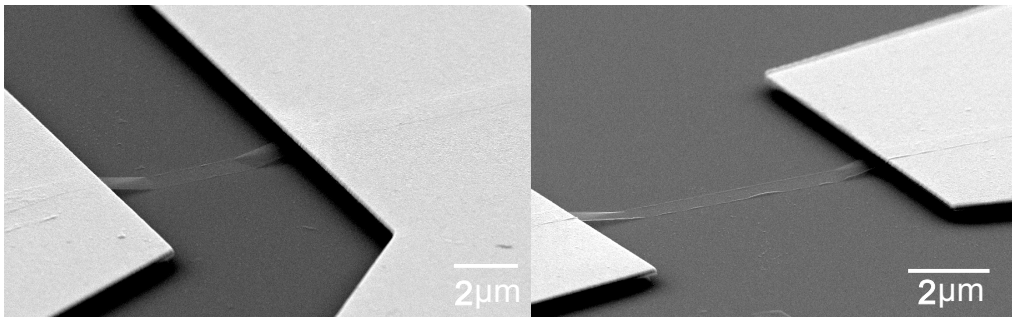

Figure 4.12: SEM images of the 2- Terminal Collapsed graphene sheets.

Quorum K850 CPD has been used for drying procedure [Fig. 4.13]. Drying operation can be given in the following steps;

- After the substrate etching, sample is transferred into a special specimen basket filled with isopropyl alcohol (IPA).
- Chamber is filled with IPA (15-20 ml) and the sample is transferred to chamber.
- All the screws are tightened up and the chambers is started cooling from the high-pressure CO_2 cylinder via cool valves.
- When the chamber reaches around $\approx\ 2°C$ temperature, liquid CO_2 transfer is started. Chemical is purged throughout the exhaust line while the fresh liquid CO_2 transfer continues. This is repeated until the solvent exchange is completed.
- Chamber is filled with liquid CO_2 up to desired level that is marked on the glass side of the chamber for the final time for critical point drying. Heater is switched on, then the temperature reaches $31°C$ and 1072 psi in 45 minutes. Critical point is achieved with this temperature and pressure values. One can observe from the glass side of the chamber that the liquid level drops and eventually goes away completely.

- System can be de-pressurized through the exhaust valve or bleed valve, 100psi/minute in 10 minutes.

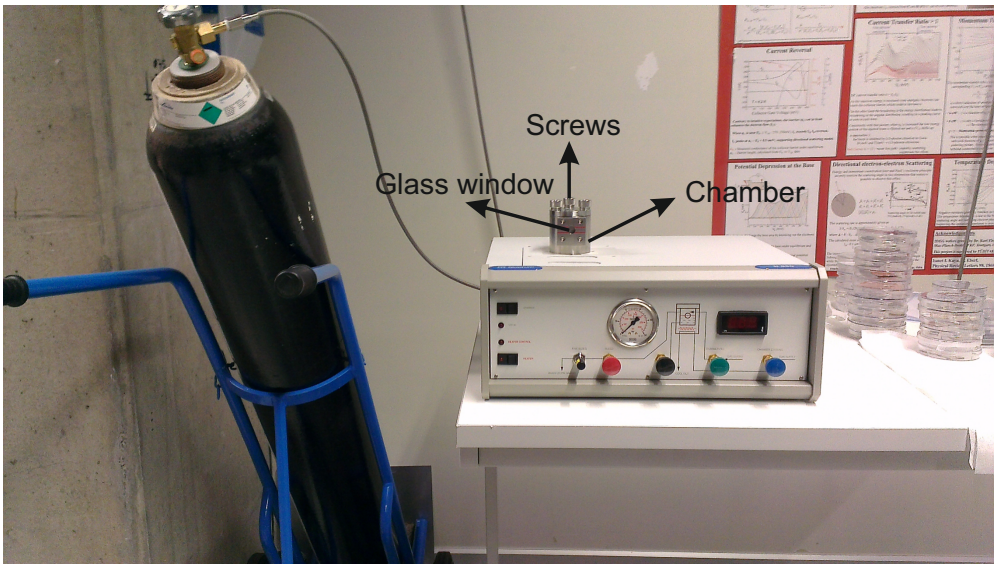

Figure 4.13: High pressure liquid CO_2 cylinder and Quorom K850 Critical Point Dryer (CPD).

However, we have realized some macroscopic contaminations which can be seen even under optical microscope after the drying. Similar observations as heavy sample contamination, have been reported after using the critical point dryer[28]. We have decided not to use CPD and limited the device dimensions as $L \leq 1$, $W > L$.

4.8 Bonding

Wire bonding is one of the methods of making the wire-connections between the ohmic contacts and the chip carrier pins. Before bonding, the substrate which was already diced by diamond scriber into small dimensions is glued to the bottom gold plate(Silicon back-gate connection will be made on this background gold plate region) region of the chip-carrier by electrically conductive silver epoxy (EPO-TEK H20E; mixture of Part A and Part B in same amount of mass ratio). The electrical connections between the ohmic contacts of the device and the gold-pins of the chip carrier were achieved by using the ball bonding mode of the Kulicke & Soffa wire bonder with $25\ \mu m$ thick gold wires.

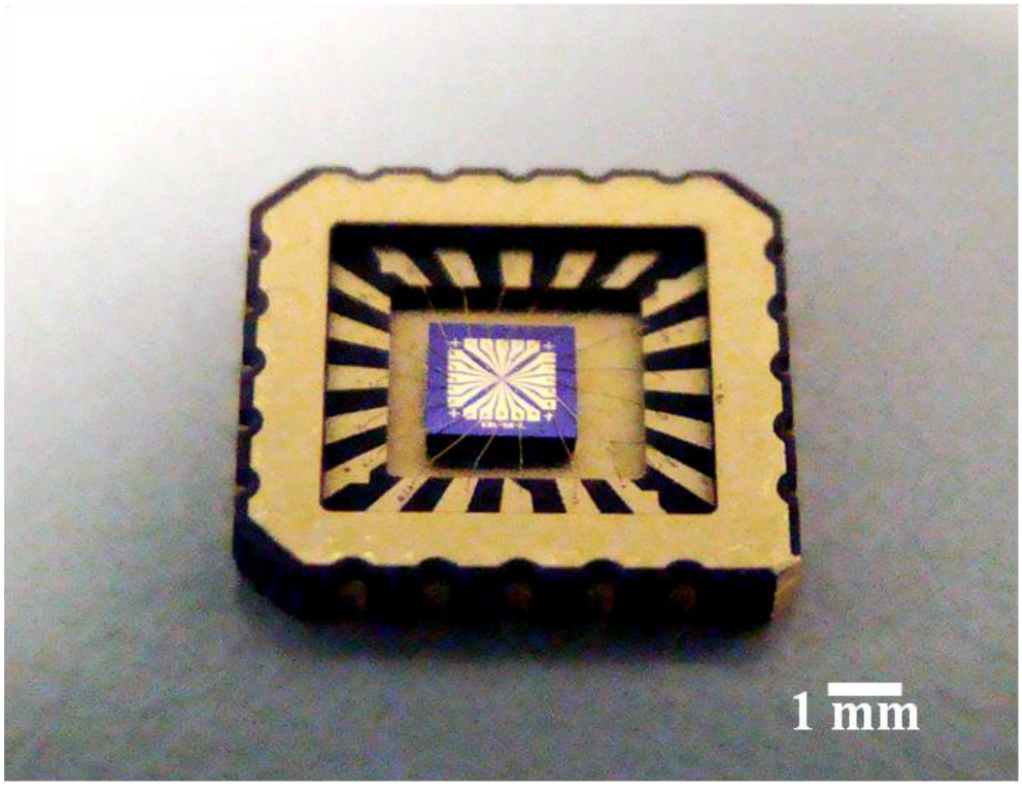

Figure 4.14: Image of the LCC02034 - 20 pin chip carrier (from SPECTRUM Semiconductor material) wire bonded to a graphene device chip.

4.9 Cryostats & Electrical characterization setups

In this thesis, low temperature experiments were performed in the Oxford instruments He^4 wet cryostat (1.4-200 Kelvin; 14 Tesla) [Fig. 4.15(a)], and Triton 400 He^3/He^4 closed cycle dilution refrigerator (0.01-30 Kelvin; 12 Tesla) [Fig. 4.15(b)]. The standard cool-down procedure of the wet cryostat from room temperature to liquid helium temperature is described in Appendix. B.

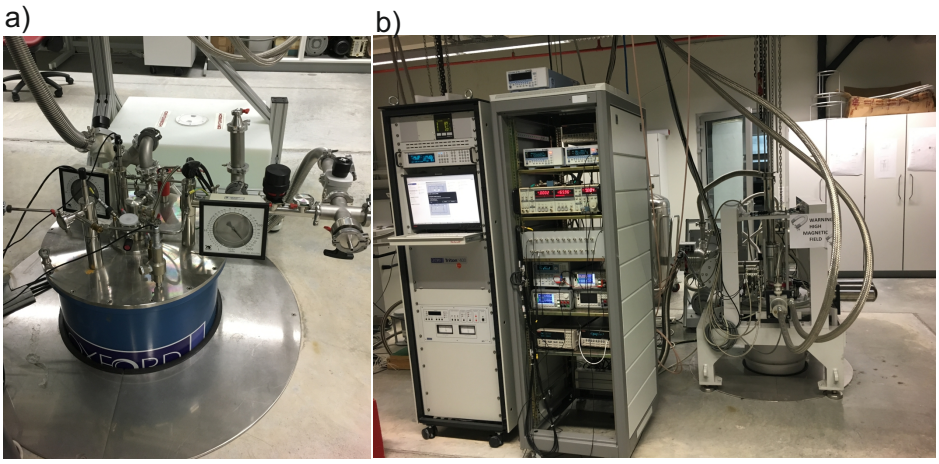

Figure 4.15: Cryostats for the low temperature measurements; a) Oxford 1.4 K He^4 wet cryostat b) Oxford Triton 400 He^3/He^4 dilution refrigerator with the electrical measurement set up in the rack at the left side

For transport measurements, measurement setup is given for a Hall bar configuration and 2- terminal suspended graphene in Fig. 4.16. Following electrical units were used for the electrical characterization;

- SRS SR830 Lock-in amplifier
- Agilent B2912A Source Measure Unit (SMU)
- Agilent B2962A Power Source Unit
- Yokogawa GS200 DC Source
- Yokogowa GS610 SMU
- Keithley 22182A Nanovoltmeter
- Keithley 7001 Switch-box

Keithley switch box is used to measure all the pairs of the contacts through the Nanovoltmeter (DC), subsequently. Back gate voltage is appliied with DC source unit though

the SiO_2 dielectric to tune the charge carrier density in graphene. For AC measurements, an AC current at low frequencies (17 Hz) is applied to the sample using standard lock-in techniques. All measurements are automated and controlled by Labview software of National Instruments.

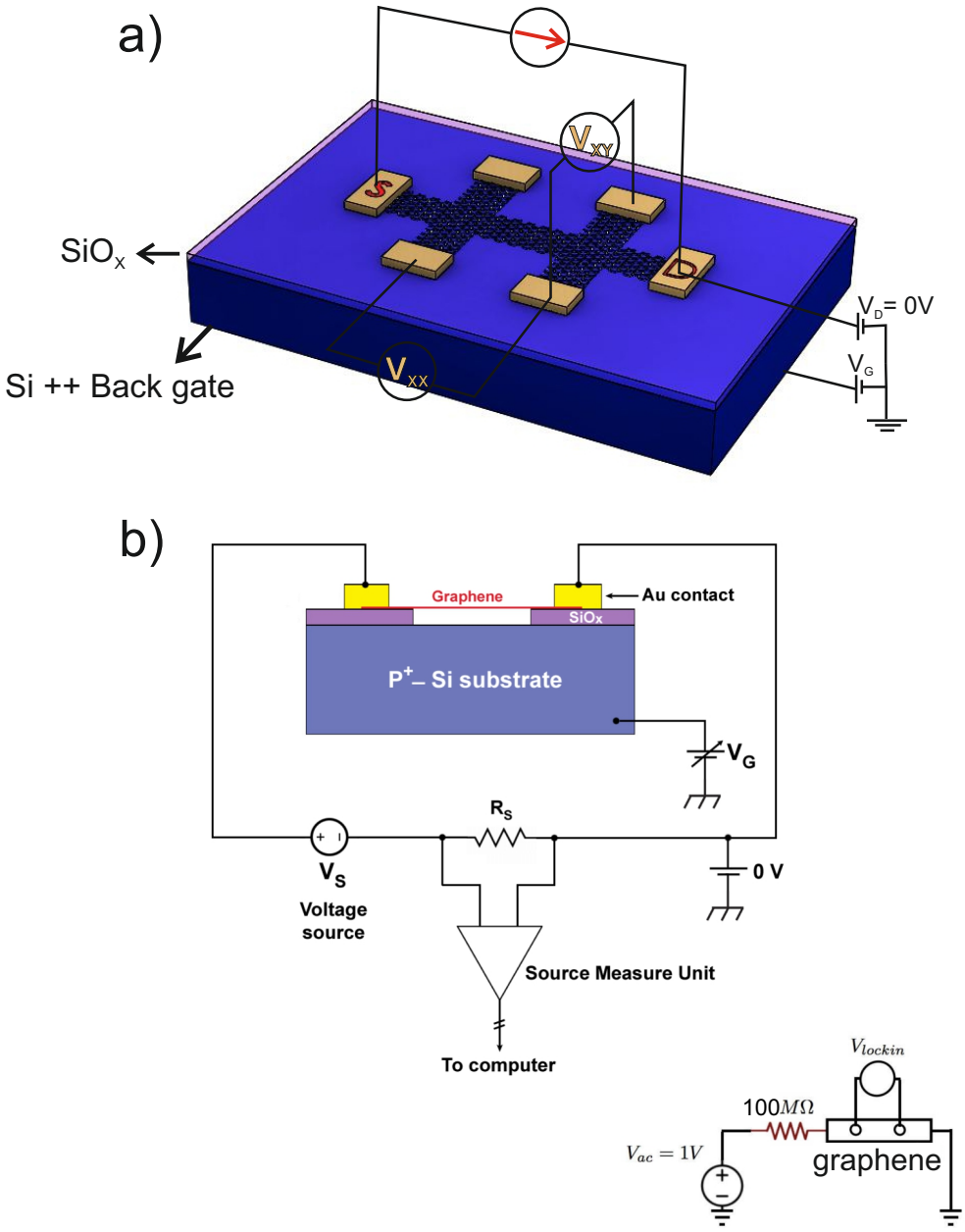

Figure 4.16: Measurement setup; a) Schematic for the magneto-transport measurements in a graphene Hall bar. In the presence of a perpendicular magnetic filed, a constant current is applied between the contacts (S-D). The voltage drop through the longitudinal and transverse contacts V_{xx} and V_{xy} are measured, respectively. b) Schematic for the 2 terminal suspended graphene measurement set up with the lock-in technique. The lock-in excitation at 1 V AC thorough the 100 $M\Omega$ resistor gives a current excitation of 100 nA.

Chapter 5

LOCAL BREAKDOWN OF THE QUANTUM HALL EFFECT IN NARROW SINGLE LAYER GRAPHENE HALL DEVICES

In this work[1], we investigated the breakdown phenomenon in narrow monolayer graphene Hall bar samples addressing the role of the charge inhomogeneity. In the narrow graphene samples of about one micrometer width, the charge inhomogeneity is quite prominent and strongly affects the nondissipative transport in the quantum Hall regime. Microscopic inhomogeneity of the dopant density in 2DEG causes potential fluctuations in the sample interior. These microscopic inhomogeneities lead to slight spatial variations in the carrier density and the current distribution in large area samples. Although they are small, these fluctuations are enhanced near the breakdown of the quantum Hall effect in 2DEG and result in large spatial variation of the critical currents [13]. The charge impurities have been shown to significantly enhance the inter-LL scattering rates and reduce the critical current in monolayer and bilayer graphene samples [15]. We observed that the quantization of the Hall resistance can retain at high current densities in the excess of 5 A/m even in the presence of a dissipative potential along the longitudinal probes.

[1]The results presented in this chapter are published in *Solid State Communications* ©2013 Elsevier B. V., Volume 160, April 2013, pp. 47–51. C. Yanık, I. I. Kaya[81]

5.1 Nonequilibrium Transport Results and Discussion

The graphene flake used in the experiments was exfoliated from a highly ordered pyrolytic graphite (HOPG), transferred on to a silicon substrate coated with $285\ nm$ of SiO_x and was verified to be monolayer by Raman spectroscopy. Electron beam lithography and oxygen plasma etching were used to define the Hall bar geometry with $w = 1\ \mu m$ width as shown in Fig. 5.1(a). The current leads were given a funnel shape to gradually reduce the effect of the hot spots at the injection corners. The graphene arms were extended outside the Hall bar to form the potential probes to prevent the electrode-induced doping of the graphene. This geometry also helps to minimize the interference of the metal leads with the current flow and provides a well defined bar width through the sample.

The contacts on the graphene were defined by electron beam lithography and Cr/Au (5/30 nm) evaporation. Immediately before the cool down for measurements, the sample was heat treated in 10^{-5} mbar vacuum by a combination of external heating up to $120\,^{\circ}\mathrm{C}$ and current heating by passing up to 1 mA dc current. The heat treatment cycles were carried out inside a built-in chamber on top of the cryostat allowing the sample transfer without breaking of the vacuum.

DC measurements were done within a temperature range of 1.4-300 K. The degenerately doped silicon substrate served as the back-gate to tune the density of carriers. After the heat treatment, the Dirac point was settled to +15 V which indicated that the graphene is p-type doped. The source of the persistent doping even after such an aggressive heat treatment is probably due to residues trapped between the graphene and the substrate or the impurities from the SiO_x substrate itself. We have experienced in several samples that the current annealing is quite delicate and may result in highly inhomogeneous graphene if done excessively for devices on the SiO_x.

The Hall mobility of the device was measured as 8300 $cm^2/V-s$ at $n = 5\times10^{11}\ cm^{-2}$ and the corresponding mean free path can be calculated from the Drude formula as;

$$l_{mfp} = \sigma h/(2e^2 k_F) \Longrightarrow l_{mfp} = 0.07\ \mu m \tag{5.1}$$

Since the mean free path and the size of the sample are comparable, there is an enhancement of the inhomogeneity over the Hall bar area. Fig. 5.1(b) shows the resistivity of the sample $\rho_{xx} = R_{xx}w/L$ as a function of the gate voltage measured between the two adjacent voltage probes (6-7 and 7-8) when current is passed between the leads 1-5. at $T = 1.4$ K. Both resistivity traces well coincide apart from the small fluctuations. These conductance fluctuations are repeatable and represents the varying effects of the random distribution of the scatterers on different potential probes. Inset in the Fig. 5.1(b) shows

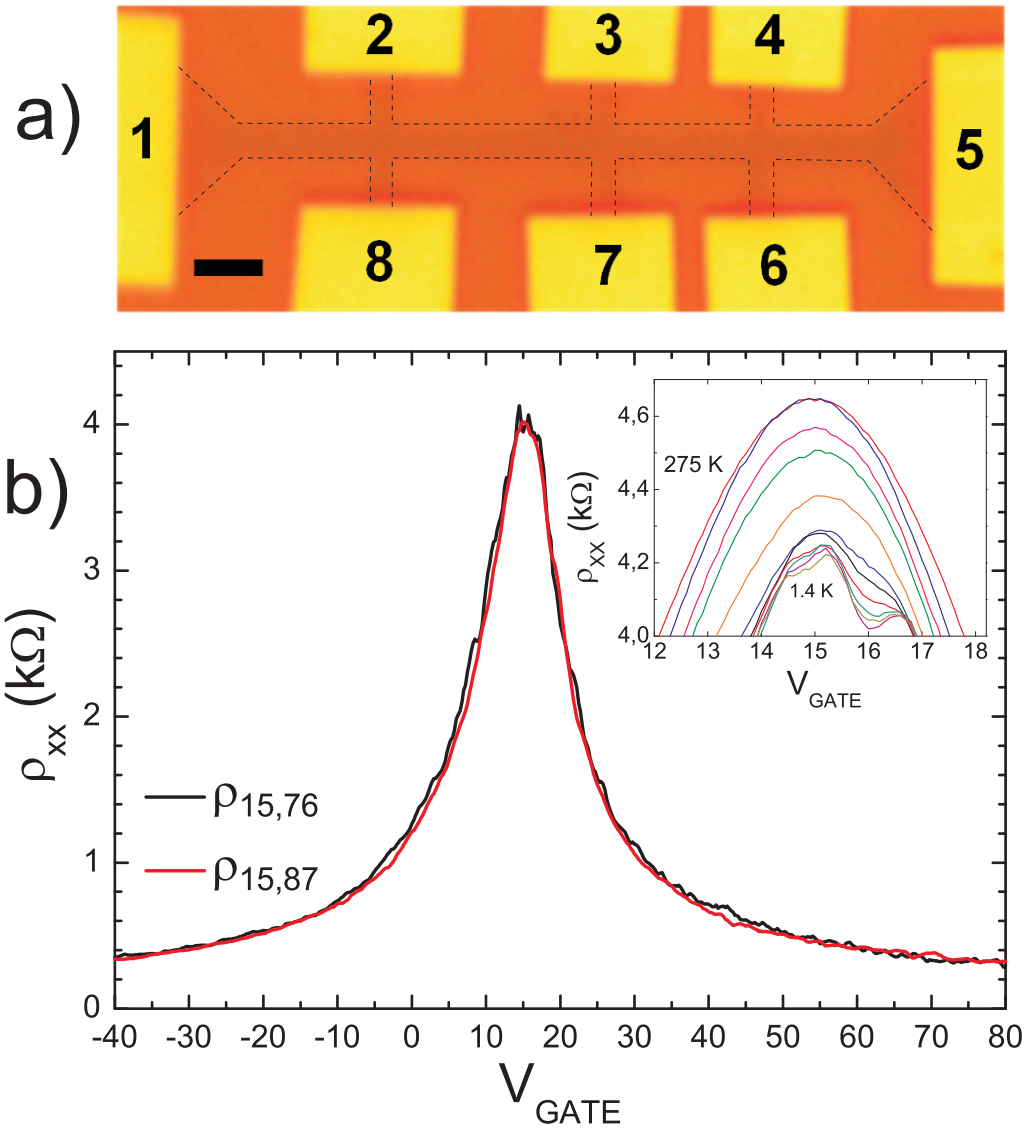

Figure 5.1: (a) The optical microscope image of the measured sample. Yellow pads are Cr/Au contacts defined by electron beam lithography. Current leads are marked as 1 and 5. During the measurements the electrons are injected from the lead 5. Dashed lines mark the borders of the graphene. Scale bar is 2 μm. (b) The longitudinal resistivity, ρ_{xx} versus the back gate voltage, V_{GATE} measured between the contacts 6-7 ($L = 5\ \mu m$) and 7-8 ($L = 7.5\ \mu m$) ($\rho_{15,76}$, $\rho_{15,87}$) at 1.4 K. Inset shows $\rho_{15,76}$ versus V_{GATE} for temperatures 275, 175, 135, 115, 77, 47, 37, 27, 10, 5 and 1.4 K.

the emergence of the conductance fluctuations as the temperature is lowered below 77 K.

In Fig. 5.2 the Hall conductance, σ_{xy} and the longitudinal resistivity, ρ_{xx} are plotted as a function of the gate voltage at $B = 11$ T and $T = 1.4$ K. The quantum Hall plateaus in σ_{xy} corresponding to filling factors of $\nu = \pm 2, \pm 6$ and ± 10 are well defined and confirms that the sample is made of monolayer graphene. $\nu = \pm 2$ plateaus are the sharpest and the breakdown of the quantum Hall effect for the sample was studied in detail around these filling factors.

The breakdown of the quantum Hall effect is characterized simultaneously for the

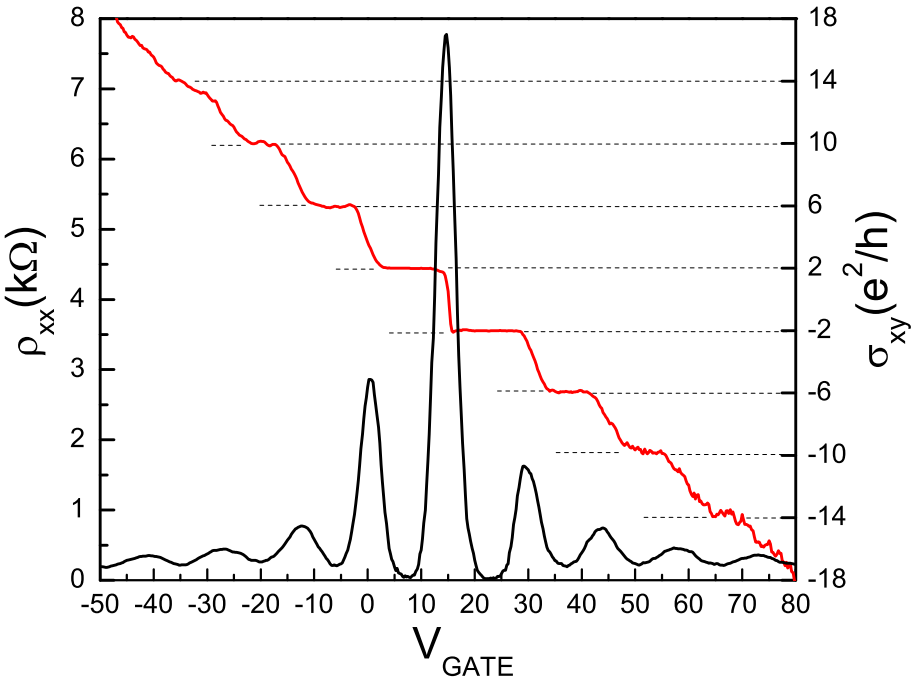

Figure 5.2: Longitudinal resistivity $\rho_{15,76}$ (black curve) and the Hall conductance $\sigma_{15,46}$ (red curve) as a function of the gate voltage at $B = 11\ T$ and $T = 1.4\ K$ with a bias current $I = 0.7\ \mu A$. Hall plateaus at the fillings factors $\nu = \pm 2, \pm 6, \pm 10$ indicate that the sample is monolayer graphene.

longitudinal resistance between the probes 6-7, 7-8 and the Hall resistance between the probes 4-6. The rest of the voltage probes, had too high contact resistances to perform accurate measurements. Fig. 5.3(a) displays the evolution of the longitudinal resistance minima, ρ_{xx} and the Hall resistance plateaus, R_{xy} around the filling factor $\nu = +2$ when the current is increased from 0.6 μA to 20 μA corresponding to maximum current density $j_x = I/w = 20\ A/m$ for the $w = 1\ \mu m$ sample width. The results of the same kind of measurements for $\nu = -2$ are shown in Fig. 5.3(b). In these graphs, the Hall resistance and the longitudinal resistance were measured between the contacts 4-6 and 6-7 respectively with a shared contact. Therefore, R_{xy} and ρ_{xx} measurements probe the adjacent zones of the Hall bar; nevertheless not exactly the same as it is always the case for any measurement with the Hall bar geometry. We observe quite different breakdown behavior for the Hall and longitudinal resistances for this specific sample and attribute it to local variations throughout the sample due to microscopic inhomogeneity of the unintentionally doped graphene.

We observe that both ρ_{xx} and R_{xy} follow a normal breakdown behavior. As the current increases, longitudinal resistance minima increase from their nearly nondissipative value

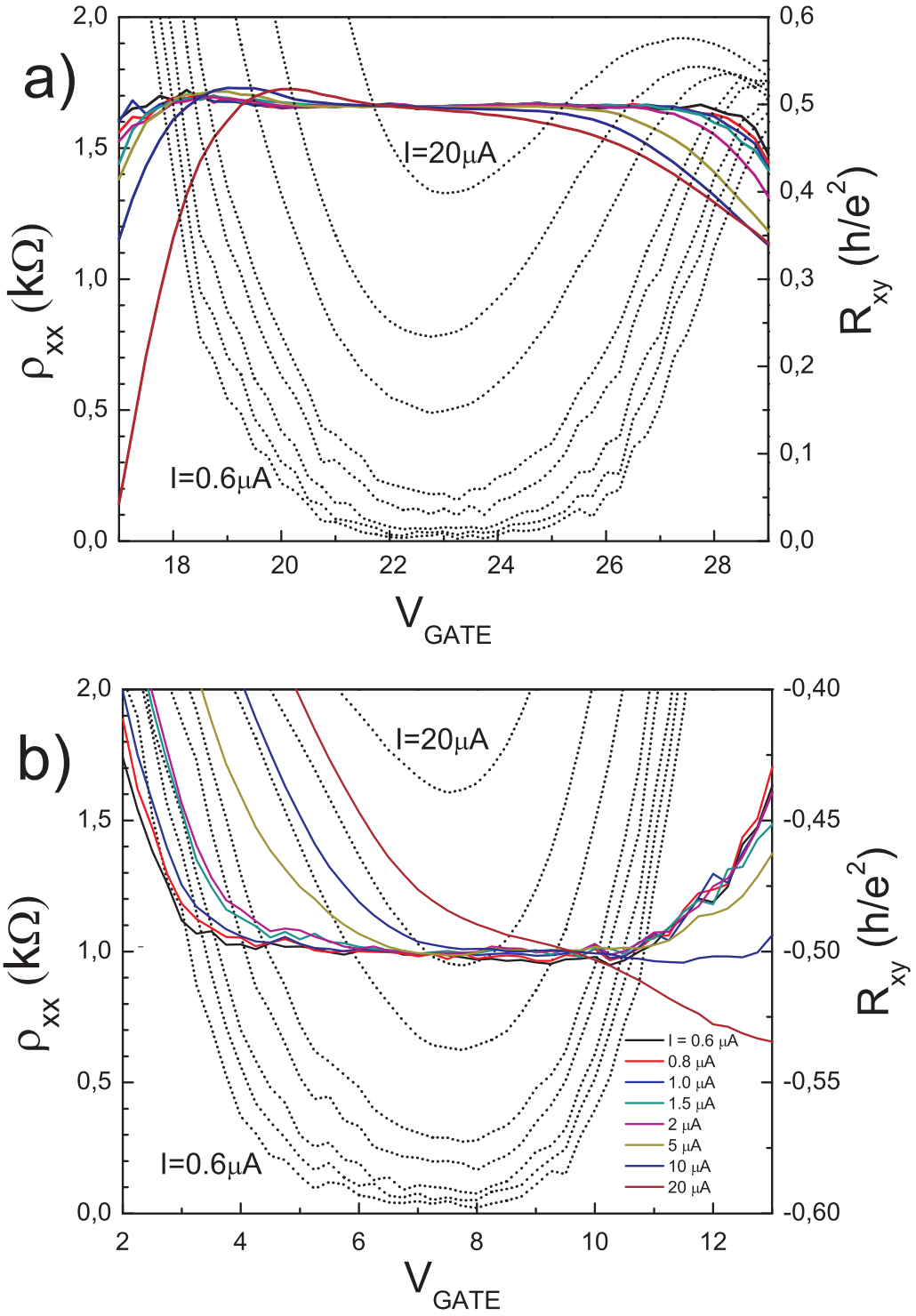

Figure 5.3: The evolution of the longitudinal resistivity $\rho_{15,76}$ (black dots) and the Hall resistance $R_{15,46}$ (colored solid lines) around the filling factors (a) $\nu = 2$ and (b) $\nu = -2$ as a function of the gate voltage, V_{GATE} at $B = 11\ T$, $T = 1.4\ K$ with currents I = 0.6, 0.8, 1, 1.5, 2, 5, 10, 20 (μA) as labeled in (b).

and reaches $\rho_{xx} > 1\ k\Omega$ at $I = 20\ \mu A$ while the flat plateaus of the R_{xy} gradually shrink and eventually vanish. The conductance fluctuations are still visible in these ρ_{xx} and R_{xy} plots for relatively low currents, but with the increasing current they diminish and

disappear rather erratically. Some of the fluctuations shift and may even enhance with the increased current. This behavior is attributed to the shifting of the electron-hole puddles in the graphene with the expansion of local dissipative regions [98]. A close examination of the graphs indicates that the emergence of the breakdown clearly occurs at quite different current values for ρ_{xx} and R_{xy}. While R_{xy} maintains its flatness up to 5-10 μA range, ρ_{xx} nearly reaches 1 $k\Omega$ for such high currents and already exceeds 100 Ω around 1 μA.

Fig. 5.4(a) displays the longitudinal resistivity between the voltage probes 6-7 and 7-8 as a function of the current density, j_x for the low current range and the full range of up to 20 A/m. Unlike the familiar breakdown behavior in 2DEG samples, the longitudinal resistivity makes a rather gradual transition into the dissipative regime with the increased current. This behavior is similar to those can be seen in the previous publications with exfoliated graphene [15, 63, 64]. Although there is a nonlinear increase of resistivity below 1 A/m, an abrupt jump is missing in all of the traces. Therefore, it is quite difficult to define the critical current for the breakdown. Here we set a threshold resistivity of 40 Ω to determine the critical current values, I_c for $\rho_{15,76}$ as 0.75 A/m ($\nu = +2$) and 0.50 A/m ($\nu = -2$); for $\rho_{15,87}$ as 0.50 A/m ($\nu = +2$) and 0.65 A/m ($\nu = -2$). A relatively high resistivity is chosen as the threshold resistance to reduce the error from the conductance fluctuations in this rather narrow sample. We attribute the large variation in the critical current between the probes as well as between the filling factors to the inhomogeneity of the sample. High local electric fields due to the applied gate voltages in the sample should effect the charge distribution. For the filling factors $\nu = +2$ and $\nu = -2$ the gate voltage has the values $V_{GATE} = 23\ V$ and $V_{GATE} = 7.5\ V$. Due to the presence of the electron-hole puddles in graphene, gate potential may alter the charge distribution through the sample and cause the spatial variation of the critical current.

Fig. 5.4(b) displays the semilog plot of the σ_{xx} versus $1/j_x$. An exponential variation of σ_{xx} between $j_x = 0.6 - 5\ A/m$ can be seen in this graph for all the traces although their current range and slope slightly vary. For lower currents longitudinal conductivity saturates to its minimum value originating from the conductance fluctuations. For the high current densities ($j_x > 5\ A/m$) σ_{xx} increases faster with the current. Inset in Fig. 5.4(b) shows the fit of the measured conductance to a phenomenological function;

$$\sigma_{xx} = \sigma_0 exp[-\Delta E_{eff}/eV_H] \tag{5.2}$$

between $j_x = 1 - 2\ A/m$.

Here σ_0 is a prefactor which is found to be $0.12 \pm 0.03\ e^2/h$ and $\Delta E_{eff} = 30 \pm 3\ meV$ is the effective energy gap for the activation of the carriers, for the filling factors $\nu = \pm 2$ and both of the sample regions measured.

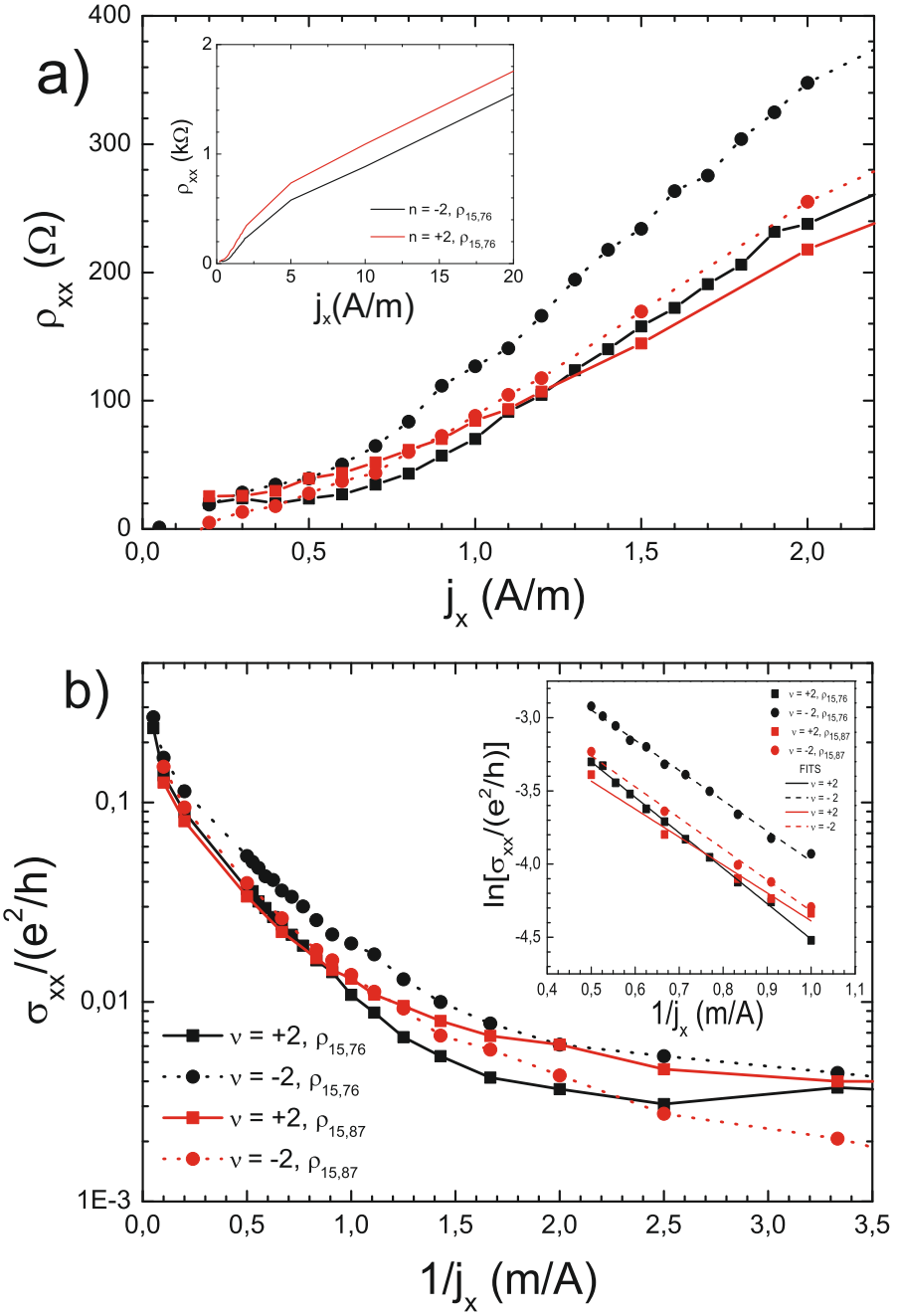

Figure 5.4: (a) ρ_{xx} versus current density, j_x for $\nu = \pm 2$ and between the contacts 6-7 and 7-8. Longitudinal resistivity makes a rather gradual transition into dissipative regime with the increased current. Critical currents at filling factors $\nu = \pm 2$ between the probes (6-7),(7-8) at $B = 11\ T, T = 1.4\ K$. Inset shows $\rho_{15,76}$ vs j_x for $\nu = \pm 2$ with the full range of currents. (b) σ_{xx} versus $1/j_x$ in semilog scale. Inset shows fittings at filling factors $\nu = \pm 2$ between the probes (6-7),(7-8) at $B = 11\ T, T = 1.4\ K$ for the region $j_x = 1to2\ A/m$.

The exponential dependence of conductivity on ΔE_{eff} for this regime is due to quasi-elastic inter-Landau level scattering (QUILLS) assisted by large local electric field. This

behavior is also observed by Guignard *et al.* and analyzed within the variable range hopping (VRH) model via the dependence of the energy gap on the filling factor [15]. The measured effective gap ΔE_{eff} is very close to the experimentally observed thermally activated gap value [99]. The difference between $\hbar\omega_c/2 = 65\ meV$ and $\Delta E_{eff} = 30\ meV$ can be attributed to potential fluctuations due to charge inhomogeneities. Spatially resolved measurements has demonstrated the existence of the potential fluctuations with the intrinsic disorder length scale of $\approx 30\ nm$ in a monolayer graphene related to electron hole puddles [98]. It has been measured by temperature dependent magneto transport measurements that the potential fluctuations due to the electron hole puddles around the charge neutrality point in graphene is about $20\ meV$[100]. Although QUILLS model predicts larger breakdown currents than almost all the breakdown experiments due to the relatively large separation between the LL's, the impurity potential fluctuations in effect reduces the spatial separation between the LL'ss and enhances the tunneling between the localized puddles of compressible and incompressible states. Within this picture the breakdown behavior of a sample strongly depends on the distribution and the strength of the potential fluctuations which was also proposed by Sing *et al.* [63].

The breakdown behavior becomes more erratic in small samples as the one investigated in this work. Here we argue that the ρ_{xx} measurements and R_{xy} measurements should be very different in the narrow sample. In our experiments ρ_{xx} measurements probe the partial areas of the sample ($L_{7-8} \times w = 7.5 \times 1\ \mu m^2$ and $L_{6-7} \times w = 5 \times 1\ \mu m^2$). However the Hall measurements probe a much smaller sample area ($w_p \times w = 1 \times 0.5\ \mu m^2$) where ω_p and ω are the width of the voltage probe and the width of the sample respectively. We indeed observe a difference in the breakdown behavior of the longitudinal and Hall resistances.

The deviation of the Hall resistance from its quantized value is known to be related to the longitudinal resistance in 2DEG samples. This relation has been experimentally analyzed by temperature driven and current driven dissipative regimes. An empirical relation;

$$\Delta R_{xy} = -s\rho_{xx} \tag{5.3}$$

has been observed in numerous experiments and various mechanisms have been proposed to explain the behavior [101–105]. At high temperatures quadratic dependence, $\Delta R_{xy} \propto \rho_{xx}^2$ was also seen [105]. The observed value of the s in the linear relation varies but typically is in the order of unity. One of the proposed mechanisms is the geometrical effect, i.e. the mixing of the longitudinal resistivity to Hall resistance when the current

density and the Hall field are not orthogonal under dissipative conditions,

$$\Delta R_{xy} = -(w_p/w)\rho_{xx}[103]. \tag{5.4}$$

In the temperature driven dissipative quantum Hall regime, Cage *et al.* experimentally verified the linear relationship over four orders of magnitude change in resistivity and determined the s values to vary in the range of 0.015-0.5 depending on the sample and the configuration of the probes [102]. The behavior can be understood by the thermal activation of electrons to higher Landau levels. The deviation of R_{xy} versus ρ_{xx} was also analyzed when the 2DEG is driven into dissipative regime by increasing the current and again a linear relation is observed. In the current driven dissipation the value of the s and its variation with the filling factor verified the role of the variable range hopping mechanism for the activation of the carriers [105].

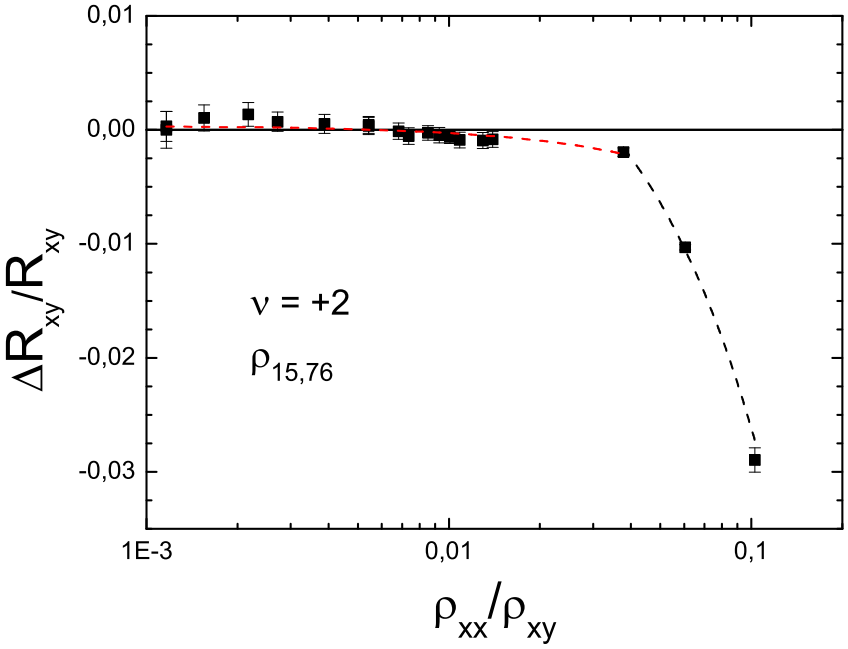

Figure 5.5: Relative deviation of the Hall resistance, $\Delta R_{xy}/R_{xy}$ versus the normalized longitudinal resistivity, $\Delta\rho_{xx}^{min}/R_{xy}$ at the filling factor $\nu = 2$. Semilog scale is used to clearly display all data points. Red and black lines are the linear fits to two range of data corresponding to $j_x \leq 5\ A/m$ and $5\ A/m\ \leq\ j_x \leq 20$ A/m respectively.

We analyzed the current driven deviation of the quantized Hall resistance, ΔR_{xy} as a function of the longitudinal ρ_{xx} for the filling factor $\nu = 2$ as shown in Fig. 5.5. We observe two regimes in this plot, for the current densities up to 5A/m the deviation follows a linear behavior with a slope, $s = 0.066 \pm 0.008$. For $j_x = 5 - 20\ A/m$ however the deviation in the Hall resistance shows an abrupt increase and the slope jumps to $s = 0.40$.

The small value of s up to $j_x = 5\ A/m$ is due to the weak dependence of R_{xy} on the increased current compared to ρ_{xx}. Above $j_x = 5A/m$, ΔR_{xy} suddenly starts to increase with the current. This is consistent with the qualitative observation of the different onset of the breakdown in the ρ_{xx} and R_{xy} plots in Fig. 5.3.

High critical current for the Hall resistance compared to the lower critical breakdown current of longitudinal resistance is caused by the narrow, small and more homogeneous region across the Hall probes 4-6. In this particular small region of the sample to Hall plateaus remain flat well up to high fields possibly due to slower variation of the potential fluctuations. On the other hand, longitudinal resistance measurements probe wider regions along which contains impurity induced potential fluctuations leading to smaller breakdown currents. Especially, when the length scale of inhomogeneity becomes comparable with the sample width, inhomogeneity size effect leads to variation in the range and distribution of the localized dissipative regions throughout the sample interior. This leads to variation of the breakdown current throughout the sample area. Such inhomogeneity effects in the breakdown of the quantum Hall effect were also observed in narrow GaAs 2DEG samples [106].

5.1.1 Collapse of quantized Hall resistance

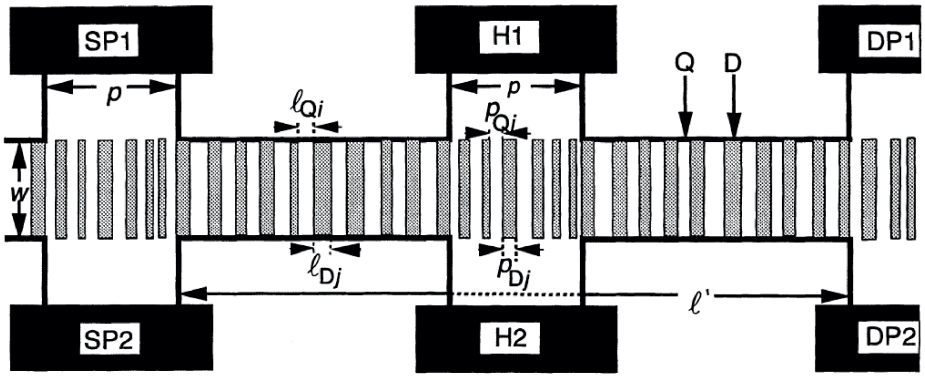

Figure 5.6: Schematic one-dimensional super-lattice (periodic or aperiodic) structure in a quantized Hall bar. Open area indicate ideal quantum Hall resistances Q and shaded stripes indicate dissipative quasi-quantum Hall resistances D [7].

A similar phenomenon was observed by Kawaji *et al.* in a GaAs 2DEG samples with $35\mu m$ width, indicating "a phase separation between the quantum Hall resistance state and the dissipative quasi-quantum Hall resistance state" [7]. The Hall resistance remained

precisely quantised even when the longitudinal resistance was increasing exponentially with the current. Then a *collapse*, a steep change in the quantized resistance occurred while longitudinal resistance kept its gradual increase. They explained the results using a phenomenological model which assumes that the Hall bar consists of alternating phases of ideal quantum Hall and dissipative quasi-quantum Hall states along the bar [Fig. 5.6]. Collapse of quantized Hall resistance occurs when the quantum Hall phase disappears near the voltage probes, hence it is a different phenomenon than breakdown.

5.1.2 Conclusions

We observed that in a narrow monolayer graphene Hall bar sample the critical current for the breakdown of the quantum Hall effect varies between 0.50 and 0.75 A/m depending on the probe set and the filling factor. The breakdown emerges as a gradual increase in the longitudinal resistivity rather than an abrupt jump and its behavior strongly depends on the location and the gate potential. The Hall resistance also displays a different behavior with the increasing current. Its deviation with current remains very small until an abrupt increase around $j_x = 5\ A/m$. The exponential dependence of the longitudinal resistivity on $1/j_x$ is attributed to impurity mediated inter-Landau level tunnelling of carriers. Charge induced inhomogeneity is critical for the breakdown of the quantum Hall effect, especially when the length scale of the fluctuations becomes comparable with the sample size in graphene devices. We interpret that the physical mechanism underlying the occurrence of local breakdown is the highly inhomogeneous distribution of impurity induced potential fluctuations in the sample.

Chapter 6

CHARACTERIZATION AND QUANTUM TRANSPORT IN SUSPENDED GRAPHENE DEVICES

One of the major drawbacks of graphene devices is its vulnerability to the environmental effects. Even, the molecular level contaminants or the substrates that graphene resides on can dramatically modify its electronic properties. In this thesis, in order to be able to probe the electronic properties of ultra clean graphene, suspended graphene devices were fabricated and electrically characterized at temperatures ranging from room temperature (RT) to 20 mK, in the presence of magnetic fields up to 12 Tesla. Various techniques have been developed to fabricate suspended graphene devices and treated them to reach ultra-high cleanliness. These lead us to produce devices with charge mobility values in excess of $10^6\ cm^2/V-s$. We observed that in these devices, the minimum conductivity around the Dirac point can exceed the theoretically predicted value of $4e^2/\pi h$. In such monolayer graphene devices, quantum Hall filling factors $\nu = 0, \pm 1$ can also emerge in the magneto-transport measurements in addition to the expected $2(2n+1)$ plateaus. The presence of these plateaus in these ultra high quality suspended samples indicates the lifting of the valley and/or spin degeneracy in these devices.

6.1 Cleaning the suspended graphene

In order to set the graphene free from disorders and impurities, besides the chemical cleaning treatments, there also exists some cleaning techniques in the literature such as annealing the graphene around $200°C$ in the $H_2 - Ar$ environment[107] or the current induced annealing of graphene which can help to reach ultra clean devices[30]. Since $H_2 - Ar$ annealing in a cryostat environment requires a separate system to proceed performing the cleaning, it is very challenging and costly. However, current annealing in a vacuum environment is more convenient to utilize and provides more effective cleaning on the suspended samples. This technique may not provide promising results for the

graphene sheets on substrates due to the residues trapped on the interface between the graphene and the substrate, or the impurities from the SiO_x substrate itself. We have performed the $H_2 - Ar$ cleaning procedure on the suspended graphene samples, however, we experienced that it does not give a remarkable effect in terms of the electronic measurements compared to the current annealing technique. The cleaning procedure can be given in these steps briefly;
Cleaning procedure in the $H_2 - Ar$ environment;

- Dry pump is started and waited to reach to vacuum levels down to $1 \times 10^{-2}\ mBar$ inside the quartz furnace.
- A forming gas ($1:9 - H_2 : Ar$) is sent through the furnace with a 300 sccm flow rate and waited for the pressure stabilization around 2 mBar. When it is stabilized, heating procedure can be started.
- Temperature is ramped from room temperature (RT) to $200°C$ in 1 hour.
- Sample stays at $200°C$ 1 hour.
- Temperature is ramped from $200°C$ to $340°C$ in 1 hour.
- Sample stays at $340°C$ 2 hours.
- Finally, temperature is ramped down to RT in 2 hours.

Fabrication procedure of the suspended samples is as follows in the steps which were already explained in the Device Fabrication chapter in detail. Briefly;

Suspended graphene devices are fabricated by mechanical exfoliation of natural graphite transferred on to a p doped Si substrate covered by 285 nm of SiO_x. Single-layer graphene flakes are determined based on their contrast under the optical microscope, then confirmed by Raman spectroscopy. Electron beam lithography is employed to pattern the electrical contacts made from Cr/Au (3/100 nm) followed by a lift-off in acetone. Suspension is achieved by dipping the SiO_x in Buffered Oxide etch (BOE) to remove $\approx$ 200 nm SiO_x. The remaining oxide is allowed to avoid any shorts between the leads and Si layer. Device is transferred from BOE to DI water then dipped into IPA and dried by nitrogen gas (N2) gently.

In the current annealing technique, huge amount of current density ($\approx 1\ mA/1\mu m$) is passed through the device which leads to the heating of graphene up to temperatures around $600°C$ and helps to evaporate the dirt on the sample in the vacuum environment. In Fig. 6.2 resistances R as a function of applied gate voltage V_G before and after current

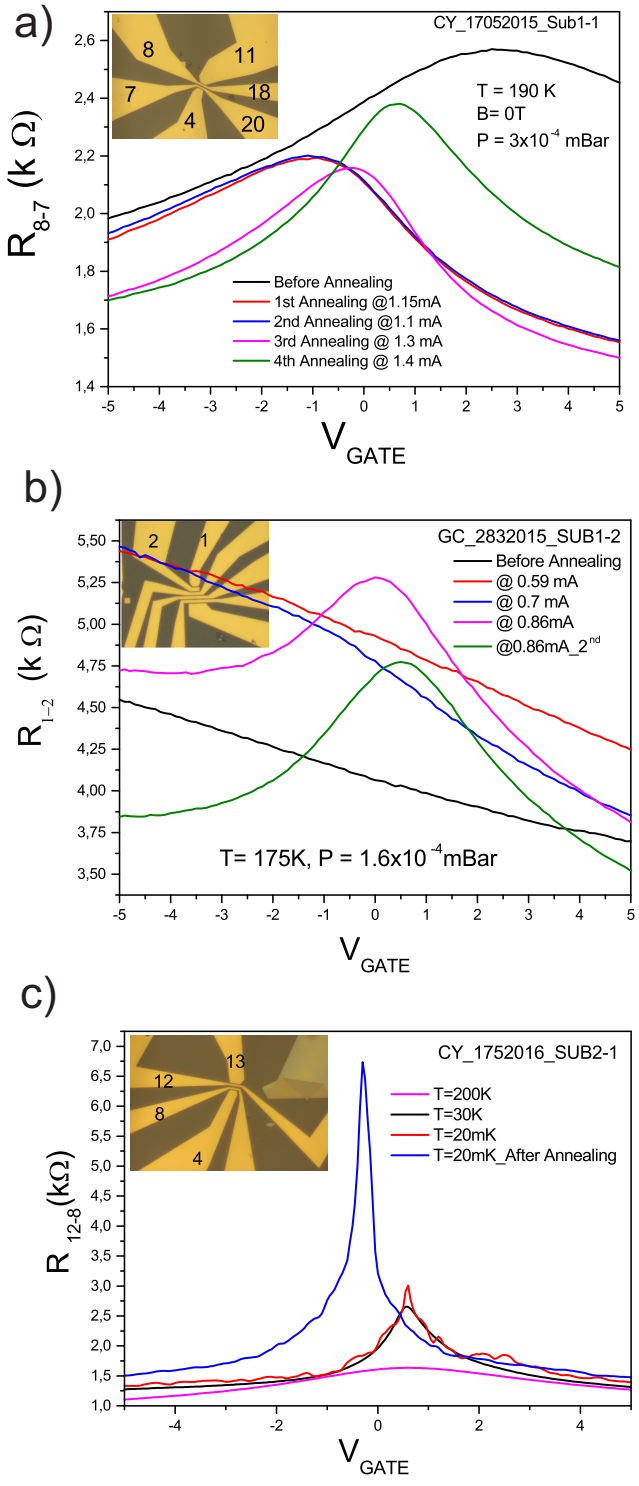

Figure 6.1: Resistance vs Gate potential values after performing current annealing on the suspended graphene devices. Insets show the optical microscope picture of the devices with labeled contact numbers wire-bonded to the pins of the chip-carrier. Measurements were carried out with the labeled contacts (subscription indicates Source- Drain).

annealing are given for some of the suspended graphene samples in various pressure and temperature conditions.

In Fig.6.2(a), the resistance behaviors of the suspended part of the sample (CY-17052015-SUB1-1, width:2.5 μm, Length: 1.75 μm, Probes between 8-7) as a function of applied gate potential are shown after performing 4 current annealing steps at zero magnetic field and at 190 K temperature in the vacuum environment at a pressure value of $3 \times 10^{-4}\ mBar$. Black line is the gate sweep before annealing, which does not exhibit a pronounced shape of the Dirac point around the zero gate potential. One can clearly see that a significant difference has been achieved on the resistance curve after 4^{th} annealing step by passing $1.4\ mA$ DC current through the graphene sheet. We show another R vs V_G sweep curve of the suspended device (GC-2832015-SUB1-2, width:2 μm, Length: 1 μm, Probes between 2-1) at 175 K in Fig. 6.2(b). Initially, Dirac peak is not observable in the range of applied gate potential(-5 V to +5 V), which indicates that the graphene is heavily doped (black curve). It has not been achieved to obtain a remarkable shape on the resistance for the currents ramped up to $I_S = 0.86\ mA$. Then the Dirac peak is obtained at $V_G = 0.5\ V$ after 2^{nd} annealing with the current, $I_S = 0.86\ mA$. Fig. 6.2(c) shows the resistance values as a function of gate potential at different temperature values before and after current annealing for another suspended graphene samples (CY-1752016-S2-1,width:2 μm, Length: 1 μm, Probes between 12-8). Blue curve shows the resistance curve at base temperature (15 mK) in vacuum environment ($P \approx 1 \times 10^{-6}\ mBar$) after applying just one annealing on the sample with current $I_S = 1.1\ mA$. We have experienced that the current annealing provides much better results in the high vacuum and low temperature environments.

6.2 Multi-source current annealing through the split design contacts

2-terminal suspended graphene devices can be successfully cleaned by current annealing technique. However, it is almost impossible to achieve a uniform temperature gradient on the suspended samples with the multi-terminal designs, since the side probes act like a heat sink. It has been showed that annealing one part of the sample makes dirty the other part and vice versa [108]. We consider a split contact design where we pass high currents ($40\ mA$) through the metal contacts, while passing an optimal current density through the graphene for cleaning. Eventually, we expect the dirt near the contacts to evaporate with an effective heating, and therefore, to obtain higher quality samples. We

design the contacts as narrow as possible in order to ramp to temperatures with relatively less current densities. On the other hand, narrowing the contacts too much may lead to the collapse of the graphene during the etching due to the mechanical instability. Our experiences have shown that gold contacts designed with widths around $1\ \mu m$ are ideal for an effective annealing, where it can reach to desired temperatures with the probe currents around $30 - 40\ mA$.

6.2.1 Automatic Annealing Software

We control the source-measurement units and the data acquisition during the annealing procedure by LabVIEW software of National Instruments. The software first increases the current on the contacts by an amount set on the program, and at the same time, keeps a constant low current passing through the graphene to monitor the changes in the device behavior during the annealing process.

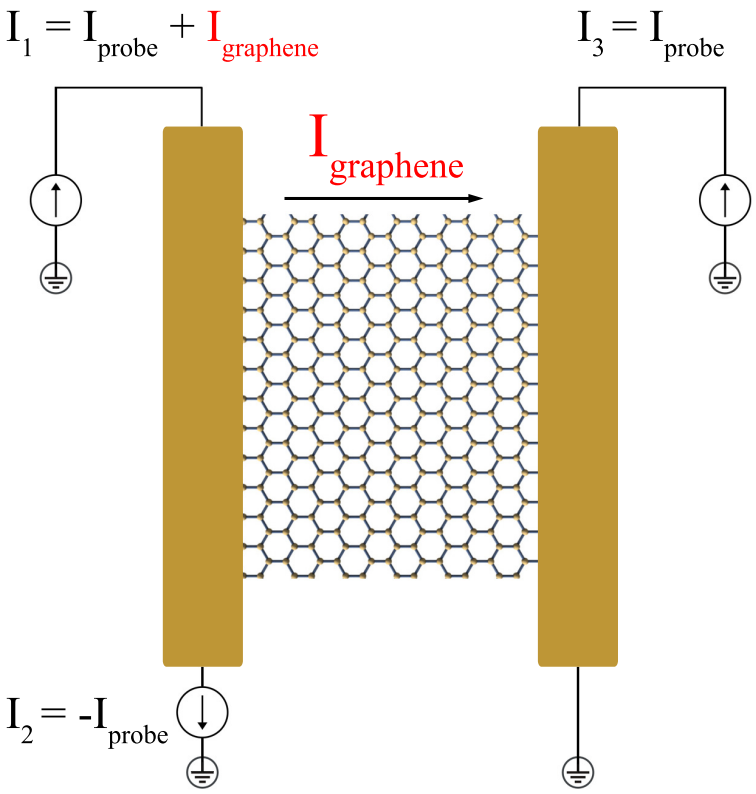

Figure 6.2: Schematic of the electrical set-up for multi-source current annealing through the split contacts and graphene.

2-terminal graphene device fabricated with split contacts are electrically connected to source-measure units as is shown in Fig. 6.2, where I_{probe} is the intended current to

be passed through the metal contacts in order to heat up the probes, and $I_{graphene}$ stands for the current passing through the graphene during the heating up process of the probes. Through $I_{graphene}$, which is usually a low current, we are able to probe the changes happening to the graphene while we reach high temperatures in probes. Annealing software flows as follows:

1. *Setting metal probe currents*
    - First set the upper left probe to $I_{graphene}$.
    - Then increase I_1, and decrease I_2 by ΔI increments/decrements (Therefore, only $I_{graphene}$ amount of current will pass through graphene).
    - Increase I_3 by by ΔI increments. Since the other end of I_3 is the drain, it does not need to apply any current to the other end.
    - Measure the voltages and currents of each probe and print.
    - Repeat this procedure until $I_1 - I_{graphene} = -I_2 = I_{probe}$
2. *Graphene annealing (User controls)*
    - User is free to set the current $I_1 - I_{probe} = I_{graphene}$ and probe the resistance changes in graphene.
    - Continuously measure the voltages and currents of each probe and print.
    - User will press "Stop Annealing" when the user observes a significant jump/drop in the graphene resistance.
3. *Return back to the zero current state of the probes*
    - First, bring $I_1 - I_{probe} = I_{graphene}$ to I_{probe} by ΔI decrements.
    - Then decrease I_1, and increase I_2 by ΔI decrements/increments.
4. *Gate sweep (User controls)*
    - User is free to sweep the gate voltage in order to confirm if any affirmative change has happened.
    - If device needs further annealing, user can repeat the whole procedure.

6.2.2 Effective annealing with the split contacts

A set of annealing experiments were organized in order to investigate whether the probe annealing makes any change on the transport properties or not. All the annealing steps have been performed individually in the suspended graphene sample (CY-792015-SUB1-2)[Fig. 6.3(a)].

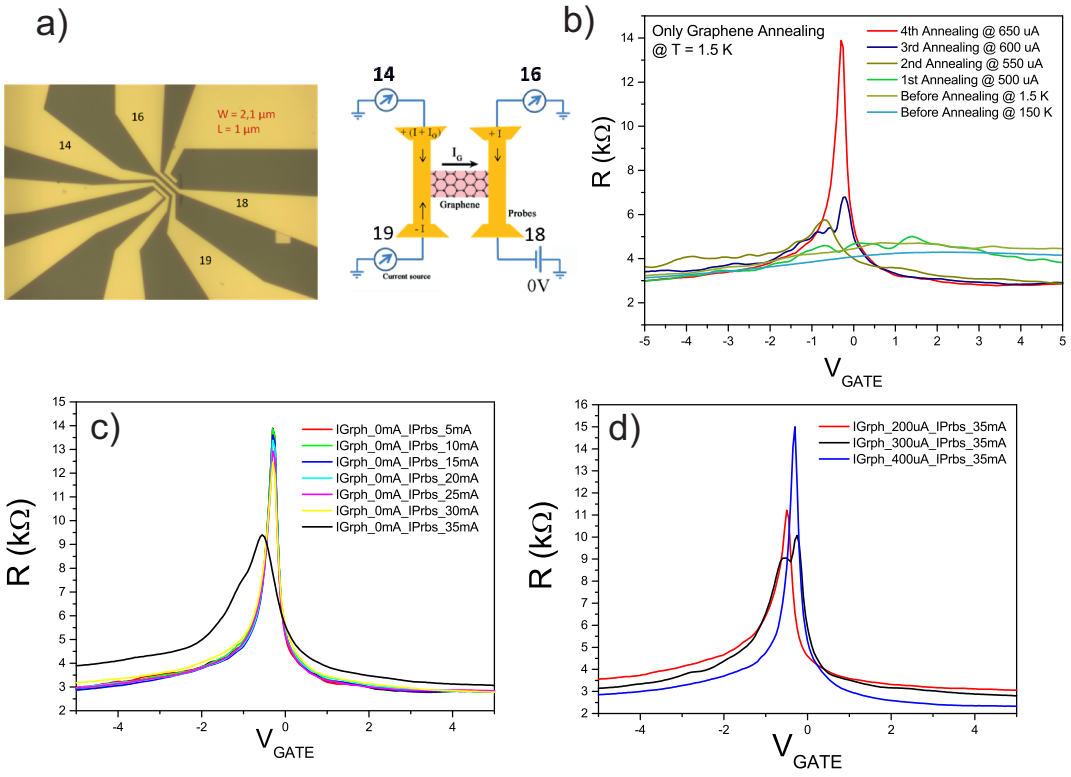

Figure 6.3: Multi-source current annealing through the split contacts of the suspended sample (CY-792015-SUB1-2). a) Optical image of the device, contact configuration and the measurement schematic. R vs V_G results for only the graphene annealing $I_{probes} = 0$, probe annealing $I_G = 0$, graphene and probe annealing at 1.5K, b), c), d), respectively.

We first started with just passing current through the graphene (Probes between 14-16) and caught the Dirac point on the resistance curve which is very close to the zero gate voltage after passing a DC current of $I_S = 650\ \mu A$ at 1.5 K [Fig. 6.3(b). Before the current annealing, one can see that the sample resistance had almost no response to the gate. After catching a desired shape on the resistance curve, we only heated the probes by passing huge amount of currents through the probes (14-19) and (16-18, 18 at 0V) step by step (From 5 mA to 35 mA) during 5 minutes. [Fig. 6.3(c).

We could not observe a significant change on the resistance curve by passing currents up to 30 mA. However, in the last ramp up to 35 mA, we observed a significant difference on the resistance curve (black), where resistance curve got broadened and the peak value almost dropped to half of it. We claim that the one highly possible reason for this can be the graphene was contaminated by the residues located near the contacts, which migrated into the center of the graphene region. After the observation of the probe annealing on the graphene, we decided to keep the same $35\ mA$ amount of current constant for the probes and pass the current I_G through the graphene simultaneously to be able to create an effective heating on the total graphene region which may lead to better cleaning of the graphene device. In Fig. 6.3(d), we show the results of the resistance curve as a function of applied gate potential after performing the annealing steps while the probes at $35\ mA$ and graphene currents at $I_G = 200\ \mu A\ (red), 300\ \mu A\ (black), 400\ \mu A\ (blue)$. One can see that a remarkable shape on the resistance curve has been obtained (better than Fig. 6.3(b)) with the $I_G = 400\ \mu A$ while the probes at $35\ mA$ indicating the effective annealing has been achieved. Although, we were able to obtain an ultra-clean graphene sample by this multi-source annealing technique, it definitely requires further imaging and/or surface characterization in order to prove the real influence of the effective cleaning on the samples.

6.3 Temperature dependence of the resistance

The temperature behavior of the resistance can be used to estimate the disorder level in the system. Clean samples show higher peak resistances which increases as the temperature is lowered and saturates when k_BT is smaller than the Fermi energy fluctuations;

$$k_BT \lesssim \hbar v_F \sqrt{\pi n}. \tag{6.1}$$

Non-suspended or dirty suspended samples (not annealed) have extrinsic sources of disorders which induce pronounced inhomogeneity in the carrier density around;

$$n \sim 10^{11}\ cm^{-2} \Rightarrow T = \hbar v_F \sqrt{\pi n}/k_B \sim 400\ K \tag{6.2}$$

which explains the weak dependency of the resistance peak on the temperature in the range of $0 - 300\ K$[109].

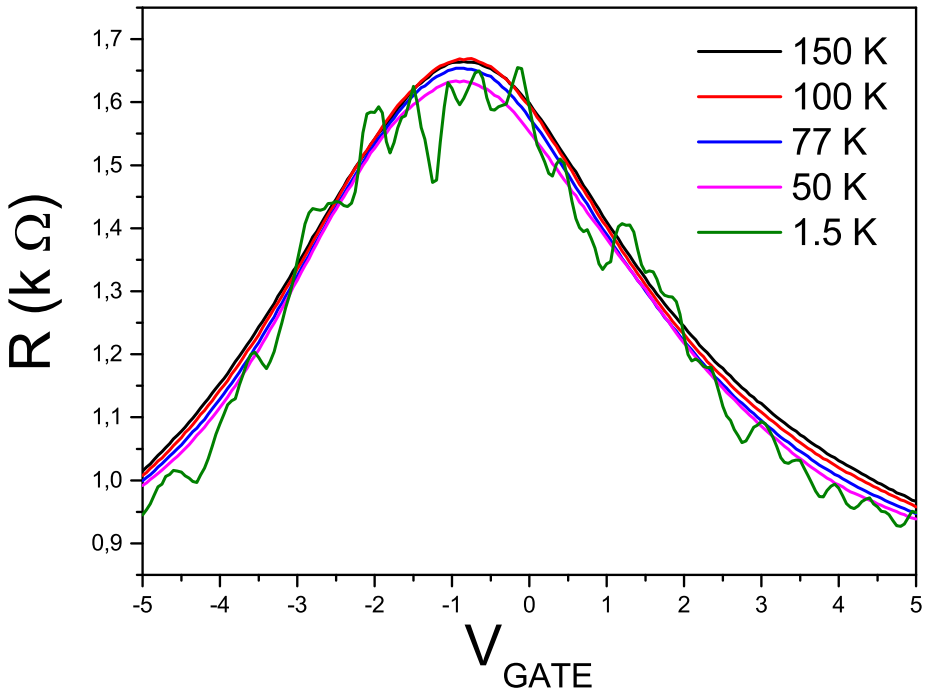

Figure 6.4: Temperature evolution of the resistance for not-annealed suspended graphene. As the temperatures gets lowered, sample does not exhibit any improvement in its resistance shape.

Fig. 6.4 shows the resistance as a function of gate voltage for a non-annealed suspended sample at the indicated temperatures at zero magnetic field. Here the resistance shape neither has an increment in its peak value nor the change in the full width at half maximum as the temperature decreases, only conductance fluctuations emerge at $1.4\ K$.

However, Fig. 6.5 shows the resistance curves of an current-annealed suspended sample (CY-17052015-SUB1-1) as a function of V_G in various temperatures (Surface Plot). It can be clearly seen that the resistance peak gets narrower, while the peak values increases as the temperature decreases. The full width at half maximum (FWHM) of the resistance peak is significantly lowered from $\Delta W_{Dirac} \equiv \Delta V_G = 3.6\ V$ at 200 K to $\Delta W_{Dirac} \equiv \Delta V_G = 0.4\ V$ at 1.4 K with an almost order of magnitude reduced corresponding fluctuations in the carrier density.

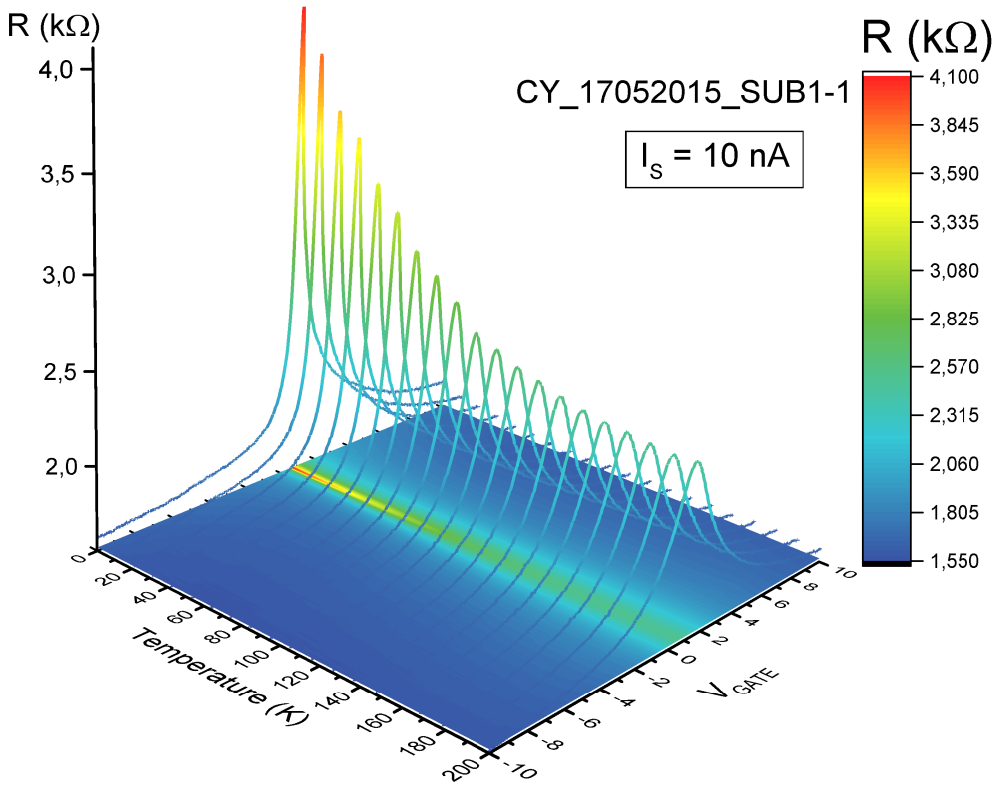

Figure 6.5: Temperature evolution of the resistance for the current-annealed suspended graphene. Surface color corresponds to resistance values as indicated in the scale bar.

6.4 Quantum Hall Measurements

6.4.1 Carrier Mobility

Quantitatively, the resistance R vs V_G can be fitted by the model[110, 111];

$$R_{tot} = R_C + \frac{L}{we\mu\sqrt{n_{res}^2 + n^2}}, \quad n(V_G) = \alpha(V_G - V_D) \tag{6.3}$$

Here the parameters correspond respectively to: R_C: Contact resistance, L: Length of the sample between the midpoints of the contacts, w: Width of the sample, e: electron charge, μ: Charge mobility, n_{res}: residual carrier concentration, n: Gate induced carrier concentration, α: Coupling factor between the carrier concentration and the applied gate voltage. The coupling parameter, α can be calculated by using the serial capacitor model as;

$$\frac{n}{V_g - V_{Dirac}} = \frac{C_g}{e}, \quad C_g = 1/\left(\frac{1}{\frac{\epsilon_0}{t_{vacuum}}} + \frac{1}{\frac{\epsilon_0\epsilon}{t_{oxide}}}\right) \tag{6.4}$$

where ϵ_0 and ϵ represent the permittivity of free space and SiO_x respectively.

This yields a coupling parameter of $\alpha \approx 2.5{\times}10^{10} cm^2V^{-1}$ for the suspended graphene where the suspension of the sheet above $\approx 200\ nm$ oxide layer, $t_{vacuum} \sim 200\ nm$ and the remained oxide, $t_{oxide} \sim 85\ nm$). Theoretically calculated result by considering this model is in good agreement with the one ($\alpha \sim 2.71 \times 10^{10}\ cm^2V^{-1}$) calculated experimentally from the quantum Hall measurements Fig. 6.6(a).

Fitting results on the resistance vs V_G curves of the suspended sample (CY-17052015-SUB1-1) are given separately for the electrons and holes in Fig. 6.6(b) and (c), respectively. Here the fittings were achieved by considering the length of the sample $L : 1.75\ \mu m$, width $L : 2.5\ \mu m$, Dirac point at $V_D = 0.45\ V$ as the constant parameters and the rests are free. The fittings yield very high mobilities for the holes and electrons, $\mu_h \approx 535000\ cm^{-2}V^{-1}s^{-1}$ and electrons $\mu_e \approx 359000\ cm^{-2}V^{-1}s^{-1}$, respectively. Moreover, individual fittings yield a residual concentration fluctuations in the carrier density of $\delta n_e \approx 5.5 \times 10^9\ cm^{-2}$ for the electrons, and $\delta n_h \approx 3 \times 10^9\ cm^{-2}$ for the holes. These residual carrier fluctuation values in the carrier density also agree with the one which is calculated from the FWHM value of the resistance peak, $\Delta W_{Dirac} \equiv \Delta V_G = 0.4\ V$ which corresponds to the the carrier fluctuations $\Delta n = \alpha \Delta V_G$ with $\alpha = 2.71 \times 10^{10}$. Considering the symmetric resistance curve, the inhomogeneity fluctuations in the carrier concentration gives $\delta n = 5 \times 10^9\ cm^{-2}$, which is very small for the graphene sheets on the substrates or dirty suspended samples ($\delta n \approx 10^{11}\ cm^{-2}$).

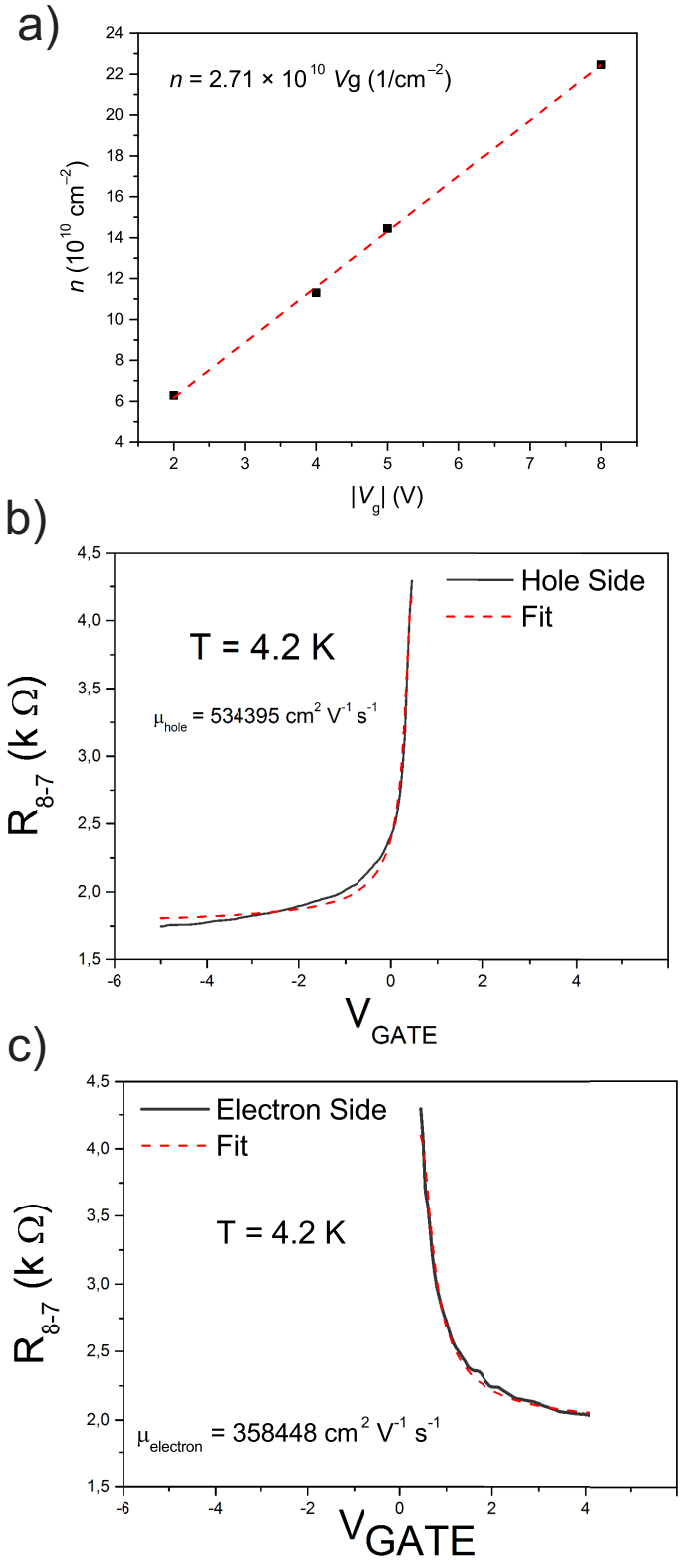

Figure 6.6: Carrier concentration and the mobility of the suspended graphene device (CY-17052015-SUB1-1). a) Carrier concentration is calculated from the quantum Hall measurements. b) Black line corresponds to hole branch of the resistance curve at 4.2 K. Hole mobility is extracted by fitting (red-dashed line) the curve by the given model in the tex. c) Resistance curve (black) and the fitting (red-dashed line) for the electron branch. Measurements were performed with an AC 10 nA source current.

6.4.2 Shubnikov-de Haas oscillations and the quantum mobility

In order to analyze the device quality from the onset of the Shubnikov-de Haas (SdH) oscillations, one can confirm the development of a minimum in $R(V_G)$ where SdH oscillations first appear as two maxima around the neutrality point (develop to first filling factors $\nu = \pm 2$) as the magnetic field increases above the certain magnetic field. This sets a lower mobility value of $\mu_Q \sim 1/B_q$ extracted from the magnetic field at which the carriers complete one cyclotron orbit without scattering using the equation;

$$\mu_Q B_q \equiv \omega_c \tau_q = 1 \tag{6.5}$$

where, B_q corresponds to the onset of SdH oscillations, ω_c is the cyclotron frequency, τ is the scattering time and μ_Q is called the quantum mobility[29]

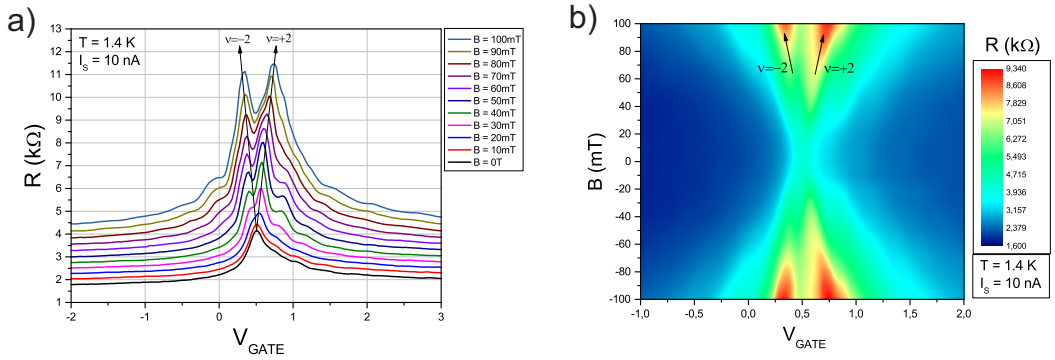

Figure 6.7: SdH oscillations and the quantum mobility a) $R(V_G)$ at the indicated magnetic fields. Arrows indicate the first quantization plateaus to be developed. b) 2D colour map of $R(V_G, B)$.

Fig. 6.7(a) shows the Resistance R as a function of applied gate potential V_G between the magnetic fields 0-100 mT at 1.4 K with an AC current source of $I_S = 10\ nA$, respectively. One can see the development of such a minimum in Fig. 6.7(a) where the minimum appears at $B_q = 30\ mT$ which sets a carrier mobility of around $\mu \approx 330000\ cm^{-2}V^{-1}s^{-1}$. This is in agreement with the mobility values extracted from transport mobility (fittings) in previous section. One should realize that the standard mobility calculations based on the Drude formula are valid for the charge transport takes place in the diffusive regime. In very high quality (high mobility) suspended samples, transport properties should be considered through the ballistic regime rather than the diffusive one. Thus, the mobility values calculated from the Drude formula may not give correct values for the mobility of the suspended samples, whereas quantum mobility as an qualitative estimate can give an

alternative way of quantifying graphene's quality. The development of the first $\nu = \pm 2$ filling factors is shown as a 2D surface plot in Fig. 6.7(b). Being able to observe such a development for the filling factors at these low magnetic fields confirms the high quality of the suspended devices. Observing these quantizations in the graphene samples on the SiO_x substrates or dirty suspended devices require higher magnetic fields due to the inhomogeneity fluctuations in the carrier concentration.

6.4.3 Quantizations by sweeping the gate potential

In the presence of a perpendicular magnetic field, the energy spectrum of two dimensional electron system splits into a fan of Landau levels. When the Fermi energy is tuned by changing the gate potential and lies between the Landau levels, system enters the integer quantum Hall regime, in which transport is governed by the edge states and overall conductance G is quantized as $G = \nu e^2/h$, where ν is the filling factor which takes integer values, e is the elementary charge, and h is the Planck's constant.

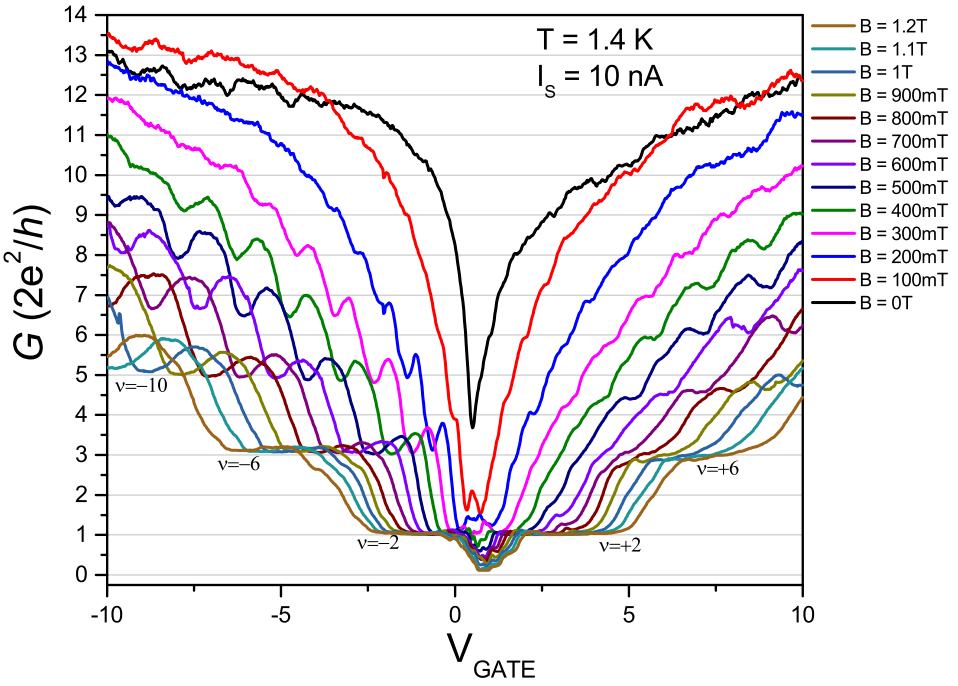

Figure 6.8: G vs V_G at indicated magnetic fields at 1.4K. Quantum Hall plateaus with conductance values $G = \nu e^2/h$ appear at the correct filling factors $\nu = \pm 2, \pm 6, \pm 10$ for the single layer graphene.

The sequence of the integer filling factors follows the values of $\nu = \pm 2, \pm 6, \pm 10, ...$ in graphene in the quantum Hall regime due to the fourfold spin and pseudo- spin (valley) degeneracy of the Landau levels which is explained in detail in Subsection. 2.3.3.

Conductance G of the suspended device (CY-17052015-SUB1-1) as a function of applied gate potential V_{GATE} is shown at 1.4 K by applying an AC source current $I_S = 10\ nA$ in the magnetic field range of 0 T - 1.2 T with 100 mT increments in Fig. 6.8. We start observing well developed plateaus in the conductance at $2e^2/h$, corresponding to the filling factors of $\nu \pm 2$ after 0.3T. A fully developed sequence of the filling factors at $\nu = \pm 2, \pm 6, \pm 10$ can be seen at relatively low magnetic fields at $B = 1\ T$. This also confirms that the sample is certainly single layer graphene. $1.1\ k\Omega$ contact resistance is determined by the deviation of the quantized plateaus from their correct quantization values. One should realize that we were able to see these sequences in the graphene Hall-bar samples on the SiO_x substrates at very magnetic field values around $B = 11\ T$.

6.4.4 Quantizations by sweeping the magnetic field

Although, the magneto-resistance measurements in two-terminal devices may not be as straightforward to interpret as simultaneously observable longitudinal and transversal resistance values in the multi-terminal devices, it is possible to observe the quantizations when the longitudinal contributions vanishes, $\rho_{xx} \approx 0$.

Fig. 6.9(a) shows the magneto-transport measurements of the suspended device at 1.4 K between 0-4 T magnetic field by applying two different gate voltages, $V_G = +3\ V$ and $V_G = -2\ V$, which correspond to the electron and hole regions, respectively. In the electron branch, besides the normal sequence of the filling factors for single layer graphene around 2.5 T, we observed a weak quantized plateau outside the normal sequence with $R = \frac{1}{\nu}\frac{h}{e^2}, \nu = 1$ which is not expected within a picture of noninteracting quasi-particles[112]. The $\nu = \pm 1$ symmetry broken states are associated with the valley splitting of the $n = 0$ Landaul level due to the electron-electron interactions[112–114]. In the hole branch, well-defined Shubnikov-de-Haas (SdH) oscillations are clearly observable at low magnetic field values before entering the quantum Hall regime [Fig. 6.9(b)].

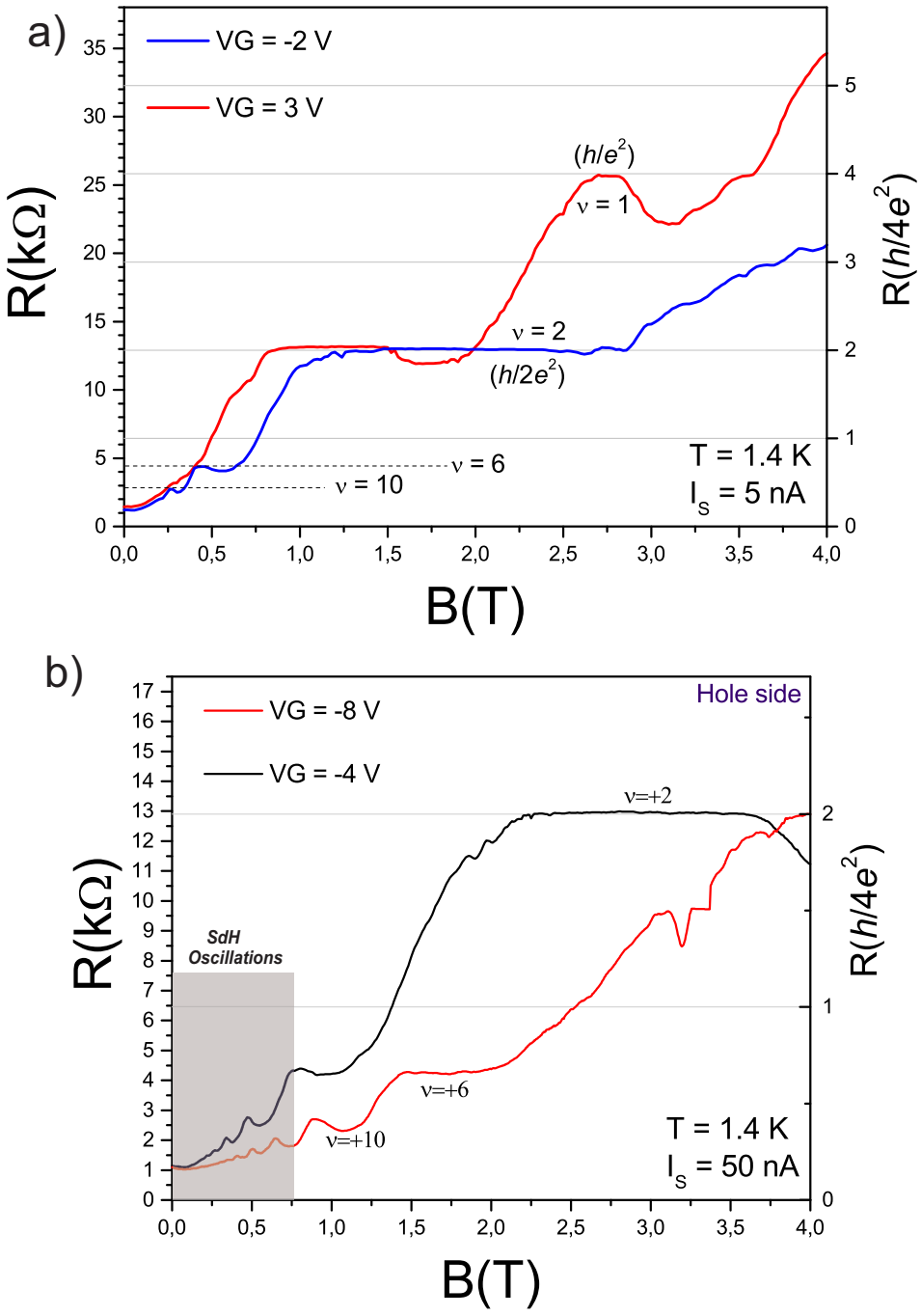

Figure 6.9: Quantum Hall effect plateaus of a suspended graphene sample (CY-17052015-SUB1-1). a) Red and blue curves correspond to electron and hole regime with a corresponding carrier densities of $\approx 6.7 \times 10^{10}\ cm^{-2}$ and $\approx 5.4 \times 10^{10}\ cm^{-2}$, respectively at 1.4 K, $I_S = 5\ nA$. Note that the $\nu = 1$ plateau at the electron branch. b) Quantizations at higher densities of the hole branch at 1.4 K, $I_S = 50\ nA$. Highlighted area exhibits the Shubnikov-de Haas oscillations.

Chapter 7

INSULATING BEHAVIOUR IN ULTRACLEAN SUSPENDED MONOLAYER GRAPHENE

In this chapter, we present our transport measurements on a thermo-pressure-cycled ultra-clean suspended monolayer graphene with extremely low potential fluctuations of $\delta n \lesssim 10^9\ cm^{-2}$ approaching the Dirac point. An insulating behavior developed during a thermo-pressure cycle has been observed and the results are discussed through the conductance fluctuations (CF) of a weakly disordered ultra-clean graphene sheet with strong short-range potentials which results in localization via intervalley backscattering.

7.0.1 Introduction

The nature of the conductivity at Dirac point has been debated since graphene's first isolation[10]. The saturation of the minimum conductivity in monolayer graphene has been observed even in ultra-clean high mobility suspended samples[25–29] well above the ballistic limit ($4e^2/\pi h$)[115, 116]. However, an insulating behavior around Dirac point has been realized by screening the charge puddles in so-called double-layer graphene heterostructures[117] or in top-gated graphene sheets on hBN substrates[118]. In disordered graphene, on the other hand, the minimum conductance is limited by saturation of the average carrier density in the presence of charge impurities. Scattering of the electrons off the impurity-induced potential leads to interesting quantum interference phenomena such as conductance fluctuations (CF)[119–122], and weak (anti) and strong localization[122–126].

A fundamental problem in quantum transport through mesoscopic devices is conductance fluctuations. Fluctuations of the conductance of electron systems have been widely studied in metals and semiconductors[127, 128]. They originate from the interference between phase-coherent electrons propagating in all possible paths through a mesoscopic system. As the Fermi energy of the conducting electrons or the magnetic flux through the sample is varied, the conductance can exhibit distinct fluctuations which can be either

universal or non-universal. In diffusive phase-coherent systems the average amplitude of these fluctuations is of the order of e^2/h, independent of the mean conductance, which is known as the universal conductance fluctuations (UCF)[127]. In conventional semiconductors and metals, the average amplitude of these fluctuations is a universal number giving rise to UCF. In graphene, however, due to its unique band structure with Dirac-like spectrum, the fluctuations of the conductance is highly dependent on the geometry of the device[129] as well as the the spatial distribution[121] and the strength of the scattering potentials in a disordered system[119, 130]. On the other hand, since the CF is a result of the interference of the scattered electron wave, it is also sensitive to the disorder strength and range, and spatial configuration of the scatterers[119, 121].

In general, there are two scattering mechanisms for graphene Dirac fermions which are intra-valley and inter-valley scattering. In the presence of long-range disorder potentials, for example in case of graphene on substrates, the electrons scatter in each of the two valleys without backscattering[131–133]. However, with short-range or strong long-range disorders[134], e.g., in graphene on hBN or suspended graphene, the dominant scattering is inter-valley scattering giving rise to backscattering and localization[135–138].

7.0.2 Results and Discussion

Here we report, for the first-time, on the observation of an insulating behavior in a suspended monolayer graphene around the charge neutrality point as a result of strong conductance fluctuations of the order of e^2/h which are the same order of the conductance itself. This insulating behavior at zero magnetic field has been developed during a thermo-pressure cycle of a high quality current-annealed[30] suspended sample. Moreover, we observed that a direct transition from an insulator to a Quantum Hall conductor occurs within $\approx\ 0.4\ T$. Another hallmark of our study is the emergence of $\nu = 0, \pm 1$ quantum Hall plateaus at $B \sim 1\ T$ besides the normal sequence of plateaux for single layer graphene, which we believe is a result of broken valley and spin symmetries[28]. These observations are described via weakly disordered ultra-clean graphene by strong short range inter-valley scatterers which lead to backscattering and valley symmetry breaking.

The studied suspended graphene device was fabricated by mechanical exfoliation of natural graphite transferred on to a p doped Si substrate covered by 285 nm of SiO_x. Single-layer graphene flakes are determined based on their contrast under the optical microscope, then confirmed by Raman spectroscopy. Electron beam lithography is employed to pattern the electrical contacts made from Cr/Au (3/100 nm) followed by a lift-off in acetone. Suspension is achieved by dipping the SiO_x in Buffered Oxide etcher (BOE)

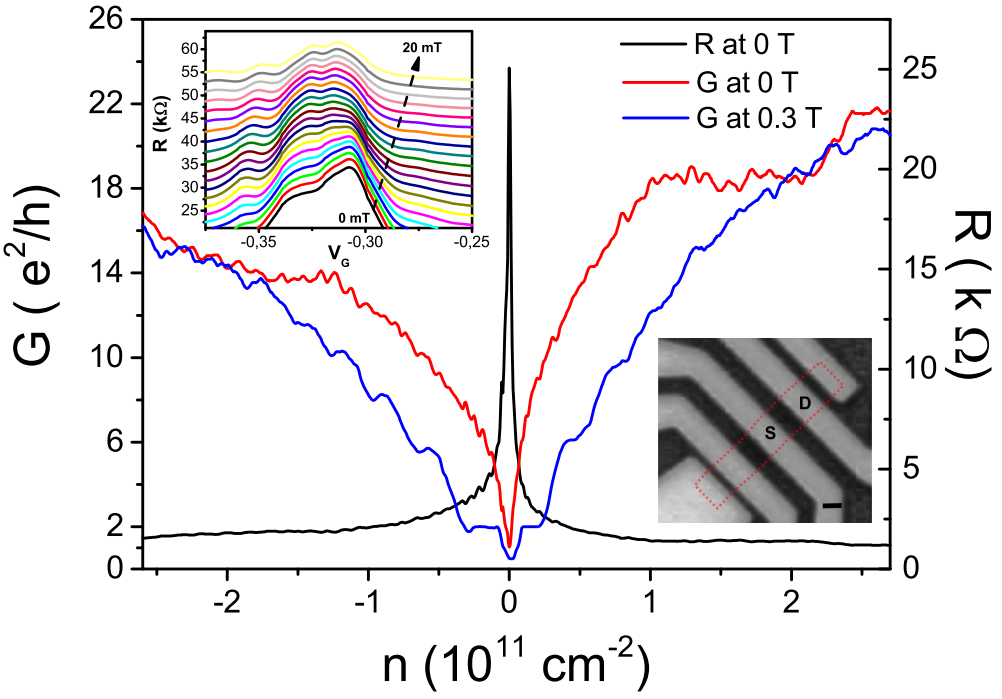

Figure 7.1: Resistance (black curve), Conductance (red curve) at zero magnetic field and Conductance (blue curve) at 300 mT as a function of carrier concentration after current annealing of suspended graphene with channel length $L = 1\ \mu m$ and width $W = 2\ \mu m$. The resistance peak is significantly narrow with the full width at half maximum (FWHM) of $(\delta n \approx 4 \times 10^9\ cm^{-2})$. The contact resistance of $\approx 0.9\ k\Omega$ is subtracted from the deviation of the expected conductance quantization values. Upper inset: $R(V_G)$ in various small B fields in the range of $1 - 20\ mT$ where the curves are shifted for clarity. Note that the Dirac point starts to split at B fields less than $10\ mT$. Lower inset: The optical microscope image of the measured device. Measurements were performed between the labelled Au leads as Source (S) and Drain (D) with $I_S = 10\ nA$ at $1.5\ K$. Dashed lines mark the borders of the suspended graphene which is not clearly visible under the optical microscope. Scale bar is $1\ \mu m$.

to remove $\approx$ 185 nm of SiO_x layer. The remaining oxide is allowed to avoid any shorts between the leads and Si layer. Device is transferred from BOE to DI water then dipped into isopropyl alcohol and dried by nitrogen gas (N2) gently. Electrical measurements on suspended device is performed in ^{3}He Dilution Refrigerator using the standard lock-in techniques. We performed current annealing by applying a DC current, with current densities of $j \approx 1\ mA/\mu m$, until the sample shows a remarkable feature on the resistance curve where the Dirac point is very close to 0 gate voltage indicating low unintentional doping [Fig. 7.1].

The resistance and conductance of the sample after current annealing is illustrated as a function of carrier concentration in Fig. 7.1. Carrier concentration varying by gate voltage, $n(V_g) = \alpha V_g$, is calculated with the coupling factor of $\alpha \approx 2.7 \times 10^{10} cm^{-2}$ obtained from the quantum Hall (QH) measurements in agreement with the parallel-plate capacitor model. As shown in Fig. 7.1, the sample was confirmed to be indeed a

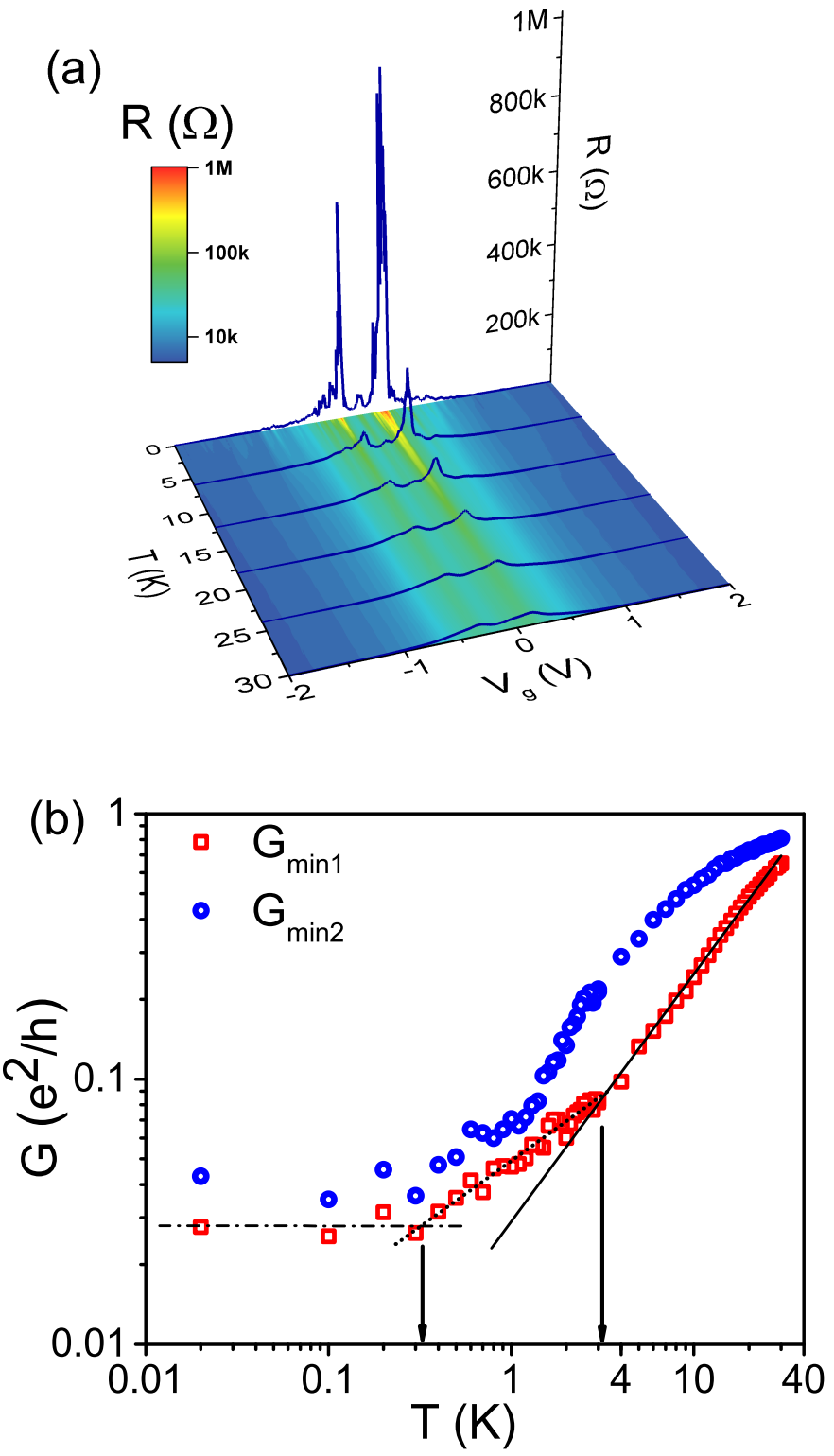

Figure 7.2: (a) Resistance as a function of V_g after thermo-pressure cycle at various temperatures at zero magnetic field. Note that the insulating peaks appear at $V_g = 0.15\ V$ and $V_g = -0.3V$. The resistance peaks at 20 mK are extremely narrow with FWHM of $\delta V_g \approx 0.07\ V$ translating to ($\delta n \approx 1.9 \times 10^9\ cm^{-2}$). The color scale corresponds to the surface plot. (b) The temperature behavior of conductance at insulating points in log-log scale labeled as G_{min1} and G_{min2} for $V_g = 0.15\ V$ and $V_g = -0.3\ V$, respectively. Black dotted line corresponds to a fit $G \propto T^{\beta}$, with $\beta = 1$ to G_{min1}. Note that this power-law behavior with $\beta = 1$ starts to diminish below $4K$. G_{min2} behaves slightly different at $T \gtrsim 4\ K$ whereas at lower temperatures both conductance minima follow the same trend.

monolayer graphene via QH measurements where conductance exhibits well developed quantized plateaus at $\nu = \pm 2, \pm 6, \pm 10$ already at $300\ mT$. Taking the aspect ratio of $W/L = 2$ into consideration, it should be noted that the maximum resistivity in our sample is $\sim 50\ k\Omega$ which can only be explained with an extremely clean sample with strongly reduced electron-hole puddles[139]. From the onset of the Shubnikov-de Haas oscillations at $8\ mT$, the mobility is estimated to exceed $10^6\ cm^2/(V-s)$ [Fig. 7.1upper inset].

However, after a thermo-pressure cycle to room temperature back to sub-Kelvin temperatures having the vacuum loosen up to maximum $\sim 10^{-2}\ mBar$ during the warm-up, the sample adopted a strong CF leading to insulating behavior around the charge neutrality point with high resistance peaks approaching mega-ohm range. We believe that the ultraclean sample has been weakly disordered during the thermo-pressure cycle by some adsorbents accompanying strong short-range potentials leading to pronounced conductance fluctuations and intervalley backscattering. In Fig. 7.2(a), the resistance as a function of gate voltage is plotted at various temperatures. The resistance is highly temperature dependent specially around the neutrality point with strong fluctuations leading to an insulating behavior at very low density regime. With reference to Fig.7.2, the temperature evolution of the resistance is addressed where the resistance fluctuation peaks are strongly dependent on temperature. However, no activation behavior is observed for these insulating peaks ruling out a gap-induced insulating behavior, which would lead to otherwise an exponentially activated conductivity. Indeed, the power-law behavior of the conductance [Fig. 7.2(b) is consistent with other experimental works on quality graphene devices[117, 118].

As the temperature is lowered, the quantum transport of electrons becomes coherent and leads to quantum interference corrections to the conductance. In Fig. 7.3, the relative fluctuations of conductance is illustrated in low density regime at different temperatures up to $25\ K$. It can be seen that by lowering the temperature the fluctuations of conductance is strongly pronounced around Dirac point corresponding to the insulating peaks in Fig. 7.2(a). The fluctuations are also reproducible at different temperatures and becomes so strong at lower temperatures that they can even diminish the conductance occasionally around the Dirac point leading to an insulating behavior when the carriers are totally localized in the bulk. The inset also shows the root mean square of the conductance fluctuations with respect to temperature with an exponential decay, $\delta G_{rms} \propto exp(T/T_0)$, where $T_0 \sim 11\ K$ above which the fluctuations start fading away.

Fig. 7.4 shows the field behavior of conductance as a function of carrier density. A direct transition from the insulating behavior around the Dirac point to QH regime can be

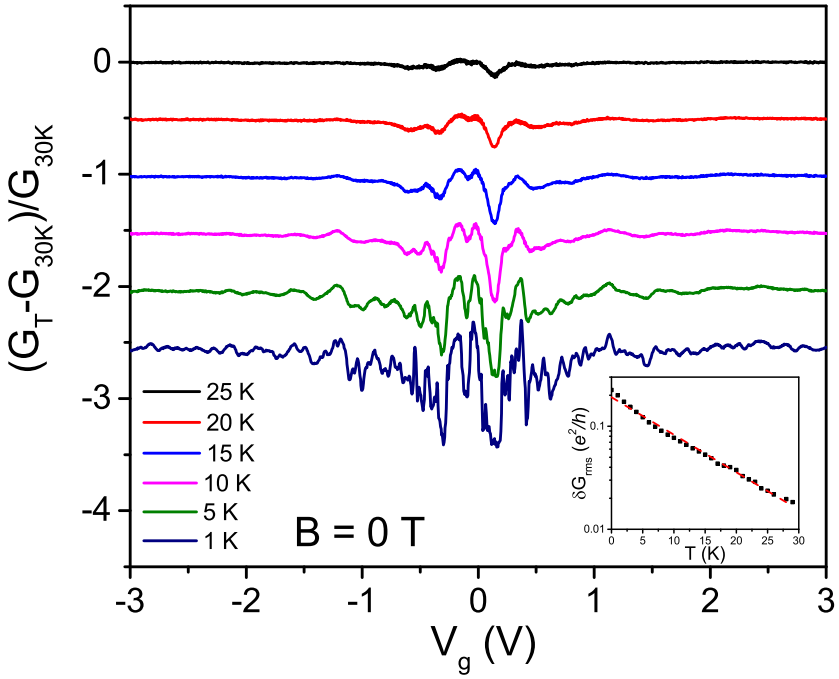

Figure 7.3: Relative conductance fluctuations at various temperatures with respect to the conductance at $30\ K$ at zero magnetic field. The plots are stacked for clarity. Inset: The root mean square of conductance fluctuations as a function of temperature in log-normal scale. The red dashed line shows the exponential fit.

seen by increasing the magnetic field up to $0.4\ T$ where a single conductance minimum at Dirac point appears with the development of $\nu = \pm 2$ plateaus around it. This behavior indicates that the bulk conductance is continuously vanishing with the current transport through edge channels until it fully enters the quantum Hall regime. Moreover, the sample displayed clear $\nu = 0, \pm 1$ plateaus besides the normal sequence of plateaux for a single layer graphene at relatively low magnetic fields[Fig. 7.4]. The presence of inter-valley scattering lifts the valley degeneracy and splitting the spin degeneracy at high enough magnetic fields ($\gtrsim 1\ T$) giving rise to this full symmetry-broken QH sequences[28, 140] which can only be resolved in ultra-clean samples.

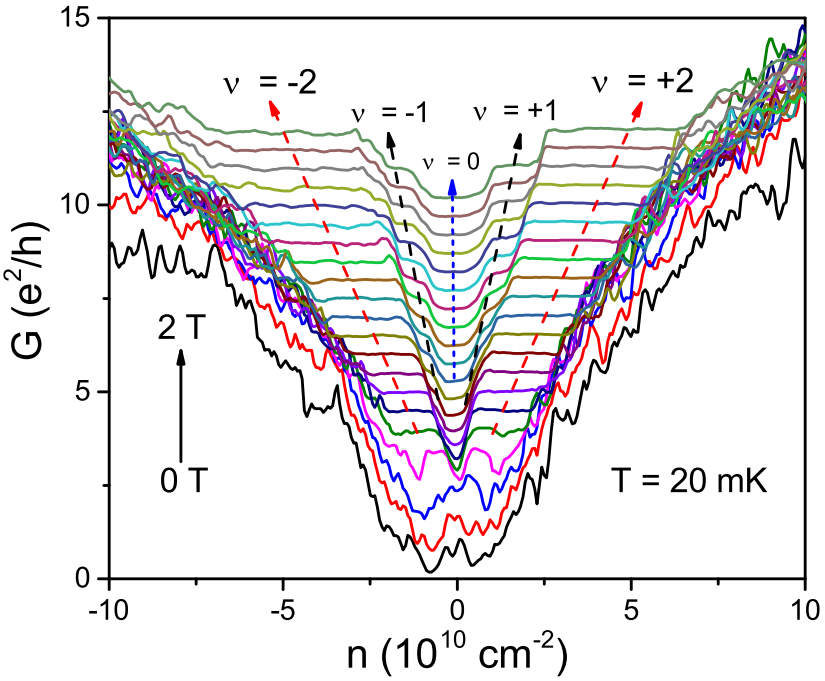

Figure 7.4: Two-terminal conductance at different magnetic fields up to 2 T. Insulating peaks declines monotonously to QH $\nu = \pm 2$ plateaus. The $\nu = 0, \pm 1$ plateaus also appear at around 1 T. The graphs are stacked with a constant amount.

7.0.3 Conlusions

In this chapter, we have investigated an unexpectedly high resistance peak in a current-annealed micron-size suspended graphene sheet, which is well above the ballistic limit. More interesting observation was a highly temperature-dependent insulating behavior in the suspended device after being disordered weakly by sharp atomic-scale impurity potentials during a thermo-pressure cycle. Such a low conductance around the charge neutrality point well below the ballistic limit $4e^2/\pi\ h$ before and after thermal cycle indicates that the sample is ultra clean and the transport is governed by the recently developed theory by Das Sarma et. al[140] which predicts a vanishing conductance and metal-insulator transition in higher quality samples. This behavior arises from the suppression of Coulomb disorder induced inhomogeneities near the charge neutrality point of very high quality samples. We believe our sample after current annealing was readily clean enough to show such an insulating behavior, however, after a thermal cycle, the adsorbent-induced inter-valley scattering brought the sample into a completely insulating regime near Dirac point. Lifting of the valley symmetry due to strong inter-valley scattering was also reflected in the QH measurements as a $\nu = 0, \pm 1$ plateau appearing at relatively small fields of $\sim 1\ T$.

Chapter 8

SUMMARY

There are two novel outcomes of this thesis:

First; we have analysed the breakdown of the quantum Hall effect in 1 μm wide Hall devices fabricated from an exfoliated monolayer graphene which is inherently 2D material transferred on SiO_x. We have observed that the deviation of the Hall resistance from its quantized value is weakly dependent on the longitudinal resistivity up to current density of 5 A/m, where the Hall resistance remains quantized even when the longitudinal resistance increases monotonously with the current. Then a collapse in the quantized resistance occurs while longitudinal resistance keeps its gradual increase. The exponential increase of the conductivity with respect to the current suggests impurity mediated inter-Landau level scattering as the mechanism of the breakdown. The results are interpreted as the strong variation of the breakdown behaviour throughout the sample due to the randomly distributed scattering centers that mediates the breakdown.

Second; we have presented the transport measurements of successfully annealed suspended graphene samples in which we achieved very high mobilities confirmed by an early onset of the Shubnikov-de Haas oscillations. Early appearance of a fully developed quantizations at low magnetic fields combined with broken symmetry states also confirm the quality of the devices. In one of these high quality samples which has a record carrier mobility (estimated to exceed 10^6 $cm^2V^{-1}s^{-1}$), an insulating behaviour at zero magnetic field was investigated after thermo-pressure-cycle. Before the thermo-pressure cycle, the sample was already in a high resistance regime by showing a peak resistivity of over 50 $k\Omega$ at Dirac point after current annealing which provides an extremely clean sample with highly reduced electron-hole puddles. However, after the thermo-pressure cycle, our current-annealed device acquired an insulating behavior around the neutrality point with a strong power-law dependency on temperature approaching $M\Omega$ range at 20 mK. This behavior is discussed through the conductance fluctuations (CF) of a weakly disordered ultra-clean graphene sheet but with strong short-range potentials which results in localization via intervalley backscattering. Moreover, by applying a perpendicular mag-

netic field, a direct transition from insulator to quantum Hall conductor is observed within $\approx 0.4\ T$ accompanied by broken-symmetry-induced $\nu = 0, \pm 1$ plateaux which confirms our picture of intervalley scatterers.

Appendix A

VISTEC EBPG 5000PLUSES STANDARD OPERATING PROCEDURE

Figure A.1: Vistec EBPG5000+ES 100 kV electron beam lithography system at Sabanci University Nanotechnology Research and Application Center's clean-room.

- Activate the monitors by moving the mouse.
- Check the system situation by monitoring the "CSYS". If it is not open, click the "EBPG5000+" icon on the desktop, "Cebpg" will be displayed on the screen then click "CSYS" from the upper short-cut panel.
- Vent the airlock by pressing the "set lock vent" button in "CSYS". Airlock will come to the atmosphere pressure in approx. 2 minutes [Fig. A.2(a)].

- Check the airlock whether it is in atmosphere pressure or not by just moving the arm up gently.
- Remove the cassette holder [Fig. A.2(b)].
- There are 2 holder in the "cassette holder". Upper side (Cassette 1) corresponds to the mask holder, down side (casette 2) is the piece part sample holder.
- After taking the holder, close the airlock lid, then check the lid is closed properly. Check the O-ring !
- Handle the holder carefully while carrying; NEVER TOUCH the calibration marker & Faraday Cup regions [Fig. A.2(c) upper part].
- While trying to place the sample on the holder, system must be kept in vacuum. From the "CYSY" press "set lock vacuum" button.
- You can put your sample either in low-y or high-y position via clipping with sample clips [Fig. A.2(c)].
- One should be careful with the orientation of the holder, adjust your sample orientation.
- After replacing your substrate properly, put the holder to the microscope stage carefully.
- Clamp the holder into the tray by just turning a quarter-clockwise(you will hear a click noise then stop), gently turning the screw in the counter-clockwise direction will release the spring and the holder [Fig. A.2(d)].
- Open the microscope and laser height meter, go to the faraday cup, put the cross on the right eyepiece to the center of faraday cup hole [Fig. A.2(e)].
- Make the position meter of X an Y "zero". Any movement is going to be relative to the faraday cup from now on [Fig. A.2(f)].
- Adjust your height with the three levelling set screws. If you turn fully in the clockwise direction, stage will go down approximately $200\ \mu m$ and vice versa. It obeys the RIGHT HAND RULE [Fig. A.2(f)].
- Height should be between max $-50\ \mu m$ to $+50\ \mu m$ range.

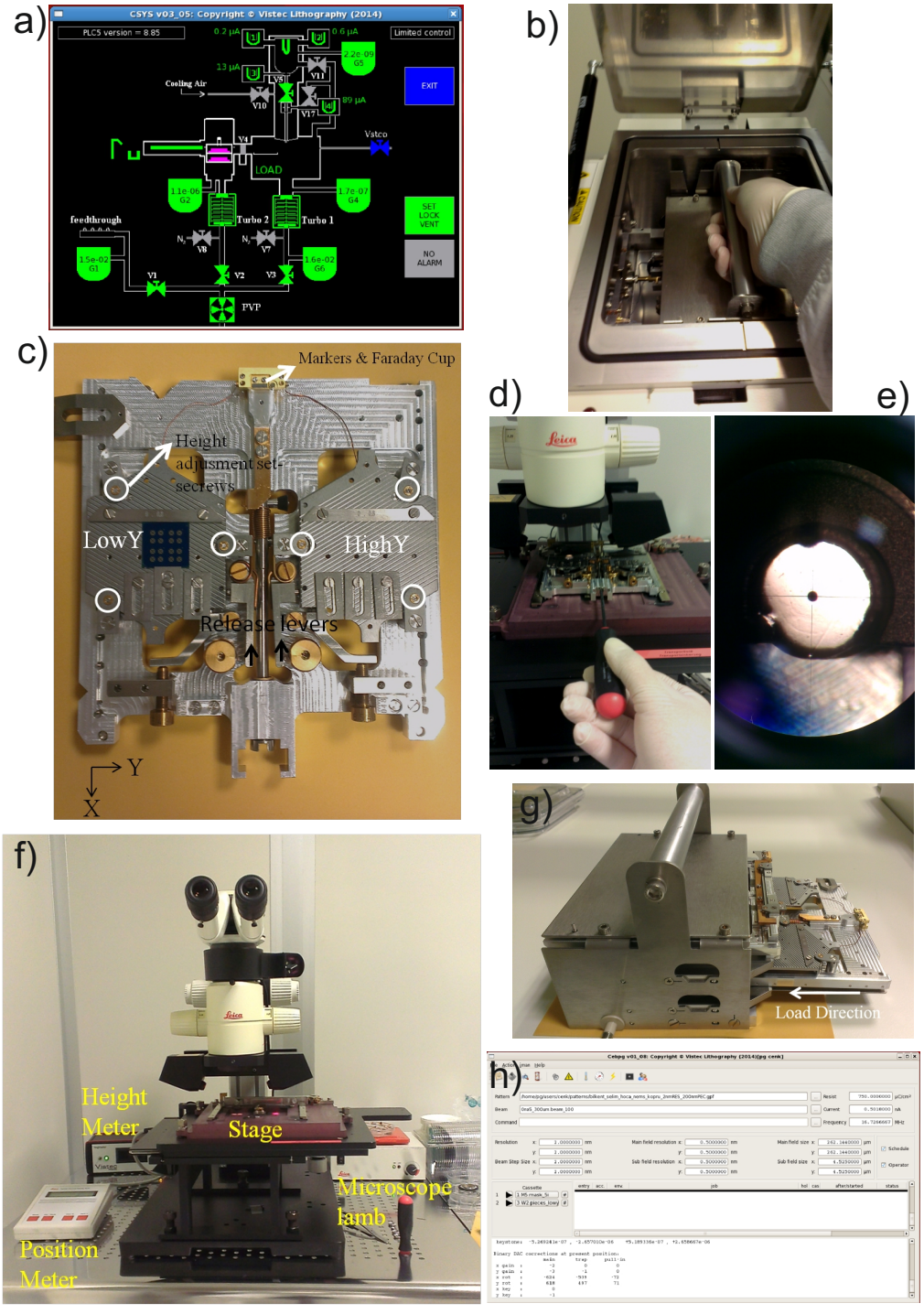

Figure A.2: Vistec EBPG500+ electron beam lithography direct write operating flow.

- If you have 1cm x 1cm substrate, from one side to other, height differences should not be higher than $10\ \mu m$ on the hight meter. ($1\ \mu m\ height/1\ mm\ length$).
- After you finish with the height alignment and taking the coordinate of your samples. (Take the both coordinates from the edge of the samples as X_1, X_2 and Y_1, Y_2, adding them up and dividing by 2, will give you the center of your substrate as (X_0, Y_0). Remove the holder. Do not forget to release the "release lever". For marker alignment, one should adjust the orientation and need to take the coordinate of the lower left marker in the layout.
- Vent the system from "CSYS" by pressing the vent the lock button again.
- Place the holder to the cassette [Fig. A.2(g)].
- Place the cassette to the airlock from the rails gently, you will hear a "click" voice when it is plugged properly, you can check also from the load arm head (T shape) should fit the big screw head of the holder.
- Set lock vacuum in "CSYS" again. Pumping will started and you will have to wait until the vacuum reaches the minimum required value of 5×10^{-5} TORR.
- When it reaches the required vacuum level, airlock region will turn intro green and cassette loading part in the "Cebpg" will highlighted [Fig. A.2(h)].
- You can select the holder type as Lowy (3) or highy (2) and strat loading the holder by just pressing arrow icon under the cassette in "Cebpg".
- Copy your gpf file from the LayoutBeamer-Machine folder on the desktop and paste it to the pattern file of your pg user account.
- Open a new terminal, change the environment to your environment by entering the " ce username" command (like ce cenk).
- NEVER give any "set", "measure", "adjust" commands, if there exist no holder inside the system. You can just give get information commands if there is no holder inside.
- After you change the environment open "cjop" by just entering "cjob" command into the terminal, then create your job file.
- In order to see archived currents in the system, enter the command as " pg information archive beam" - short command "iarc beam". It will list the archived beams. you can double click the one you would like to load.

- To load the current, you should enter the command as "pg archive restore beam ..... (middle click)". In Linux, highlighted region by double clicking will be pasted after middle clicking in the moue".
- To find the marker on the holder itself, you should enter "pg move marker" - "mvm" in shot.
- Only after it finds the marker, you should enter " pg adjust table coordinate" - " atc" in shot. This command should be entered only and only after " mvm" command !.
- To measure the the current, just enter " pg measure current" - "mcur" in short.
- Now you are on the faraday cup as your 0,0 position.
- Enter your center coordinates of X_0, Y_0 which are relative from the cup. "mpos /r X_0, Y_0"
- Now your are at the center of your substrate, you can check whether you are on the substrate or not by entering the "mpgm height" command. If it is in micron range, you are on the substrate then. If you are going to perform an alignment for the second ebeam step, then you have to enter your marker coordinate, go there and check shortly whether you are on the marker or not by just opening SEM module in "Cebpg".
- Take the coordinates of this point according to system's reference system as an absolute value by entering th" mpg tab" command.
- Copy this coordinates to parameters part in "Cebpg", chose your file, submit it then drag the panel bar down to start the exposure [Fig. A.2(h)]. Do not forget to change the environment in the "Cebpg" first.
- Leave the system in low beam currents (0.5 nA, 1 nA, etc.), high beam currents may damage the beam-blanker over the time.

Appendix B

OXFORD - 1.4 K- 12 TESLA CRYOSTAT - COOLING PROCEDURE

- Pump the Outer vacuum Jacket (OVC) and Variable Temperature Insert (VTI) of the cryostat ($< 10^{-5}\ mBar$)
- Check T-sensor -1 shows room temperature (RT) & LN_2 and LHe level sensors; -1 empty.
- insert the siphon pipe (sp) into he LHe refill (134 cm) connect the He gas to sp, flash for few minutes. Open the needle valves let the He gas flow diffuses every part.
- Pump the LHe reservoir (main bath) by Leybold rotary pump (< 1 mBar). Do not pump helium reservoir unless the OVC is already under vacuum, it may collapse if you do. Flush & pump Lambda Plate and VTI again. Repeat this process a few times (There must be no air inside!).
- Fill the He gas.
- Insert LN_2 transfer pipe into the LHe refill part then start LN_2 transfer. Do not let the pressure over 1 bar during the transfer.
- Check the ALLEN BRADLEY RESISTOR: Room temperature: 173.4 Ohm, 77 K: 195.95 Ohm [Fig. B.1].
- Stop LN_2 transfer when liquid comes out of the exhaust port. First close LN_2 dewar then remove the transfer tube from cryostat. Close tap on LHe refill part and plug the one-way vale to exhaust port.
- Leave the cryostat for a while for temperature stabilization.
- Approximately, % 40-50 of LN_2 must be remained when the transfer is finished.

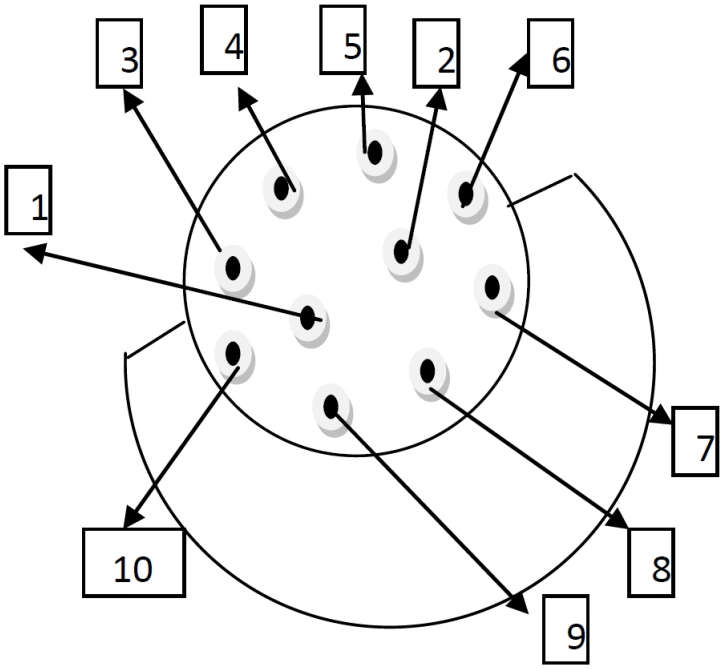

Figure B.1: Schematic of the Fisher connector: Allen Bradley resistor pins. At 77K; 3-Common, 4-100 mm above LPS: 195.75 Ohm, 5-On LPF: 196.20 Ohm, 6-Magnet Top: 194.70 Ohm. $R_{LEAD} + R_{COIL} = 34.37\ \Omega$.

- Observe T drops at VTI slowly towards 77 K.
- Keep the VTI & LPF needle valves closed.
- Place LHe transfer tube between the LHe refill part & LN_2 refill parts (Do not forget to pump the tube before transferring !). Keeps to fill the He gas through the butterfly valve part during the transfer, 200 mBar is enough).
- Pressurize the main LHe bath by He gas (0.1-0.2 bar).
- Leave one of 3 LN_2 parts open, observe the coming out gas. Gas flow will slow after 10-20 minutes as the LN_2 jacket cools down, indicating liquid collections.
- Observe the LN_2 level from the level sensors. If there is a problem with LN_2 levelling probe, plug it out, unscrew it and clean the coppers with sand papers to get rid of the oxidation. Hopefully, it should work.
- One has to be sure that there is no LN_2 in the LHe bath. Pump the bath and VTI. Then the pressure must go down around 1 mBar. If the pressure hesitates at any value above 1 mBar, it indicates that there is still LN_2 inside. You have to blow

it out. Leave one pipe in the LHe reservoir and take the other one out then check whether gas or LN_2 is coming out. Fill He gas and pump it. Another way to understand the remained LN_2 in the bath is to measure the Allen Bradley resistor which must be decreased compared to the 77 K values.

- Fill the He gas to sample stage and LHe bath before transferring the LHe and leaved the system pressurized He gas. If there is N_2 gas inside, needle valve might be freezed while cooling down to 4.2 K.

- When LHe transfer is started, The pressure of the dewar must be between 0.05 and 0.07 ($\approx 1\ Psi$). Transfer must be done slowly. Umplug the non-return valve during the LHe transfer. When the transfer is finished, replace the non-return valve to the helium reservoir exhaust.

Bibliography

[1] E. H. Hall, "On a new action of the magnet on electric currents," *American Journal of Mathematics*, vol. 2, no. 3, pp. 287–292, 1879.

[2] K. v. Klitzing, G. Dorda, and M. Pepper, "New method for high-accuracy determination of the fine-structure constant based on quantized hall resistance," *Phys. Rev. Lett.*, vol. 45, pp. 494–497, Aug 1980.

[3] A. H. Castro Neto, F. Guinea, N. M. R. Peres, K. S. Novoselov, and A. K. Geim, "The electronic properties of graphene," *Rev. Mod. Phys.*, vol. 81, pp. 109–162, Jan 2009.

[4] K. S. Novoselov, A. K. Geim, S. V. Morozov, D. Jiang, M. I. Katsnelson, I. V. Grigorieva, S. V. Dubonos, and A. A. Firsov, "Two-dimensional gas of massless dirac fermions in graphene," *Nature*, vol. 438, no. 7065, pp. 197–200, 2005.

[5] G. Nachtwei, "Breakdown of the quantum hall effect," *Physica E: Low-dimensional Systems and Nanostructures*, vol. 4, no. 2, pp. 79 – 101, 1999.

[6] L. Eaves and F. W. Sheard, "Size-dependent quantised breakdown of the dissipationless quantum hall effect in narrow channels," *Semicond. Sci. Technol.*, vol. 1, pp. 346–349, 1986.

[7] S. Kawaji, H. Iizuka, T. Kuga, and T. Okamoto, "Collapse of quantized hall resistance at high hall electric fields," *Physica B*, vol. 256-258, pp. 56–59, 1998.

[8] P. R. Wallace, "The band theory of graphite," *Phys. Rev.*, vol. 71, pp. 622–634, May 1947.

[9] N. D. Mermin, "Crystalline order in two dimensions," *Physical Review*, vol. 176, no. 1, p. 250, 1968.

[10] K. S. Novoselov, A. K. Geim, S. V. Morozov, D. Jiang, Y. Zhang, S. V. Dubonos, I. V. Grigorieva, and A. A. Firsov, "Electric field effect in atomically thin carbon films," *science*, vol. 306, no. 5696, pp. 666–669, 2004.

[11] K. v. Klitzing, "Physics and application of the quantum hall effect," *Physica B: Condensed Matter*, vol. 204, no. 1, pp. 111–116, 1995.

[12] G. Ebert, K. v. Klitzing, K. Ploog, and G. Wiemann, "Two-dimensional magneto-quantum transport on gaas-algaas heterostructures under non-ohmic conditions," *J. Phys. C: Solid State Phys.*, vol. 16, pp. 5441–5448, 1983.

[13] M. E. Cage, R. F. Dziuba, B. F. Field, E. R. Williams, S. M. Girvin, A. C. Gossard, D. C. Tsui, and R. J. Wagner, "Dissipation and dynamic nonlinear behavior in the quantum hall regime," *Physical Review Letters*, vol. 51, no. 15, pp. 1374–1377, 1983.

[14] K. S. Novoselov, Z. Jiang, Y. Zhang, S. V. Morozov, H. L. Stormer, U. Zeitler, J. C. Maan, G. S. Boebinger, P. Kim, and A. K. Geim, "Room-temperature quantum hall effect in graphene," *Science*, vol. 315, no. 5817, pp. 1379–1379, 2007.

[15] J. Guignard, D. Leprat, D. C. Glattli, F. Schopfer, and W. Poirier, "Quantum hall effect in exfoliated graphene affected by charged impurities: Metrological measurements," *Physical Review B*, vol. 85, no. 16, 2012.

[16] M. Woszczyna, M. Friedemann, M. GoÌĹtz, E. Pesel, K. Pierz, T. Weimann, and F. J. Ahlers, "Precision quantization of hall resistance in transferred graphene," *Applied Physics Letters*, vol. 100, no. 16, p. 164106, 2012.

[17] A. Tzalenchuk, S. Lara-Avila, A. Kalaboukhov, S. Paolillo, M. Syvajarvi, R. Yakimova, O. Kazakova, T. J. Janssen, V. Fal'ko, and S. Kubatkin, "Towards a quantum resistance standard based on epitaxial graphene," *Nat Nanotechnol*, vol. 5, no. 3, pp. 186–9, 2010.

[18] T. J. B. M. Janssen, N. E. Fletcher, R. Goebel, J. M. Williams, A. Tzalenchuk, R. Yakimova, S. Kubatkin, S. Lara-Avila, and V. I. Falko, "Graphene, universality of the quantum hall effect and redefinition of the si system," *New Journal of Physics*, vol. 13, no. 9, p. 093026, 2011.

[19] T. J. B. M. Janssen, A. Tzalenchuk, R. Yakimova, S. Kubatkin, S. Lara-Avila, S. Kopylov, and V. I. FalâĂŹko, "Anomalously strong pinning of the filling factorÎ¡=2in epitaxial graphene," *Physical Review B*, vol. 83, no. 23, 2011.

[20] A. Satrapinski, S. Novikov, and N. Lebedeva, "Precision quantum hall resistance measurement on epitaxial graphene device in low magnetic field," *Applied Physics Letters*, vol. 103, no. 17, p. 173509, 2013.

[21] C.-C. Kalmbach, J. Schurr, F. Ahlers, A. Müller, S. Novikov, N. Lebedeva, and A. Satrapinski, "Towards a graphene-based quantum impedance standard," *Applied Physics Letters*, vol. 105, no. 7, p. 073511, 2014.

[22] F. Lafont, R. Ribeiro-Palau, D. Kazazis, A. Michon, O. Couturaud, C. Consejo, T. Chassagne, M. Zielinski, M. Portail, B. Jouault, *et al.*, "Quantum hall resistance standards from graphene grown by chemical vapour deposition on silicon carbide," *Nature communications*, vol. 6, 2015.

[23] J. Alexander-Webber, J. Huang, D. Maude, T. Janssen, A. Tzalenchuk, V. Antonov, T. Yager, S. Lara-Avila, S. Kubatkin, R. Yakimova, *et al.*, "Giant quantum hall plateaus generated by charge transfer in epitaxial graphene," *Scientific Reports*, vol. 6, p. 30296, 2016.

[24] T. Janssen, S. Rozhko, I. Antonov, A. Tzalenchuk, J. Williams, Z. Melhem, H. He, S. Lara-Avila, S. Kubatkin, and R. Yakimova, "Operation of graphene quantum hall resistance standard in a cryogen-free table-top system," *2D Materials*, vol. 2, no. 3, p. 035015, 2015.

[25] X. Du, I. Skachko, A. Barker, and E. Y. Andrei, "Approaching ballistic transport in suspended graphene," *Nat. Nano*, vol. 3, no. 8, pp. 491–495, 2008.

[26] K. I. Bolotin, K. Sikes, Z. Jiang, M. Klima, G. Fudenberg, J. Hone, P. Kim, and H. Stormer, "Ultrahigh electron mobility in suspended graphene," *Solid State Communications*, vol. 146, no. 9, pp. 351–355, 2008.

[27] X. Du, I. Skachko, F. Duerr, A. Luican, and E. Y. Andrei, "Fractional quantum hall effect and insulating phase of dirac electrons in graphene," *Nature*, vol. 462, no. 7270, pp. 192–195, 2009.

[28] K. I. Bolotin, F. Ghahari, M. D. Shulman, H. L. Stormer, and P. Kim, "Observation of the fractional quantum hall effect in graphene," *Nature*, vol. 462, no. 7270, pp. 196–199, 2009.

[29] A. S. Mayorov, D. C. Elias, I. S. Mukhin, S. V. Morozov, L. A. Ponomarenko, K. S. Novoselov, A. Geim, and R. V. Gorbachev, "How close can one approach the dirac point in graphene experimentally?," *Nano letters*, vol. 12, no. 9, pp. 4629–4634, 2012.

[30] J. Moser, A. Barreiro, and A. Bachtold, "Current-induced cleaning of graphene," *Appl. Phys. Lett.*, vol. 91, no. 16, 2007.

[31] M. Marder, *Condensed Matter Physics*. Wiley, 2010.

[32] M. Dresselhaus, "Two dimensional electron gas, quantum wells and semiconductor superlattices," 2001.

[33] D. J. Griffiths, *Introduction to quantum mechanics*. Pearson Education India, 2005.

[34] B. Simons, "Advanced quantum mechanics," 2009.

[35] D. Tong, "The quantum hall effect lectures," 2016.

[36] R. B. Laughlin, "Quantized hall conductivity in two dimensions," *Physical Review B*, vol. 23, no. 10, p. 5632, 1981.

[37] R. Landauer, "Spatial variation of currents and fields due to localized scatterers in metallic conduction," *IBM Journal of Research and Development*, vol. 1, no. 3, pp. 223–231, 1957.

[38] R. Landauer, "Electrical transport in open and closed systems," *Zeitschrift für Physik B Condensed Matter*, vol. 68, no. 2-3, pp. 217–228, 1987.

[39] M. Büttiker, "Absence of backscattering in the quantum hall effect in multiprobe conductors," *Physical Review B*, vol. 38, no. 14, p. 9375, 1988.

[40] L. Bliek, E. Braun, G. Hein, V. Kose, J. Niemeyer, G. Weimann, and W. Schlapp, "Critical current density for the dissipationless quantum hall effect," *Semiconductor science and technology*, vol. 1, no. 2, p. 110, 1986.

[41] S. Komiyama, Y. Kawaguchi, T. Osada, and Y. Shiraki, "Evidence of nonlocal breakdown of the integer quantum hall effect," *Physical review letters*, vol. 77, no. 3, p. 558, 1996.

[42] Y. Kawaguchi, S. Komiyama, T. Osada, and Y. Shiraki, "Nonlocal nature of the breakdown of the integer quantum hall effects," *Physica B: Condensed Matter*, vol. 227, no. 1, pp. 183–185, 1996.

[43] S. Kawaji, K. Hirakawa, and M. Nagata, "Device-width dependence of plateau width in quantum hall states," *Physica B: Condensed Matter*, vol. 184, no. 1, pp. 17–20, 1993.

[44] S. Kawaji, K. Hirakawa, M. Nagata, T. Okamoto, T. Fukuse, and T. Gotoh, "Breakdown of the quantum hall effect in gaas/algaas heterostructures due to current," *Journal of the Physical Society of Japan*, vol. 63, no. 6, pp. 2303–2313, 1994.

[45] S. Kawaji, K. Hirakawa, M. Nagata, T. Okamoto, T. Fukase, and T. Goto, "Magnetic field dependence of the device-width-dependent breakdown current in the quantum hall effect," *Surface science*, vol. 305, no. 1, pp. 161–165, 1994.

[46] A. Boisen, P. Bo, A. Kristensen, P. Lindelof, *et al.*, "Nonlinear current-voltage characteristics at quantum hall resistance minima," *Physical Review B*, vol. 50, no. 3, p. 1957, 1994.

[47] N. Balaban, U. Meirav, H. Shtrikman, and Y. Levinson, "Scaling of the critical current in the quantum hall effect: a probe of current distribution," *Physical review letters*, vol. 71, no. 9, p. 1443, 1993.

[48] J. Kirtley, Z. Schlesinger, T. Theis, F. Milliken, S. Wright, and L. Palmateer, "Low-voltage breakdown of the quantum hall state in a laterally constricted two-dimensional electron gas," *Physical Review B*, vol. 34, no. 2, p. 1384, 1986.

[49] M. Cage, G. M. Reedtz, D. Yu, and C. Van Degrift, "Quantised dissipative states at breakdown of the quantum hall effect," *Semiconductor Science and Technology*, vol. 5, no. 4, p. 351, 1990.

[50] M. Cage, "Dependence of quantized hall effect breakdown voltage on magnetic field and current," *JOURNAL OF RESEARCH-NATIONAL INSTITUTE OF STANDARDS AND TECHNOLOGY*, vol. 98, pp. 361–361, 1993.

[51] I. I. Kaya, G. Nachtwei, K. Von Klitzing, and K. Eberl, "Spatially resolved montoring of the evolution of the breakdown of the quantum hall effect: Direct observation of inter-landau-level tunneling," *Europhys. Lett.*, vol. 46, no. 1, pp. 62–67, 1999.

[52] I. I. Kaya, G. Nachtwei, K. von Klitzing, and K. Eberl, "Spatial evolution of hot-electron relaxation in quantum hall conductors," *Phys. Rev. B*, vol. 58, pp. R7536–R7539, Sep 1998.

[53] I. Kaya, G. Nachtwei, K. Von Klitzing, and K. Eberl, "Dynamics of nonequilibrium electrons at the breakdown of the quantum hall effect," *Physica B: Condensed Matter*, vol. 256, pp. 8–15, 1998.

[54] S. Komiyama, T. Takamasu, S. Hiyamizu, and S. Sasa, "Breakdown of the quantum hall effect due to electron heating," *Solid State Communications*, vol. 54, no. 6, pp. 479 – 484, 1985.

[55] T. Takamasu, S. Komiyama, S. Hiyamizu, and S. Sasa, "Effect of finite electric field on the quantum hall effect," *Surface Science*, vol. 170, no. 1, pp. 202 – 208, 1986.

[56] S. Komiyama and Y. Kawaguchi, "Heat instability of quantum hall conductors," *Physical Review B*, vol. 61, no. 3, p. 2014, 2000.

[57] K. Güven, R. R. Gerhardts, I. I. Kaya, B. E. Sağol, and G. Nachtwei, "Two-level model for the generation and relaxation of hot electrons near the breakdown of the quantum hall effect," *Phys. Rev. B*, vol. 65, p. 155316, Mar 2002.

[58] P. Streda and K. v. Klitzing, "Critical non-dissipative current of the quantum hall regime," *J. Phys. C: Solid State Phys.*, vol. 17, no. 19, p. L483, 1984.

[59] O. G. Balev and P. Vasilopoulos, "Low-voltage breakdown of the quantum hall effect in narrow channels," *Physical Review B*, vol. 47, no. 24, pp. 16410–16418, 1993.

[60] B. Jeckelmann and B. Janneret, "The quantum hall effect as an electrical resistance standard," *Rep. Prog. Phys.*, vol. 64, pp. 1603–1655, 2001.

[61] F. Piquemal, G. Geneves, F. Dlahaye, J.-P. Andre, J.-N. Patillon, and P. Frijilink, "Report on a joint bipm-euromet project for the fabricaiton of qhe samples by the lep," *IEEE Trans . Instrum. Meas.*, vol. 42, no. 2, 1993.

[62] A. J. M. Giesbers, G. Rietveld, E. Houtzager, U. Zeitler, R. Yang, K. S. Novoselov, A. K. Geim, and J. C. Maan, "Quantum resistance metrology in graphene," *Applied Physics Letters*, vol. 93, no. 22, p. 222109, 2008.

[63] V. Singh and M. M. Deshmukh, "Nonequilibrium breakdown of quantum hall state in graphene," *Physical Review B*, vol. 80, no. 8, 2009.

[64] A. M. R. Baker, J. A. Alexander-Webber, T. Altebaeumer, and R. J. Nicholas, "Energy relaxation for hot dirac fermions in graphene and breakdown of the quantum hall effect," *Physical Review B*, vol. 85, no. 11, 2012.

[65] J. Alexander-Webber, A. Baker, T. Janssen, A. Tzalenchuk, S. Lara-Avila, S. Kubatkin, R. Yakimova, B. Piot, D. Maude, and R. Nicholas, "Phase space for the breakdown of the quantum hall effect in epitaxial graphene," *Physical review letters*, vol. 111, no. 9, p. 096601, 2013.

[66] T. Okuno, S. Kawaji, T. Ohrui, T. Okamoto, Y. Kurata, and J. Sakai, "Electron concentration and mobility dependence of breakdown of the quantum hall effect," *Journal of the Physical Society of Japan*, vol. 64, no. 6, pp. 1881–1884, 1995, http://dx.doi.org/10.1143/JPSJ.64.1881.

[67] W. Poirier and F. Schopfer, "Resistance metrology based on the quantum hall effect," *The European Physical Journal Special Topics*, vol. 172, no. 1, pp. 207–245, 2009.

[68] H. Tanaka, H. Kawashima, H. Iizuka, H. Fukuda, and S. Kawaji, "Temperature dependence of collapse of quantized hall resistance," *Journal of the Physical Society of Japan*, vol. 75, no. 1, p. 014701, 2005.

[69] K. yoshlhiro, J. Kinoshita, K. Inagaki, C. Yamanouchi, J. Moriyama, and S. Kawaji, "High precision measurements of the hall effect for silicon mos inversion layers in strong magnetic fields," *Surface Science*, vol. 113, no. 1, pp. 16 – 21, 1982.

[70] T. Ando and Y. Uemura, "Theory of quantum transport in a two-dimensional electron system under magnetic fields. i. characteristics of level broadening and transport under strong fields," *Journal of the Physical Society of Japan*, vol. 36, no. 4, pp. 959–967, 1974, http://dx.doi.org/10.1143/JPSJ.36.959.

[71] T. Ando, "Theory of quantum transport in a two-dimensional electron system under magnetic fields ii. single-site approximation under strong fields," *Journal of the Physical Society of Japan*, vol. 36, no. 6, pp. 1521–1529, 1974, http://dx.doi.org/10.1143/JPSJ.36.1521.

[72] T. Ando, "Theory of quantum transport in a two-dimensional electron system under magnetic fields. iii. many-site approximation," *Journal of the Physical Society of Japan*, vol. 37, no. 3, pp. 622–630, 1974, http://dx.doi.org/10.1143/JPSJ.37.622.

[73] T. Ando, Y. Matsumoto, and Y. Uemura, "Theory of hall effect in a two-dimensional electron system," *Journal of the Physical Society of Japan*, vol. 39, no. 2, pp. 279–288, 1975, http://dx.doi.org/10.1143/JPSJ.39.279.

[74] R. R. Gerhardts, "Path-integral approach to the two-dimensional magneto-conductivity problem: I. general formulaiton of the approach; ii. application to n-type (100)- surface unversion layers of p-silicon," *Zeitschrift für Physik B Condensed Matter*, vol. 21, no. 4, pp. 275–285, 1975.

[75] R. R. Gerhardts, "Self-consistent transport equations for the electron-impurity system in a magnetic field," *Zeitschrift für Physik B Condensed Matter*, vol. 22, no. 4, pp. 327–336, 1975.

[76] H. Aoki and T. Ando, "Effect of localization on the hall conductivity in the two-dimensional system in strong magnetic fields," *Solid State Communications*, vol. 38, no. 11, pp. 1079 – 1082, 1981.

[77] U. Klass, W. Dietsche, K. Von Klitzing, and K. Ploog, "Imaging of the dissipation in quantum-hall-effect experiments," *Zeitschrift für Physik B Condensed Matter*, vol. 82, no. 3, pp. 351–354, 1991.

[78] H. Zheng, D. Tsui, and A. M. Chang, "Distribution of the quantized hall potential in gaas-al x ga 1- x as heterostructures," *Physical Review B*, vol. 32, no. 8, p. 5506, 1985.

[79] E. Sichel, M. Knowles, and H. Sample, "Equipotential distribution in the quantum hall effect in gaas-algaas heterostructures," *Journal of Physics C: Solid State Physics*, vol. 19, no. 28, p. 5695, 1986.

[80] B. Kane, D. Tsui, and G. Weimann, "Evidence for edge currents in the integral quantum hall effect," *Physical review letters*, vol. 59, no. 12, p. 1353, 1987.

[81] C. Yanık and I. I. Kaya, "Local breakdown of the quantum hall effect in narrow single layer graphene hall devices," *Solid State Communications*, vol. 160, pp. 47–51, 2013.

[82] S. Trugman and F. Waugh, "Complex scattering dynamics and the integral quantum hall effect," *Surface Science*, vol. 196, no. 1, pp. 171–176, 1988.

[83] S. Trugman, "Complex classical and quantum scattering dynamics and the quantum hall effect," *Physical review letters*, vol. 62, no. 5, p. 579, 1989.

[84] V. N. Nicopoulos and S. Trugman, "Complex quantum scattering and the breakdown of the quantum hall effect," *Physical review letters*, vol. 65, no. 6, p. 779, 1990.

[85] S. Komiyama, T. Takamasu, S. Hiyamizu, and S. Sasa, "Breakdown of the quantum hall effect due to electron heating," *Solid state communications*, vol. 54, no. 6, pp. 479–484, 1985.

[86] T. Takamasu, S. Komiyama, S. Hiyamizu, and S. Sasa, "Effect of finite electric field on the quantum hall effect," *Surface science*, vol. 170, no. 1-2, pp. 202–208, 1986.

[87] C. Berger, Z. Song, X. Li, X. Wu, N. Brown, C. Naud, D. Mayou, T. Li, J. Hass, A. N. Marchenkov, *et al.*, "Electronic confinement and coherence in patterned epitaxial graphene," *Science*, vol. 312, no. 5777, pp. 1191–1196, 2006.

[88] W. A. De Heer, C. Berger, X. Wu, P. N. First, E. H. Conrad, X. Li, T. Li, M. Sprinkle, J. Hass, M. L. Sadowski, *et al.*, "Epitaxial graphene," *Solid State Communications*, vol. 143, no. 1, pp. 92–100, 2007.

[89] K. V. Emtsev, A. Bostwick, K. Horn, J. Jobst, G. L. Kellogg, L. Ley, J. L. McChesney, T. Ohta, S. A. Reshanov, J. Röhrl, *et al.*, "Towards wafer-size graphene layers by atmospheric pressure graphitization of silicon carbide," *Nature materials*, vol. 8, no. 3, pp. 203–207, 2009.

[90] X. Li, W. Cai, J. An, S. Kim, J. Nah, D. Yang, R. Piner, A. Velamakanni, I. Jung, E. Tutuc, *et al.*, "Large-area synthesis of high-quality and uniform graphene films on copper foils," *Science*, vol. 324, no. 5932, pp. 1312–1314, 2009.

[91] C. Celebi, C. Yanık, A. G. Demirkol, and I. I. Kaya, "The effect of a sic cap on the growth of epitaxial graphene on sic in ultra high vacuum," *Carbon*, vol. 50, no. 8, pp. 3026–3031, 2012.

[92] C. Çelebi, C. Yanık, A. Demirkol, and I. I. Kaya, "Control of the graphene growth rate on capped sic surface under strong si confinement," *Applied Surface Science*, vol. 264, pp. 56–60, 2013.

[93] R. R. Nair, P. Blake, A. N. Grigorenko, K. S. Novoselov, T. J. Booth, T. Stauber, N. M. Peres, and A. K. Geim, "Fine structure constant defines visual transparency of graphene," *Science*, vol. 320, no. 5881, pp. 1308–1308, 2008.

[94] P. Blake, E. Hill, A. C. Neto, K. Novoselov, D. Jiang, R. Yang, T. Booth, and A. Geim, "Making graphene visible," *Applied Physics Letters*, vol. 91, no. 6, p. 063124, 2007.

[95] W. G. Cullen, M. Yamamoto, K. M. Burson, J. Chen, C. Jang, L. Li, M. S. Fuhrer, and E. D. Williams, "High-fidelity conformation of graphene to sio 2 topographic features," *Physical review letters*, vol. 105, no. 21, p. 215504, 2010.

[96] A. Ferrari, J. Meyer, V. Scardaci, C. Casiraghi, M. Lazzeri, F. Mauri, S. Piscanec, D. Jiang, K. Novoselov, S. Roth, *et al.*, "Raman spectrum of graphene and graphene layers," *Physical review letters*, vol. 97, no. 18, p. 187401, 2006.

[97] A. C. Ferrari and D. M. Basko, "Raman spectroscopy as a versatile tool for studying the properties of graphene," *Nature nanotechnology*, vol. 8, no. 4, pp. 235–246, 2013.

[98] J. Martin, N. Akerman, G. Ulbricht, T. Lohmann, K. von Klitzing, J. H. Smet, and A. Yacoby, "The nature of localization in graphene under quantum hall conditions," *Nat. Phys.*, vol. 5, no. 9, pp. 669–674, 2009.

[99] A. J. Giesbers, U. Zeitler, M. I. Katsnelson, L. A. Ponomarenko, T. M. Mohiuddin, and J. C. Maan, "Quantum-hall activation gaps in graphene," *Phys Rev Lett*, vol. 99, no. 20, p. 206803, 2007.

[100] E. V. Kurganova, S. Wiedmann, A. J. M. Giesbers, R. V. Gorbachev, K. S. Novoselov, M. I. Katsnelson, T. Tudorovskiy, J. C. Maan, and U. Zeitler, "Quantized coexisting electrons and holes in graphene measured using temperature-dependent magnetotransport," *Phys. Rev. B*, vol. 87, p. 085447, Feb 2013.

[101] K. Yoshihiro, J. Kinoshita, K. Inagaki, C. Yamanouchi, J. Moriyama, and S. Kawaji, "Quantized hall and transverse resistivities in silicon mos n-inversion layers," *Physica B+C*, vol. 117, pp. 706 – 708, 1983.

[102] M. E. Cage, B. F. Field, R. F. Dziuba, S. M. Girvin, A. C. Gossard, and D. C. Tsui, "Temperature dependence of the quantum hall resistance," *Physical Review B*, vol. 30, no. 4, pp. 2286–2288, 1984.

[103] W. van der Wel, C. J. P. M. Harmans, and J. E. Mooij, "A geometric explanation of the temperature dependence of the quantised hall resistance," *Journal of Physics C: Solid State Physics*, vol. 21, no. 7, p. L171, 1988.

[104] M. D'Iorio and B. Wood, "Temperature dependence of the quantum hall resistance," *Surface Science*, vol. 170, no. 1, pp. 233 – 237, 1986.

[105] M. Furlan, "Electronic transport and the localization length in the quantum hall effect," *Phys. Rev. B*, vol. 57, pp. 14818–14828, Jun 1998.

[106] A. S. Sachrajda, D. Landheer, R. Boulet, and T. Moore, "Evidence for an inhomogeneity size effect in narrowgaas/alxga1âĹŠxasconstrictions," *Physical Review B*, vol. 39, no. 14, pp. 10460–10463, 1989.

[107] S. Morozov, K. Novoselov, M. Katsnelson, F. Schedin, D. Elias, J. A. Jaszczak, and A. Geim, "Giant intrinsic carrier mobilities in graphene and its bilayer," *Physical review letters*, vol. 100, no. 1, p. 016602, 2008.

[108] D.-K. Ki and A. F. Morpurgo, "High-quality multiterminal suspended graphene devices," *Nano letters*, vol. 13, no. 11, pp. 5165–5170, 2013.

[109] K. I. Bolotin, K. J. Sikes, J. Hone, H. L. Stormer, and P. Kim, "Temperature-dependent transport in suspended graphene," *Phys. Rev. Lett.*, vol. 101, no. 9, p. 096802, 2008.

[110] Y. Zheng, G.-X. Ni, C.-T. Toh, C.-Y. Tan, K. Yao, and B. Özyilmaz, "Graphene field-effect transistors with ferroelectric gating," *Physical review letters*, vol. 105, no. 16, p. 166602, 2010.

[111] S. Kim, J. Nah, I. Jo, D. Shahrjerdi, L. Colombo, Z. Yao, E. Tutuc, and S. K. Banerjee, "Realization of a high mobility dual-gated graphene field-effect transistor with al2o3 dielectric," *Applied Physics Letters*, vol. 94, no. 6, 2009.

[112] Z. Jiang, Y. Zhang, H. Stormer, and P. Kim, "Quantum hall states near the charge-neutral dirac point in graphene," *Physical review letters*, vol. 99, no. 10, p. 106802, 2007.

[113] A. F. Young, C. R. Dean, L. Wang, H. Ren, P. Cadden-Zimansky, K. Watanabe, T. Taniguchi, J. Hone, K. L. Shepard, and P. Kim, "Spin and valley quantum hall ferromagnetism in graphene," *Nature Physics*, vol. 8, no. 7, pp. 550–556, 2012.

[114] B. Roy, M. P. Kennett, and S. Das Sarma, "Chiral symmetry breaking and the quantum hall effect in monolayer graphene," *Phys. Rev. B*, vol. 90, p. 201409, Nov 2014.

[115] M. I. Katsnelson, "Zitterbewegung, chirality, and minimal conductivity in graphene," *Eur. Phys. J. B*, vol. 51, no. 2, pp. 157–160, 2006.

[116] J. Tworzydło, B. Trauzettel, M. Titov, A. Rycerz, and C. W. Beenakker, "Sub-poissonian shot noise in graphene," *Physical Review Letters*, vol. 96, no. 24, p. 246802, 2006.

[117] L. Ponomarenko, A. Geim, A. Zhukov, R. Jalil, S. Morozov, K. Novoselov, I. Grigorieva, E. Hill, V. Cheianov, V. Fal'Ko, *et al.*, "Tunable metal-insulator transition in double-layer graphene heterostructures," *Nature Physics*, vol. 7, no. 12, pp. 958–961, 2011.

[118] F. Amet, J. R. Williams, K. Watanabe, T. Taniguchi, and D. Goldhaber-Gordon, "Insulating behavior at the neutrality point in single-layer graphene," *Phys. Rev. Lett.*, vol. 110, p. 216601, May 2013.

[119] M. Y. Kharitonov and K. B. Efetov, "Universal conductance fluctuations in graphene," *Phys. Rev. B*, vol. 78, p. 033404, Jul 2008.

[120] J. Berezovsky, M. Borunda, E. J. Heller, and R. M. Westervelt, "Imaging coherent transport in graphene (part i): mapping universal conductance fluctuations," *Nanotechnology*, vol. 21, no. 27, p. 274013, 2010.

[121] M. F. Borunda, J. Berezovsky, R. M. Westervelt, and E. J. Heller, "Imaging universal conductance fluctuations in graphene," *ACS Nano*, vol. 5, no. 5, pp. 3622–3627, 2011.

[122] Y.-F. Chen, M.-H. Bae, C. Chialvo, T. Dirks, A. Bezryadin, and N. Mason, "Magnetoresistance in single-layer graphene: weak localization and universal conductance fluctuation studies," *Journal of Physics: Condensed Matter*, vol. 22, no. 20, p. 205301, 2010.

[123] E. McCann, K. Kechedzhi, V. I. FalâĂŹko, H. Suzuura, T. Ando, and B. Altshuler, "Weak-localization magnetoresistance and valley symmetry in graphene," *Physical Review Letters*, vol. 97, no. 14, p. 146805, 2006.

[124] F. Tikhonenko, D. Horsell, R. Gorbachev, and A. Savchenko, "Weak localization in graphene flakes," *Physical review letters*, vol. 100, no. 5, p. 056802, 2008.

[125] A. Morpurgo and F. Guinea, "Intervalley scattering, long-range disorder, and effective time-reversal symmetry breaking in graphene," *Physical review letters*, vol. 97, no. 19, p. 196804, 2006.

[126] J. Moser, H. Tao, S. Roche, F. Alzina, C. S. Torres, and A. Bachtold, "Magnetotransport in disordered graphene exposed to ozone: From weak to strong localization," *Physical Review B*, vol. 81, no. 20, p. 205445, 2010.

[127] P. A. Lee and A. D. Stone, "Universal conductance fluctuations in metals," *Phys. Rev. Lett.*, vol. 55, pp. 1622–1625, Oct 1985.

[128] C. Beenakker and H. van Houten, "Quantum transport in semiconductor nanostructures," in *Semiconductor Heterostructures and Nanostructures* (H. Ehrenreich and D. Turnbull, eds.), vol. 44 of *Solid State Physics*, pp. 1 – 228, Academic Press, 1991.

[129] L. Ying, L. Huang, Y.-C. Lai, and C. Grebogi, "Conductance fluctuations in graphene systems: The relevance of classical dynamics," *Phys. Rev. B*, vol. 85, p. 245448, Jun 2012.

[130] E. Rossi, J. H. Bardarson, M. S. Fuhrer, and S. Das Sarma, "Universal conductance fluctuations in dirac materials in the presence of long-range disorder," *Phys. Rev. Lett.*, vol. 109, p. 096801, Aug 2012.

[131] P. M. Ostrovsky, I. V. Gornyi, and A. D. Mirlin, "Quantum criticality and minimal conductivity in graphene with long-range disorder," *Phys. Rev. Lett.*, vol. 98, p. 256801, Jun 2007.

[132] J. H. Bardarson, J. Tworzydło, P. W. Brouwer, and C. W. J. Beenakker, "One-parameter scaling at the dirac point in graphene," *Phys. Rev. Lett.*, vol. 99, p. 106801, Sep 2007.

[133] K. Nomura, M. Koshino, and S. Ryu, "Topological delocalization of two-dimensional massless dirac fermions," *Phys. Rev. Lett.*, vol. 99, p. 146806, Oct 2007.

[134] Y.-Y. Zhang, J. Hu, B. A. Bernevig, X. R. Wang, X. C. Xie, and W. M. Liu, "Localization and the kosterlitz-thouless transition in disordered graphene," *Phys. Rev. Lett.*, vol. 102, p. 106401, Mar 2009.

[135] I. L. Aleiner and K. B. Efetov, "Effect of disorder on transport in graphene," *Phys. Rev. Lett.*, vol. 97, p. 236801, Dec 2006.

[136] A. Altland, "Low-energy theory of disordered graphene," *Phys. Rev. Lett.*, vol. 97, p. 236802, Dec 2006.

[137] S.-J. Xiong and Y. Xiong, "Anderson localization of electron states in graphene in different types of disorder," *Phys. Rev. B*, vol. 76, p. 214204, Dec 2007.

[138] G. Schubert, J. Schleede, K. Byczuk, H. Fehske, and D. Vollhardt, "Distribution of the local density of states as a criterion for anderson localization: Numerically exact results for various lattices in two and three dimensions," *Phys. Rev. B*, vol. 81, p. 155106, Apr 2010.

[139] S. Das Sarma, E. H. Hwang, and Q. Li, "Disorder by order in graphene," *Phys. Rev. B*, vol. 85, p. 195451, May 2012.

[140] S. Das Sarma, S. Adam, E. H. Hwang, and E. Rossi, “Electronic transport in two-dimensional graphene,” *Rev. Mod. Phys.*, vol. 83, pp. 407–470, May 2011.